

University of Windsor

Scholarship at UWindor

Electronic Theses and Dissertations

Theses, Dissertations, and Major Papers

10-19-2015

Mechanical Properties and Microstructural Investigations of Welded MuCell® Glass Fibre Reinforced PA 6

Tianhao Guo
University of Windsor

Follow this and additional works at: <https://scholar.uwindsor.ca/etd>

Recommended Citation

Guo, Tianhao, "Mechanical Properties and Microstructural Investigations of Welded MuCell® Glass Fibre Reinforced PA 6" (2015). *Electronic Theses and Dissertations*. 5437.
<https://scholar.uwindsor.ca/etd/5437>

This online database contains the full-text of PhD dissertations and Masters' theses of University of Windsor students from 1954 forward. These documents are made available for personal study and research purposes only, in accordance with the Canadian Copyright Act and the Creative Commons license—CC BY-NC-ND (Attribution, Non-Commercial, No Derivative Works). Under this license, works must always be attributed to the copyright holder (original author), cannot be used for any commercial purposes, and may not be altered. Any other use would require the permission of the copyright holder. Students may inquire about withdrawing their dissertation and/or thesis from this database. For additional inquiries, please contact the repository administrator via email (scholarship@uwindsor.ca) or by telephone at 519-253-3000ext. 3208.

Mechanical Properties and Microstructural Investigations of Welded
MuCell® Glass Fibre Reinforced PA 6

By

Tianhao Guo

A Thesis
Submitted to the Faculty of Graduate Studies
through Engineering Materials
in Partial Fulfillment of the Requirements for
the Degree of Master of Applied Science
at the University of Windsor

Windsor, Ontario, Canada

2015

© 2015 Tianhao Guo

Mechanical Properties and Microstructural Investigations of Welded
MuCell® Glass Fibre Reinforced PA 6

BY

Tianhao Guo

APPROVED BY:

Vesselin Stoilov, Program Reader

Department of Mechanical, Automotive, and Materials Engineering

Tricia Carmichael, Outside Program Reader
Department of Chemistry and Biochemistry

Afsaneh Edrisy, Advisor

Department of Mechanical, Automotive, and Materials Engineering

Stephan Eichhorn, Advisor

Department of Chemistry and Biochemistry

Aug. 2015

AUTHOR'S DECLARATION OF ORIGINALITY

I am aware of the University of Windsor Senate Policy on Authorship and I certify that I have properly acknowledged the contributions of other researchers to my thesis, and have obtained permission from each of the co-authors to include the materials in my thesis.

I certify that, with the above qualification, this thesis, and the research to which it refers, is the product of my own work.

I certify that, to the best of my knowledge, my thesis does not infringe upon anyone's copyright nor violate any proprietary rights and that any ideas, techniques, quotations, or any other material from the work of other people included in my thesis, published or otherwise, are fully acknowledged in accordance with the standard referencing practices.

I declare that this is a true copy of my thesis, including any final revisions, as approved by my thesis committee and the Graduate Studies office, and that this thesis has not been submitted for a higher degree to any other University or Institution.

ABSTRACT

In this research, three different nylon-fibre glass composites with 30–35 wt. % glass fibre and one with 50 wt. % glass fibre were fabricated using the microcellular (MuCell®) injection moulding process with the weight reduction from 4 to 10% and were tested through burst and fatigue tests. Microstructural observation and thermal analyze were also employed to investigate the effect of the MuCell® process on mechanical properties. In the first phase of this study, the B3WG6-GPX material exhibited the highest weld strength as well as the longest fatigue life. As a result, it was selected for further investigation in the second phase. It is important to note that all samples failed at the weld region during the burst tests. Additionally, a microstructural analysis by scanning electron microscopy (SEM) and optical microscopy found uniform cells at the weld region of the MuCell®-processed parts, which suggested that cells can be generated in the molten polymer during vibration welding. In contrast to the fact that the weld depth (1.511 mm) for the selected sample during vibration welding was much lower than the none-cell region thickness. We concluded that the formation of the cells in the weld region is mainly responsible for the weaker welds.

DEDICATION

I dedicate this thesis to my loving parents for their support and unconditional love.

I dedicate this thesis work to my advisors Dr. A. Edrisy and Dr. S. Eichhorn for their support and guidance in my research career.

ACKNOWLEDGEMENTS

I would like to express my deepest gratitude to my advisors Dr. A. Edrisy and Dr. S. Eichhorn for their excellent guidance, patience and providing me with an great opportunity to start my research career, to let me experience the research of MuCell® plastic and vibration welding beyond the text books, patiently directed me and financially supported my research.

I also would to thank my committee members, Dr. Stoilov and Dr. Carmichael for their comments in improving my research and thesis. I would like to thank Jim vanderveen, Bobbye Baylis and Harold Colwell, who as our collaborator members were always willing to help and support this research. It would have been a long period without their kind support. Many thanks to K. Farokhzadeh and other colleagues in the group of Dr. Edrisy and Dr. Eichhorn for help in my research

TABLE OF CONTENT

AUTHOR’S DECLARATION OF ORIGINALITY	III
ABSTRACT	IV
DEDICATION	V
ACKNOWLEDGEMENTS	VI
LIST OF TABLES	XI
LIST OF FIGURES	XII
LIST OF ABBREVIATIONS, SYMBOLS	XIX
CHAPTER 1 INTRODUCTION	1
1.1 Overview	1
1.2 Motivation	1
1.3 Research objective.....	3
CHAPTER 2 REVIEW OF THE LITERATURE	5
2.1 Overview	5
2.2 MuCell® plastic	5
2.2.1 Advantages of MuCell® plastic.....	5
2.2.2 Manufacturing process of MuCell® plastics	9
2.3 Nucleation of MuCell®.....	16
2.3.1 Nucleation Theory	16
2.3.2 Homogeneous nucleation.....	17

2.3.3	Heterogeneous nucleation	19
2.4	Microstructures of MuCell® moulded part.....	22
2.4.1	Typical microstructure	22
2.4.2	Controlling methods of microstructures	23
2.5	Mechanical properties of MuCell® plastic	26
2.5.1	Effect of MuCell® process on mechanical properties	26
2.5.2	Relationship between microstructures and mechanical properties	27
2.5.3	Fatigue behaviour.....	30
2.6	Additives in MuCell® plastic and their effects on mechanical properties.....	35
2.6.1	Fibre additives.....	35
2.6.2	Nano-clay particle additives.....	42
2.7	Vibration Welding.....	45
2.7.1	Advantages and shortcomings	46
2.7.2	Typical applications for vibration welding	46
2.7.3	Typical structure of the weld region	47
2.7.4	Vibration welding for glass fibre reinforced composite	50
2.7.5	Vibration welding of glass fibre reinforced plastic moulded by MuCell® process	59
CHAPTER 3 MATERIALS AND EXPERIMENTAL METHODS		62
3.1	Overview	62

3.2	Materials.....	62
3.3	Vibration Welding.....	65
3.4	Metallography Sample Preparation for Cross-sectional View.....	67
3.5	Mechanical Properties test	67
3.5.1	Pressure Cycle Fatigue test	67
3.5.2	Burst Test	70
3.6	Microstructure Investigation	70
3.6.1	Optical microscopy analysis	70
3.6.2	Scanning Electron Microscopy Analysis	72
3.7	Crystallinity and Glass Fibre Content Analysis.....	74
3.7.1	Differential Scanning Calorimeter analysis	74
3.7.2	Thermogravmetric analysis.....	75
CHAPTER 4 EXPERIMENTAL RESULTS		76
4.1	Overview	76
4.2	Weld Strength Test Results	76
4.2.1	Pressure Cycle Fatigue Test Results	76
4.2.2	Burst Test Results	77
4.3	Optical Microscopy Investigation	79
4.3.1	Cell morphology: Cell Size and area occupied by cells.....	80
4.3.2	None-cell Region Thickness	83

4.4	Crystallinity and Glass Fibre Content	84
4.4.1	Thermogravmetric Analysis.....	84
4.4.2	Differential Scanning Calorimetry Results.....	86
4.5	Scanning Electron Microscopy Observation.....	90
4.5.1	Fracture Surface Investigation	90
4.5.2	Weld Region Investigation	95
CHAPTER 5 DISCUSSION.....		99
5.1	Effect of None-cell Region Thickness	100
5.2	effect of Glass fibre and Cell morphology	102
5.3	Effect of crystallinity.....	106
5.4	Effect of cells at weld region.....	107
CHAPTER 6 CONCLUSIONS AND RECOMMENDATIONS		111
6.1	Overview	111
6.1.1	Effect of the MuCell® process on weld strength.....	111
6.2	Recommendations for future research.....	112
REFERENCES		113
VITA AUCTORIS		120

LIST OF TABLES

Table 2.1 Comparison of injection-moulding process for various products with and without microcellular structure (Courtesy of Mar Lee Companies) [3]	6
Table 2.2 The improvement of dimension for under hood cover (unit: mm) [10]	7
Table 2.3 Critical properties for various solvents. [17]	11
Table 2.4 Summary of fiber length and property changes for polypropylene and nylon comparing traditional screw with LGF screw. [50]	40
Table 2.5 Component of the second order orientation tensor in terms of angles and elliptical axes dimensions: m, minor axis and M major axis [61]	53
Table 3.1 Descriptions of the tested materials	63
Table 3.2 Moulding conditions of PA6 grades	64
Table 3.3 Moulding conditions of PA66 grades	64
Table 5.1 Average none-cell region thickness and weld depth for solid, 4%, 7% and 10% WR samples	101

LIST OF FIGURES

Figure 1.1 This flow chart shows the methodology used for this study	4
Figure 2.1 Effect of SCF on viscosity of polymer [64].	7
Figure 2.2 The improvement of part length of the under hood cover [4].	9
Figure 2.3 Carbon dioxide pressure-temperature phase diagram [17].	12
Figure 2.4 Process chain for industrial foaming processes [18].	13
Figure 2.5 Process chain of foaming with autoclave preloading [18].	15
Figure 2.6 Autoclave process directly on moulding machine [18].	15
Figure 2.7 The excess free energy of clusters for homogeneous and heterogeneous nucleation [65].	21
Figure 2.8 Three areas of the general microstructure in MuCell® part [24].	23
Figure 2.9 SEM graphs with a (a) smaller and (b) larger magnification for moulded sample prepared at nozzle temperature of (1) 165, (2) 180, (3) 190°C [26].	24
Figure 2.10 SEM graphs with a (a) smaller and (b) larger magnification for moulded sample prepared at injection speed of (1) 35, (2) 45, (3) 55% (percentage of highest injection speed: 84cm ³ /s) [26].	25
Figure 2.11 SEM graphs with a (a) smaller and (b) larger magnification for moulded sample prepared for shot size of (1) 46, (2) 50, (3) 52 mm [26].	26
Figure 2.12 PBT mechanical properties with varying weight reductions [66].	27
Figure 2.13 Proportional contributions of the MuCell® morphological parameters to the mechanical properties under tensile loading [31].	28
Figure 2.14 Proportional contribution of the MuCell® morphological parameters to the mechanical properties under flexural loading [31].	29

Figure 2.15 Proportional contribution of the foam morphological parameters to the mechanical properties under impact loading [31].....	30
Figure 2.16 Failure mechanism in a tensile experiment. Left: Initiation of crack. Right: growth of crack [67].....	32
Figure 2.17 The assumed fatigue mechanism. Left: Initiation of damage. Right: development of damage, tensile debonding resulting from lateral contraction of the matrix [35].	33
Figure 2.18 Heated area of LGF PP with poor bonding between glass fibre and matrix. The arrow shows the position of the crack tip [39].	34
Figure 2.19 Schematic of the heat development in fatigue, when fibre/matrix debonding and fibre fracture was occurring [39].....	34
Figure 2.20 (O) Tensile strength and (+) flexural strength versus the volume fraction of the glass fibres [48].....	37
Figure 2.21 The tensile modulus; (O) apparent elastic modulus, (•) actual elastic modulus and (+) flexural modulus versus the volume fraction of glass fibres [48].	37
Figure 2.22 Specific flexural modulus of 20 wt. % glass fibre reinforced and unreinforced PC/ABS versus density reduction [49].....	38
Figure 2.23 SEM micrograph of the centre area of, a-c) microcellular foam unreinforced PC/ABS T85 with density reduction from 7% to 18%; d-f) microcellular foam glass fibre reinforced PC/ABS T884N with density reduction from 11% to 25% [49].....	39
Figure 2.24 Schematic comparison of standard microcellular screw with LGF screw [50].....	40

Figure 2.25 Glass Fibers – (a) Standard Screw (b) LGF Screw [50].....	41
Figure 2.26 Cross-section view of MuCell® sample moulded with (a). Neat PA 6 resin (b). 5% w.t. nano-clay reinforced PA 6 resin (c). 7.5% w.t. nano-clay reinforced PA 6 resin.....	44
Figure 2.27 Normalized toughness of sample moulded with different content of nano-clay [54].	44
Figure 2.28 Schematic of the weld process [68].....	45
Figure 2.29 Polarized transmitted light micrographs of microtomed sections of unreinforced polyamide-6 (a) HAZ-I (b) Bulk layer (c) deformed layer [68].....	48
Figure 2.30 SEM image of etched surface of HAZ from unreinforced polyamide-6 welded At 5 MPa. (1), (2), and (3) indicate HAZ, HAZ-I, and HAZ-II, respectively [68].....	49
Figure 2.31 Fracture surface of HAZ: (a) failed surface of the deformed layer; (b) the other failed surface of the recrystallized layer [68].	50
Figure 2.32 Comparison of ensile strength loss for unfilled and 30% glass fibre filled PA6 with different weight reductions [25].	51
Figure 2.33 Elliptical cross section of a cylindrical fibre: in this case, coordinates 1, 2, and 3, correspond to z, x, and y, respectively [61].	51
Figure 2.34 Treatment of images to obtain the fiber orientation tensor. (1) Micrograph (2) binary image (3) image analysis [61].....	52
Figure 2.35 Specimen preparation for fiber orientation measurement [61].....	54
Figure 2.36 A schematic of shear and squeeze flow during the vibration welding process. [61].....	55

Figure 2.37 Average amount of fibre with (a) a_{xx} orientation (b) a_{zz} orientation (c) a_{yy} orientation (d) a_{xy} orientation at HAZ welded at different welding parameters (1) HAZ welded at 0.6 MPa and 1 mm. (2) HAZ welded at 0.6 MPa and 1.78 mm. (3) HAZ welded at 5 MPa and 1 mm. (4) HAZ welded 5 MPa and 1.78 mm. (5) Bulk [61].	57
Figure 2.38 Tensile test results. (1) HAZ welded at 0.6 MPa and 1 mm. (2) HAZ welded at 0.6 MPa and 1.78 mm. (3) HAZ welded at 5 MPa and 1 mm. (4) HAZ welded at 5 MPa and 1.78 mm. (5) Bulk [61].	58
Figure 2.39 Cell structure close the weld area [63].	60
Figure 2.40 Burst test results for MuCell® samples moulded with PA6 (TechnylXCell S218 V35) and PA66 (Technyl A 218V35) [63].	60
Figure 3.1 Vibration welder	65
Figure 3.2 (a). cross-section of the 4mm and 6mm weld bead. (b). un-welded shells (c). welded shells. 4 mm and 6mm weld bead were welded together.	66
Figure 3.3 Selection of the samples	66
Figure 3.4 Cross-sectional view of (a) un-welded and (b) welded 4 mm and 6 mm beads samples prepared for microscopy investigation.	67
Figure 3.5 Pressure cycle fatigue testing machine and test set-up.	68
Figure 3.6 Pressure cycle during pressure cycle fatigue test	69
Figure 3.7 Thermal cycling during pressure cycle fatigue test	69
Figure 3.8 BASF burst test set-up	70
Figure 3.9 Sections to be observed using optical microscopy	71
Figure 3.10 Measurement of none-cell region. It refers to the distance from the outer layer to the region where the cells appear.	72

Figure 3.11 Scanning electron microscopy employed in research objective from Great Lakes Institute for Environmental Research at University of Windsor	73
Figure 3.12 Fractured sample underwent a burst test	73
Figure 3.13 DSC testing fixture	74
Figure 3.14 TGA testing fixture.....	75
Figure 4.1 Pressure cycle fatigue test results. Comparing with MuCell® samples, the solid samples exhibit significantly longer fatigue life. Additionally, B3WG6-GPX material exhibited the longest fatigue life among all the matrices.	77
Figure 4.2 Burst Test Results. The solid samples show the highest weld strength in the burst test, and the B3WG6-GPX samples are observed to have the best performance comparing with other matrices.	78
Figure 4.3 Typical structure of welded a. B3WG6-GPX 4% WR sample b. B3WG6-GPX 7% WR sample c. B3WG6-GPX 10% WR sample. The weld region, the flash and the cell region on the 4 mm and 6 mm parts can be observed on all the samples.....	80
Figure 4.4 (a) Average cell radius with standard deviation. The Largest and smallest cell radius can be observed on the 7% WR and 10% WR samples respectively. (b) Average cell area with standard deviation. Comparing with 4% WR and 10% WR samples, 7% WR samples tend to show larger cell size and area occupied by cells. Error bar is standard deviation.	81
Figure 4.5 Optical microscopy images for the cells regions a.4% WR sample b. 7% WR sample c. 10% WR sample. more uniformly sized and evenly distributed at the center of the cross-section as the weight reduction increases from 4% to 10%.	83

Figure 4.6 Average none-cell thickness with standard deviation. The thickness of none-cell layer was the highest at 4% WR and decreased with increasing weight reduction. Error bar is standard deviation. 84

Figure 4.7 The variation of TGA test results at weld region with varying weight reductions. The 7% WR sample exhibits the highest glass fibre content at weld region (35.19%), and the solid sample shows 2.3% lower content. Whereas, the glass fibre content for 4% WR sample is just 22.3% which is the lowest among all samples tested. 85

Figure 4.8 Results achieved by differential scanning calorimetry analyze for cell region. a. B3WG6-GPX 4% WR b. B3WG6-GPX 7% WR c. B3WG6-GPX 10% WR . 87

Figure 4.9 Results achieved by differential scanning calorimetry analyze for weld region. a. B3WG6-GPX solid b. B3WG6-GPX 4% WR c. B3WG6-GPX 7% WR d. B3WG6-GPX 10% WR 88

Figure 4.10 The variation of melting enthalpies with varying locations of samples. a. Cell region b. Weld region. The melting enthalpies after slow cooling at $1^{\circ}\text{C min}^{-1}$ tend to be larger than for the first heating of the “as moulded” samples. Besides, the obtained enthalpy was higher in the weld region than in the cell region..... 89

Figure 4.11 SEM morphologies of fracture surface for (a) solid sample with magnification of 400x. (b) solid sample with magnification of 1200x. (c) 4% WR sample with magnification of 400x. (d) 4% WR sample with magnification of 1200x. (e) 7% WR sample with magnification of 400x. (f) 7% WR sample with magnification of 1200x. (g) 10% WR sample with magnification of 400x. (h) 10% WR sample with magnification of 1200x. 94

Figure 4.12 Typical weld Region observed under SEM. A weld line created by re-orientation of glass fibre is observed.	96
Figure 4.13 Cells observed at weld region after cryogenic fracturing. (a) SEM image for 7% WR with the magnification of 400x (b) SEM image for 7% WR with the magnification of 1200x. Compact and deformed cells were found at the weld region. ...	98
Figure 5.1 Burst strength of the welded samples with standard deviation. Highest burst strength was observed on solid sample and the weld strength increased as the weight reduction of MuCell® sample increased from 4% to 7%.	100
Figure 5.2 (a) Fibre content at weld region for solid, 4%, 7% and 10% WR samples VS burst pressure. (b) Average cell radius VS glass fibre content at weld (c) Area occupied by cells VS glass fibre content at weld. Higher fibre content at the weld region would possibly result in higher weld strength among the MuCell® samples.	104
Figure 5.3 Schematic of the “push” effect of cell growth on glass fibre. The internal pressure provided by proper cell growth may result in the redistribution and orientation of glass fibre.	105
Figure 5.4 The degree of crystallinity for B3WG6-GPX with varying weight reduction	107
Figure 5.5 Schematic of the cell nucleating during vibration welding. Frictional heat generated will melt the polymer at the weld joint which creates a suitable condition for cells to nucleate.	109
Figure 5.6 Schematic of cell growth beside glass fibre	110
Figure 5.7 Cells on the welding surface would weaken the part joining and fibre-matrix bounding	110

LIST OF ABBREVIATIONS, SYMBOLS

ABS	acrylonitrile butadiene styrene
BSE	backscattered electron
DSC	differential scanning calorimetry
CBED	convergent beam electron diffraction
COF	coefficient of friction
EDS	energy dispersive spectroscopy
HAZ	heat affected zone
SCF	supercritical fluid
SE	secondary electron
SEM	scanning electron microscopy
TGA	thermogravimetric analysis
PA	polyamide
PC	polycarbonate
PBA	poly (butyl acrylate)
PBT	polybutylene terephth

CHAPTER 1 INTRODUCTION

1.1 OVERVIEW

This research study focuses on the microstructure and mechanical properties of MuCell® injection moulded and friction welded 30-35 wt. % glass fibre reinforced nylon 6 and Nylon 66 composite in order to determine the optimal MuCell® manufacturing parameters for maximum weld strength and the effect of this process on weld strength. This chapter presents background information related to this study along with the overall objective of the thesis.

1.2 MOTIVATION

In recent years, the polymer resin price has risen due to a petroleum shortage. This price increase has promoted manufacturing efforts to reduce plastic consumption and reduce part weight without sacrificing part quality. To that end, in the 1980s, Microcellular (MuCell®) plastics were developed at MIT to reduce material usage by creating a large number of small cells without significantly sacrificing the mechanical properties of the finished part.

The most common characteristic of a MuCell® moulded part is a special “sandwich-like” structure which contains three different regions: the first region is the none-cell region, which starts from the outer surface of the part and ends at the first cell in the sample. This layer is also referred as the solid layer. The existing none-cell layer eliminates the influence of MuCell® on the surface appearance and prevents the over loss

of mechanical properties such as tensile and impact strength. This layer also provides the necessary solid region for further vibration welding, preventing penetration of the weld region into the cell during welding. The second region is the irregular cell area at the edge of the sample, which begins at the end of the none-cell layer and ends where the cell diameter increases. The third region is referred to as the core cell area. It lies in the middle of the sample where the cells are observed to be the most regular and uniform. In this region, supercritical gas would have sufficient time and temperature to form cells with a finer structure, which mainly provide the weight reduction for the finished part.

The none-cell layer of the MuCell® part has a critical influence on the weld strength when vibration welding is employed after moulding. Its thickness is mainly controlled by the level of weight reduction. In vibration welding, it is difficult to keep the cells from the weld area, since the cell areas are not flat and are relatively wide. This inability of manufacturers to achieve sufficient strength in the joints of the MuCell® friction welded sample has prevented them from utilizing the MuCell® injection moulding procedure, thereby preventing them from enjoying its advantages.

The existing studies [1-6] of MuCell® plastics mainly focus on their tensile, flexural, and impact properties. A microstructural evaluation of MuCell® parts after welding and the effect of the MuCell® process on weld strength have not been systemically studied; therefore, we determined that these topics would be the focus of our research.

1.3 RESEARCH OBJECTIVE

The aims of this study are to identify the optimized raw material that would provide the highest weld strength and to investigate the effect of MuCell® on weld strength for selected materials.

A research flow chart is illustrated in Figure 1.1. As with any research study, the first step in this study was a background (literature) review. This review examined MuCell® plastics; specifically glass fibre reinforced MuCell® plastics, as well as their manufacturing processes, microstructures, and mechanical properties. The studies of vibration welding for glass fibre reinforced plastic and MuCell® plastics were also included.

In this study, the microstructures of the weld, none-cell, and cell regions were examined for each sample using optical and scanning electron microscopes. The mechanical tests employed to determine the strength of the MuCell® samples at the weld region were a burst test and a pressure cycle fatigue test. After each test, the fracture surfaces were examined using scanning electron microscopy in order to analyze the failure mechanism. In addition, analyses of the degree of crystallinity and fibre content at the weld region were also carried out on welded parts.

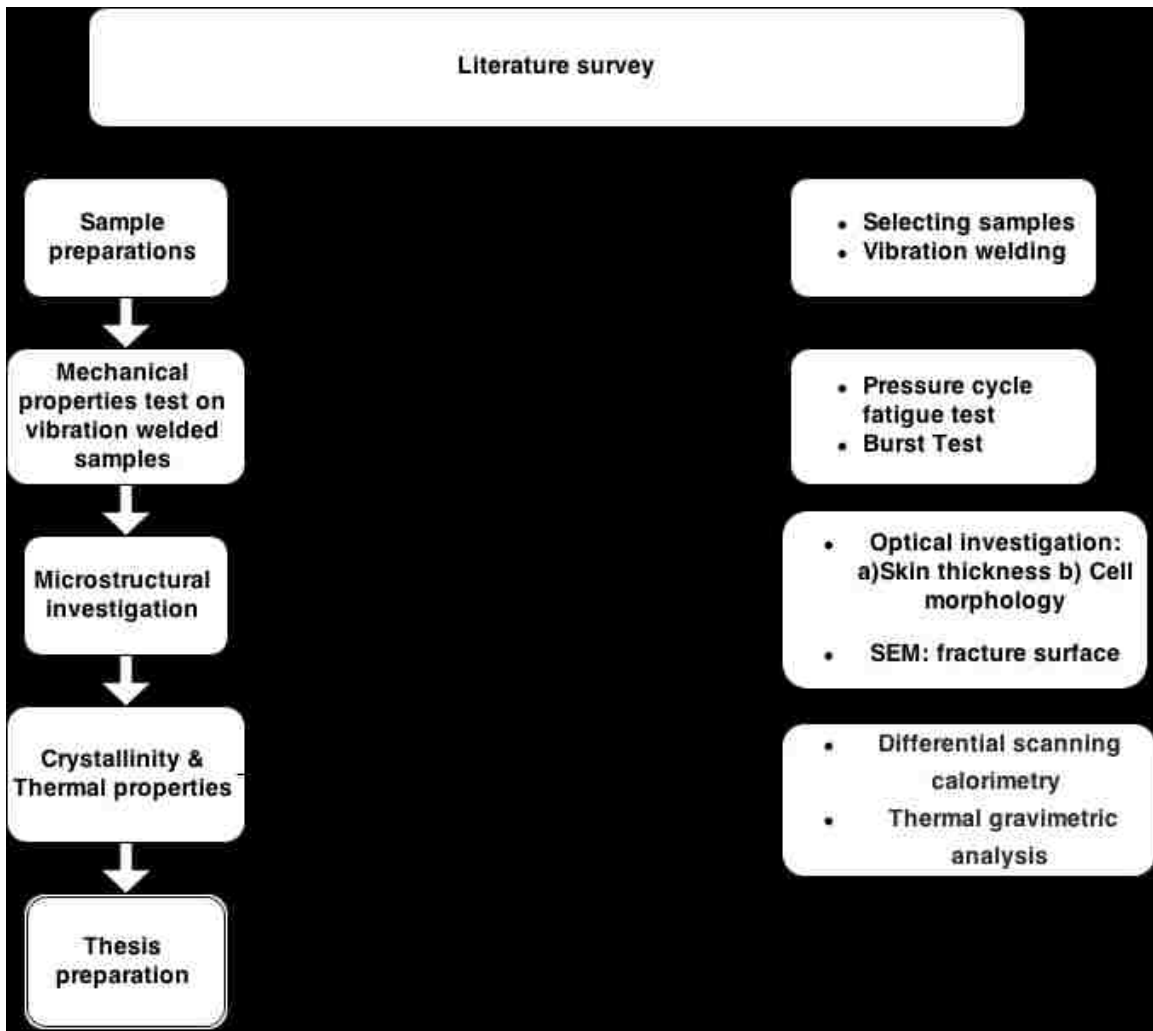


Figure 1.1 This flow chart shows the methodology used for this study

CHAPTER 2 REVIEW OF THE LITERATURE

2.1 OVERVIEW

This chapter introduces the advantages, manufacturing process, microstructures and mechanical properties of MuCell® plastics. Vibration welding on traditional and MuCell® plastics is explained. The relationship between the microstructure and mechanical properties of MuCell® plastics is also discussed.

2.2 MUCELL® PLASTIC

Facing rising raw material costs and the need to develop sustainable applications, the plastics industry has turned to the MuCell® process as a unique solution because it reduces the material consumption in moulded parts and reduces the energy usage during both the production process and the product's service life.

The process of microcellular injection moulding includes mixing the desired polymer with a gas through the use of a screw system and short shooting the molten material into the die. The pressure generated by the gas in the polymer mixture coming out of solution provides a uniform packing pressure [7-8].

2.2.1 ADVANTAGES OF MUCELL® PLASTIC

The microcellular process can be used on any thermoplastic, thermoset plastic or even some elastomers, which has closed cells of very small diameter included in the polymer. The main drives for the creation of MuCell® plastic were the advantages provided through the weight savings and savings in the raw material. By decreasing the diameter of the cells generated by the MuCell® process to a size smaller than the voids

already existing in the material, weight reduction can be achieved without compromising the strength of the material [9].

2.2.1.1 OPTIMIZATION OF THE MANUFACTURE PROCESS

The other benefits of the MuCell® moulding process are a substantial decrease in the injection pressure due to the presence of dissolved gas, which lowers the viscosity (Figure 2.1), and also that the cycle time can be reduced due to the elimination of the “hold and pack” time and also due to about 25% reduction in cooling time. A detailed comparison of the injection moulding process with and without the dissolved gas is presented in Table 2.1.

Table 2.1 Comparison of injection-moulding process for various products with and without microcellular structure (Courtesy of Mar Lee Companies) [3]

		Conventional	MuCell	Percentage %
Air Bag Canister (33% glass filled Nylon)	Part Weight	365 g	252 g	30.9
	Cycle Time	45 sec	35 sec	22.2
	Clamp Tonnage	150 tons	15 tons	90
Connector (polycarbonate)	Part Weight	48.8 g	42.9 g	10.6
	Cycle Time	17.5 sec	15.9 sec	9.1
	Clamp Tonnage	140 tons	20 tons	85.7
Battery Cover (polypropylene)	Part Weight	201 g	159 g	20.8
	Cycle Time	60 sec	37 sec	38.3
	Clamp Tonnage	200 tons	15 tons	92.5

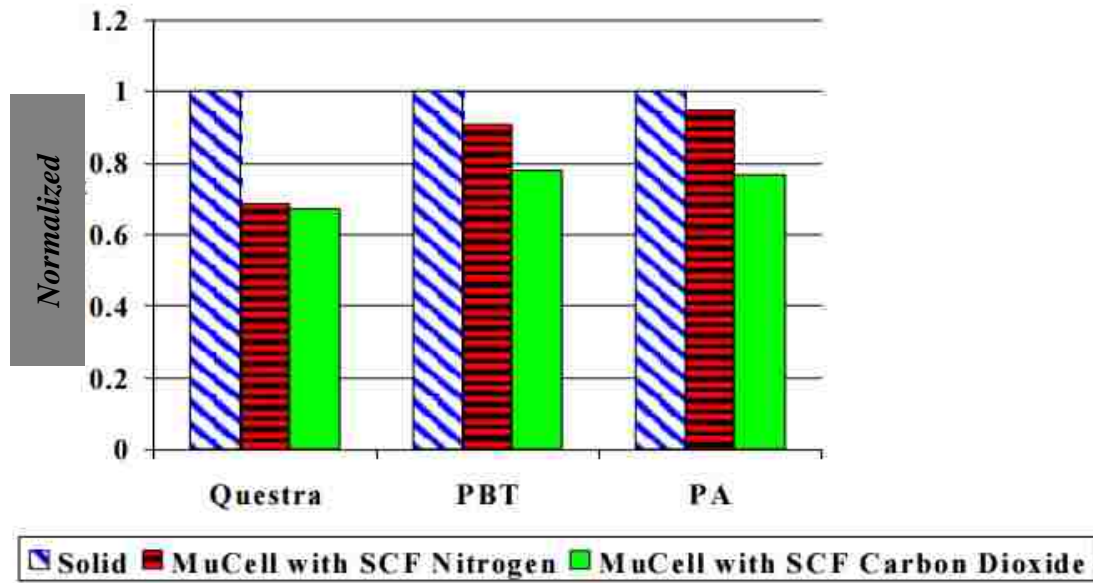


Figure 2.1 Effect of SCF on viscosity of polymer [64].

2.2.1.2 IMPROVEMENT OF DIMENSIONAL STABILITY

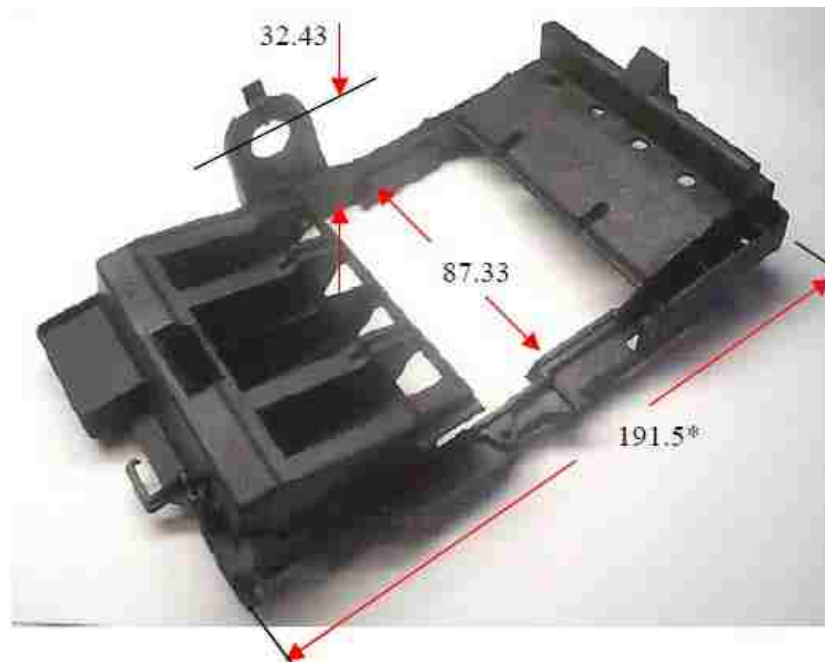
Moreover, a significant increase in dimensional stability was found when using the microcellular process. Dimensional stability in this case refers to the retention of the feature dimensions and lack of shrinkage in the moulded part. The problem of shrinkage and shift in dimension is especially critical in large moulded solid polymer parts such as engine intake manifolds, which would also achieve benefit from weight reduction.

It has been shown through studies conducted using Polyamide (PA) 66 (glass fibre (G. F.) 33% wt.) Zytel 70G33L that the factors that most influence dimensional stability in microcellular moulding were the injection speed, the mould temperature, the cooling time, and the supercritical fluid level. When these factors are correctly optimized for the particular application (as shown in Figure 2.2, the moulding of a under hood cover was studied in this case), a product with superior dimensional stability can be produced

when compared to its solid counterpart. In this particular study an under hood cover was moulded using both traditional moulding and the MuCell® process. As is shown in Table 2, the MuCell® samples showed more dimensional stability than their solid counterparts [10].

Table 2.2 The improvement of dimension for under hood cover (unit: mm) [10]

Key Dimension	Std Dev Solid	Std Dev MuCell
Height (32.43mm)	0.01mm	0.0045mm
Width (87.33mm)	0.015mm	0.0025mm
Length (191.50mm)	0.016mm	0.0035mm



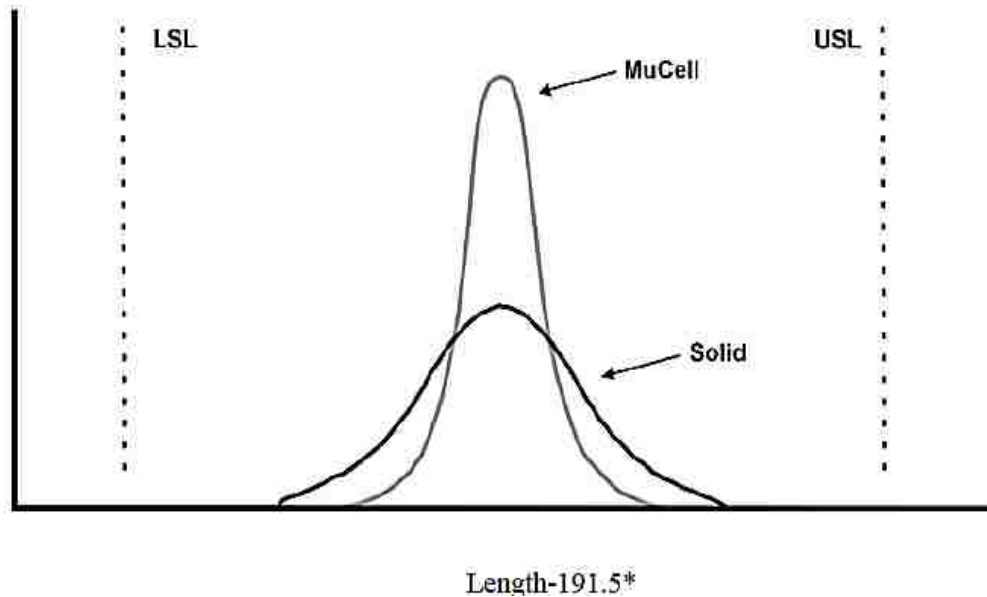


Figure 2.2 The improvement of part length of the under hood cover [4].

2.2.2 MANUFACTURING PROCESS OF MUCCELL® PLASTICS

In general, microcellular plastics are manufactured through the dissolving of a large amount of gas, generally either CO₂ or N₂, inside the plastic melt under high pressure and temperature.

Because the pressure is suddenly dropped as the molten material enters the mould, phase separation between the polymer and the dissolved gas starts, creating the distinctive closed cells. The driving factors for the creation of the cells inside the polymer are the applied temperature and pressure, the amount of dissolved gas present in the mixture and the presence of any additional additives in the polymer itself. The introduction of this thermodynamic instability reduces the solubility of the gas and results in the nucleation of the cells [9].

The reason for the apparent homogeneity of the produced cells comes as a result of the simultaneous nucleation of the second phase gas inside the material. The speed of nucleation is due to the large driving parameters such as the immediate drop in pressure, the percentage of dissolved gas and the temperature of the polymer during moulding.

Several physical conditions must be met for the MuCell® process to proceed correctly:

The first is that the plastic should be super saturated with sufficient gas (this usually being either N₂ or CO₂ in the case of a physical foaming agent) in order to nucleate a large number of cells simultaneously and to achieve a uniform material without interconnecting cells.

Secondly, the flow of the polymer during the moulding process must be sufficiently controlled by setting the temperature of the polymer.

Finally, the gas chosen for the MuCell® process must have suitable solubility and diffusivity in the selected polymer in order to have a sufficient amount of gas to be dissolved in the polymer solution, providing enough driving force for homogeneous nucleation inside the mould [10-13].

2.2.2.1 SUPERCRITICAL FLUID

Supercritical fluid (SCF) is the gas at a certain temperature and pressure higher than its critical point, where either the liquid or gas phases no longer exist. More specifically, SCF can effuse through solids like gas, or dissolve materials like liquid. Furthermore, near the critical point, tiny changes in pressure or temperature lead to enormous changes in density and allow many of the properties of SCF to be “fine-tuned.”

CO₂ and N₂ are the most commonly chosen SCF for MuCell® injection moulding [14-16].

In Figure 2.3, the boiling separates the gas and liquid regions and ends at the critical point, where the liquid and gas phases disappear to generate a single phase.

Generally, supercritical fluids generate with the properties between gas and liquid. The critical properties for some components which are commonly used as SCF are shown in Table 2.3.

Table 2.3 Critical properties for various solvents [17].

Solvent	Molecular weight g/mol	Critical temperature K	Critical pressure MPa	Critical density g/cm ³
Carbon dioxide (CO ₂)	44.01	304.1	7.38	0.469
Water (H ₂ O) (acc. IAPWS)	18.015	647.096	22.064	0.322
Methane (CH ₄)	16.04	190.4	4.60	0.162
Ethane (C ₂ H ₆)	30.07	305.3	4.87	0.203
Propane (C ₃ H ₈)	44.09	369.8	4.25	0.217
Ethylene (C ₂ H ₄)	28.05	282.4	5.04	0.215
Propylene (C ₃ H ₆)	42.08	364.9	4.60	0.232
Methanol (CH ₃ OH)	32.04	512.6	8.09	0.272

Ethanol (C ₂ H ₅ OH)	46.07	513.9	6.14	0.276
Acetone (C ₃ H ₆ O)	58.08	508.1	4.70	0.278
Nitrous oxide (N ₂ O)	44.013	306.57	7.35	0.452

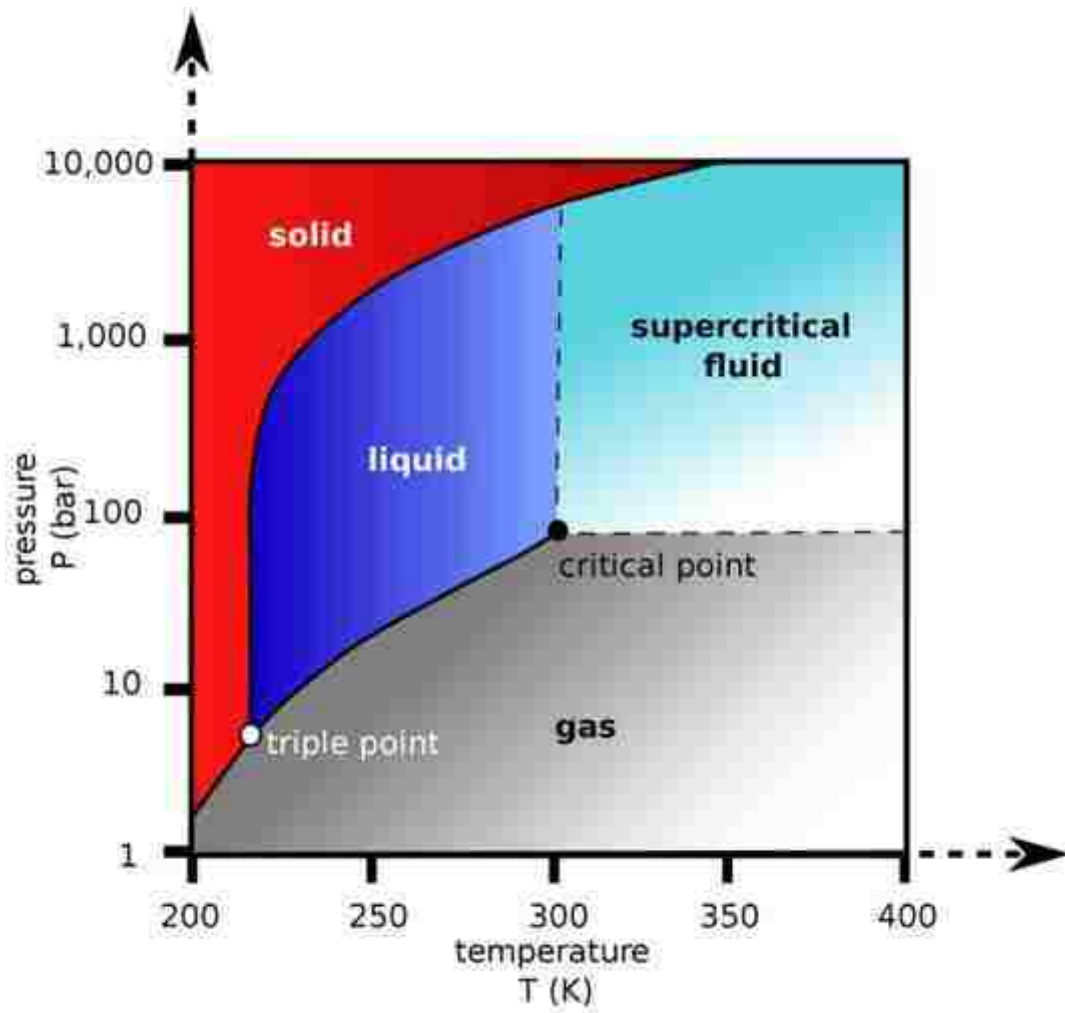


Figure 2.3 Carbon dioxide pressure-temperature phase diagram [17].

2.2.2.2 SUPERCRITICAL FLUID DIRECT INJECTION

In most industrially used processes of MuCell® injection moulding, as illustrated in Figure 2.4, the blowing agent (N₂ or CO₂ gas) is injected directly at high pressure into the polymer melt as supercritical fluid (SCF). The two-phase mixture is then blended to insure dilution of the gas into a homogeneous mixture. The bubbles of the blowing agent are divided into increasingly smaller sections. The gas dissipation in the polymer matrix of this method is very sensitive to the pressure of incoming gas and the time of the mixing of the two-phase solution. Running the process with wrong pressures or times leads to incomplete solving of the blowing agent. The remaining SCF in the polymer melt can join to form a single, large gas bubble. Then the process becomes very difficult to control and the part quality from shot to shot varies [18-19].

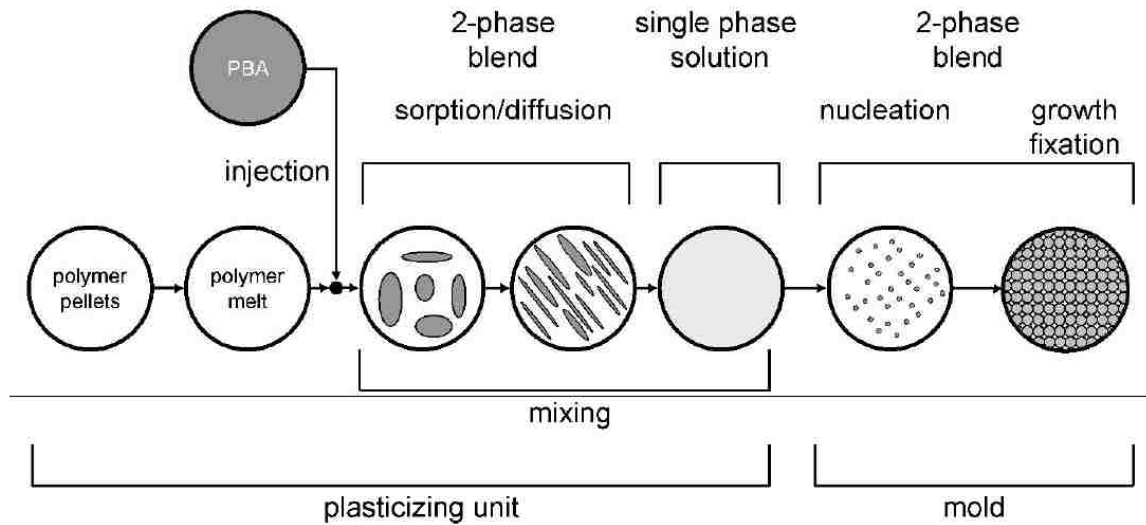


Figure 2.4 Process chain for industrial foaming processes [18].

2.2.2.3 AUTOCLAVE PRELOADING

During the injection moulding process, a completely single-phase solution must always be achieved in order to avoid any irregularities in the finished products such as excessively large or interconnected cells. The autoclave process is a method for mixing the physical foaming agent into the polymer prior to the injection moulding process (Figure 2.5). This is achieved by storing the polymer pellets under the pressurized atmosphere of the blowing agent over long periods of time (12-18 hours), allowing the blowing agent to diffuse until the polymer becomes saturated. The diffusivity of both N_2 and CO_2 are approximately the same and are proportional to the square of the penetration length and temperature. As the gases are then melted, a single-phase solution is achieved since no gas is directly injected into the polymer melt. The amount of gas introduced into the polymer is also more rigidly set and cannot vary during the injection process. The saturation concentration of the gas in the autoclave process depends strongly on the exposing pressure and temperature. This quantity is measured in the weight percentage of the gas absorbed by the material. The advantage of autoclave processing is the guarantee of a uniform single-phase solution during the industrial moulding process. However, the autoclave process has not been widely used in injection moulding production, since its batch process requires long preloading and desorption times. Preloading the polymer for production with several moulding machines would require many autoclaves, and desorption has to be continuously monitored to achieve a stable product quality. It should be noted that as soon as the polymer material is removed from the autoclave, the saturation percentage of gas begins to drop. Thus, each batch of polymer must be

injection-moulded within a certain amount of time to avoid the loss of the foaming agent [18-19].

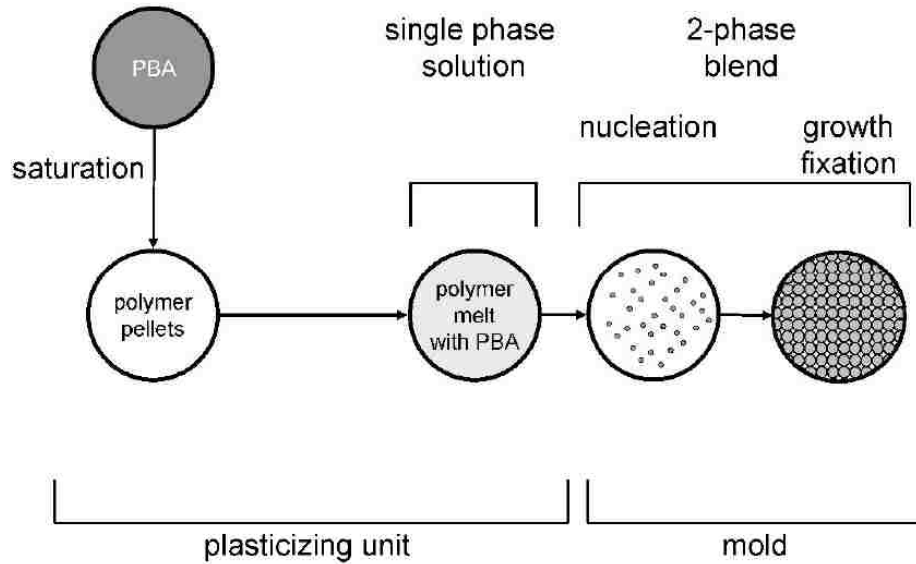


Figure 2.5 Process chain of foaming with autoclave preloading [18].

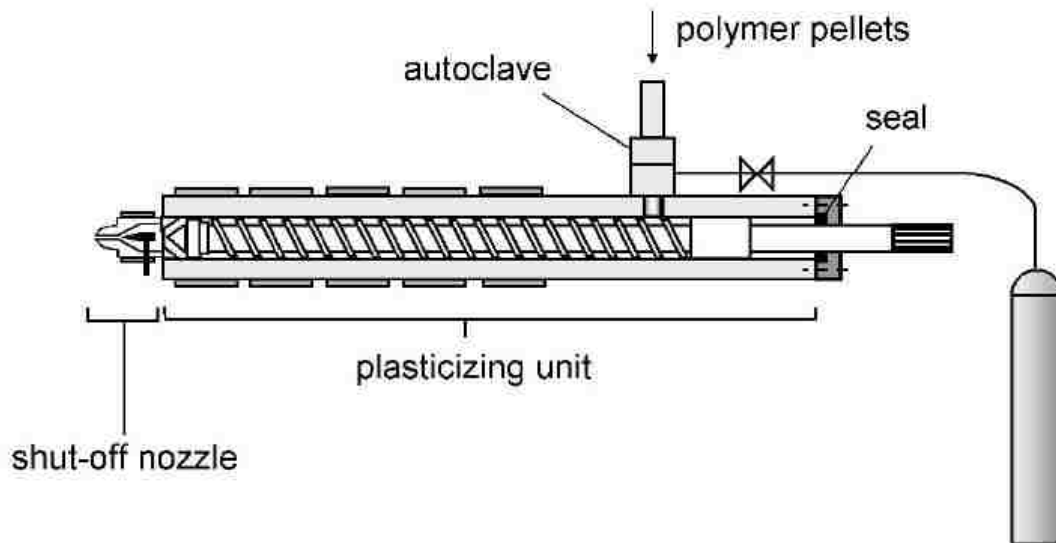


Figure 2.6 Autoclave process directly on moulding machine [18].

2.2.2.4 CHEMICAL FOAMING AGENTS

When using a chemical foaming process, the matrixes are physically mixed with the solid chemical agent, which acts as the foaming agent when activated. This additive foaming agent is completely mixed with the polymer solution and decomposes during the moulding process. The decomposing process occurs through a chemical reaction triggered either by increase in heat or drop in pressure of the polymer solution, releasing gas and creating the microcellular structure inside the products. The gases released by this type of reaction are mainly N₂ or CO₂. The advantages of chemical foaming agents over physical foaming agents include a more precise control of gas quantity dissolved in the solution, the ability to mould the microcellular part without modification of the moulding equipment, and the short processing time needed to introduce the foaming agent into the polymer solution. However, additional residual products also appear within the reaction, which can amount to 70 w.t. % of the additive material. These products have a negative effect on the quality of the polymer matrix, including the reduction of its mechanical properties, degradation of the polymer matrix, and unwanted coloration of the finished part [18].

2.3 NUCLEATION OF MUCCELL®

2.3.1 NUCLEATION THEORY

The nucleation theory was developed in the early 20th century. A classic nucleation theory was firstly proposed by Colton [20], which can be classified into three types: homogeneous nucleation, heterogeneous nucleation, and cavity nucleation.

Homogenous nucleation occurs in a single-phase solution system that has no impurities. During the pressure unloading process, every SCF molecule is a nucleation point. Thus, theoretically, the largest nucleation density and the smallest cell size will be generated by homogeneous nucleation. However, for the purity of the system, more energy is required to cross the “energy barrier” to create the nucleus. Therefore, there should be more super saturation in the MuCell® mixer system.

The impurity in the system is considered by the heterogeneous nucleation. The higher interfacial energy at the impurity solid surface would result in a bigger driving force at the impurity than other region. Thus, less free energy needs to be overcome for the nucleus generation. In other words, the heterogeneous nucleation is easier to generate nuclei more easily compared to homogeneous nucleation.

Cavity nucleation involves many nuclei being generated at the locations of cavities. The gas will be absorbed in the cavity by the nucleating agent or any other micro-impurities. The polymer mixer is not able to enter the split wedges at the rough surface. However, the gas will be trapped in these split wedges. Most of the gas will enter those cavities to form the nuclei. In the meantime, these cavities can save nucleation energy, and a stable nucleus can be easily generated.

2.3.2 HOMOGENEOUS NUCLEATION

The main concern of the classical homogenous nucleation theory is a thermodynamic description of the initial nucleation. When the equilibrium is broken and the free energy of the polymer mixer is more than the energy barrier, phase separation will occur, and nuclei will generate. When the nuclei are larger than the critical size, the

nuclei become stable and continue to form cells. The nucleation rate of the homogeneous nucleation can be described as follows:

$$N_{homo} = C_0 f_0 \exp\left(\frac{\Delta G}{KT}\right) \quad (1)$$

where the N_{homo} is the number of the nuclei generated per cm^3 per second, C_0 is the concentration of the gas, f_0 is the frequency factor of the gas molecules, K is the Boltzmann's constant, and T is the absolute temperature. ΔG is the energy barrier for the homogeneous nucleation. ΔG can be generated by the following equation:

$$\Delta G_{homo} = \frac{16\pi r^3}{3\Delta P^2} \quad (2)$$

where ΔP is magnitude of the quench pressure, and r is the surface energy of the cell interface.

The frequency factor of the gas molecules (f_0) can be explained as follows:

$$f_0 = Z\beta \quad (3)$$

Z , the Zeldovich factor, accounts for the fact that a larger number of nuclei never grow, but rather dissolve. The rate at which the molecules are added to the critical nucleus, β , can be calculated as the surface area of the critical nucleus times the rate of impingement of gas molecules per unit area.

$$\beta = (4\pi r_c^3)R_{impingement} \quad (4)$$

Then the frequency factor can be express as:

$$f_0 = Z(4\pi r_c^3)R_{impingement} \quad (5)$$

The equation above shows that the frequency factor of the gas molecules joining a nucleus to make it stable varies with the surface area of the nucleus. Generally, Z can be regarded as fitted parameter.

Knowing the surface energy of the system is a function of pressure and temperature, the critical size of the nuclei can be calculated at any condition by:

$$r_c = \frac{2r}{\Delta P} \quad (6)$$

From all the equations discussed above, a nucleation model for polymer-SCF solution can be developed.

In order to calculate the number of the nuclei produced in the system at given conditions, the rate of nucleation needs to be integrated over the time period of nucleation. Generally the gas pressure falls along with the time duration. Therefore, the starting saturation pressure and the pressure at which the polymer vitrifies define the time scale over which the rate of nucleation should be integrated. [20] So, the number of nuclei can be illustrated as follows:

$$N_{total} = \int_{P_g}^{P_{vit}} N_{homo} \frac{dP}{dP/dt} \quad (7)$$

2.3.3 HETEROGENEOUS NUCLEATION

Heterogeneous nucleation happens at the interface of two phases, which is also illustrated by classical nucleation theory. For the nucleation of the cell at the interface of a polymer and a second phase particle/fibre, the interfacial surface tensions' balance gives:

$$r_{ap} = r_{cp} + r_{api} \cos \theta \quad (8)$$

where r_{ap} , r_{bp} , and r_{api} are the interfacial tensions of the particle/fibre-polymer, cell-polymer, and particle/fibre-polymer interface, respectively, and the θ is the wetting angle of the interface. The formation of such an embryo will be associated with an excess free energy:

$$\Delta G_{homo} = -V_c \Delta P + A_{cp} r_{cp} + A_{ac} r_{ac} - A_{ap} r_{ap} \quad (9)$$

The V_c is the volume of the cells and the A_{cp} , A_{ac} , and A_{ap} are the areas of the cell-polymer, additive particle/fibre-cell, and additive particle/fibre-polymer interfaces, respectively.

With algebraic manipulation, the equation above can be expressed as follows:

$$\Delta G_{het} = \left\{ -\frac{4}{3} \pi r^3 \Delta P + 4 \pi r^2 r_{cp} \right\} S(\theta) \quad (10)$$

where $S(\theta)$ depends only on the wetting angle, θ .

Thus, the radius of a critical nucleus, r_c^* and the Gibbs free energy needed to nucleate a critical nucleus, ΔG_{het} , can be expressed as follows:

$$r_c^* = \frac{2r_{cp}}{\Delta P} \quad (11)$$

and

$$\Delta G_{het} = \frac{16\pi r_{cp}^3}{3\Delta P^2} S(\theta) \quad (12)$$

Comparing the free energies of homogenous and heterogeneous nucleation, a new equation can be yielded:

$$\Delta G_{het} = \Delta G_{homo} S(\theta) \quad (13)$$

For a typical wetting angle of 20° , $S(\theta)$ is on the order of 10^{-3} . Thus, the energy barrier for heterogeneous nucleation can be significantly reduced by the presence of an interface. Figure 2.7 expresses the schematic of both ΔG_{het} and ΔG_{homo} .

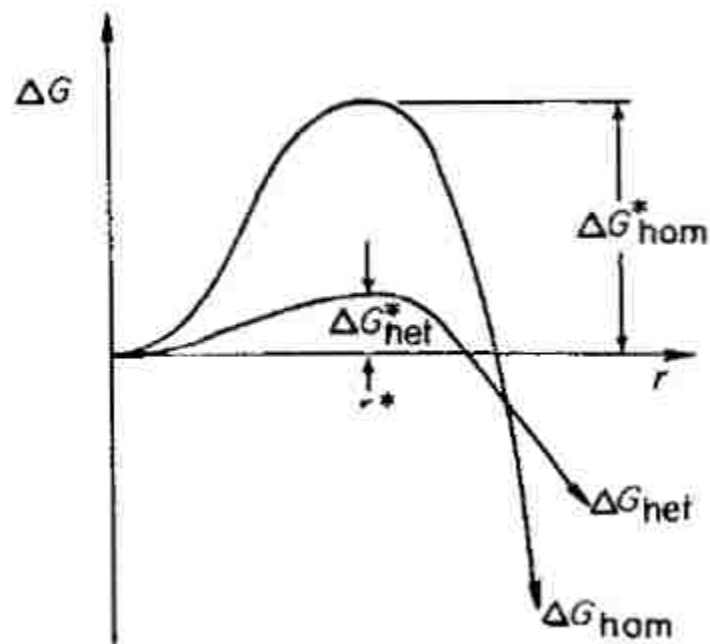


Figure 2.7 The excess free energy of clusters for homogeneous and heterogeneous nucleation [65].

The rate of the heterogeneous nucleation can be explained as:

$$N_{het} = C_1 f_1 \exp\left(\frac{\Delta G_{het}}{KT}\right) \quad (14)$$

where f_1 is a frequency factor similar to f_0 , and stands for the frequency that gas molecules impinge upon the embryo nucleus. It is a complex function of the vibrational frequency of the atoms, the activation energy for diffusion in the polymer, and the surface area of the critical nucleus. C_1 is the concentration of heterogeneous nucleation sites [21-23].

2.4 MICROSTRUCTURES OF MUCELL® MOULDED PART

2.4.1 TYPICAL MICROSTRUCTURE

It is known that a great variety of possible microstructural modifications can be found in MuCell® parts, while a general sample structure is often observed in most MuCell® parts. Usually, the MuCell® samples can be divided into three different areas (Figure 2.8). The first area is the solid layer. This layer ends at the first cell in the sample, at both the upper side and the bottom of the moulded sample. This section of the sample is usually referred to as the none-cell layer or the solid layer of the sample. At this layer, the temperature difference and rapid cooling as the molten polymer material comes into contact with the moulding die causes solidification of the polymer without allowing for the formation of cells.

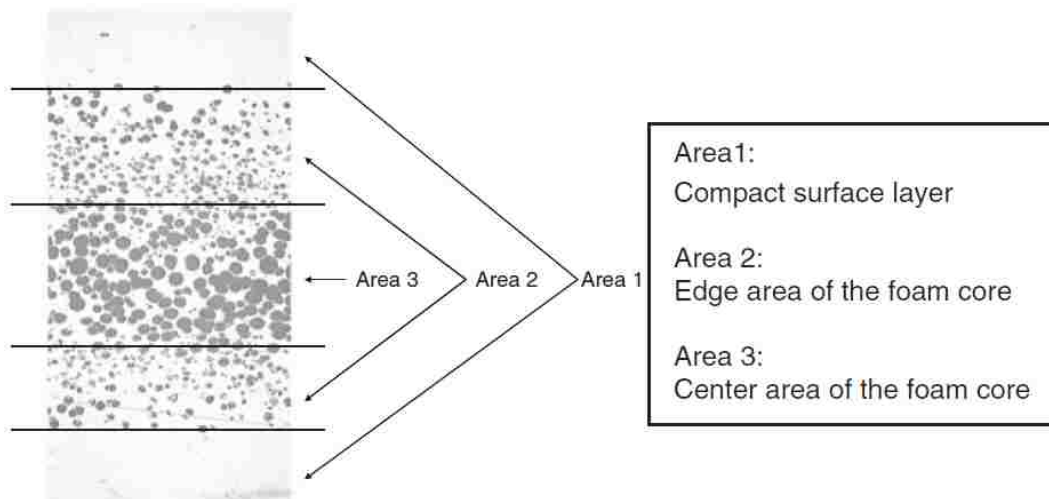


Figure 2.8 Three areas of the general microstructure in MuCell® part [24].

The second layer is the cell area at the edge of the sample, which begins at the end of the surface layer and ends where the cell diameter increases. The third area lies in the middle of the sample, where the cells are observed to be the most regular and compact [24-25].

2.4.2 CONTROLLING METHODS OF MICROSTRUCTURES

Several investigations done by Huang and Wang on polystyrene using the MuCell® process show that the processing parameters, including nozzle temperature, injection speed, and shot size, have some effect on the cell structure and non-cell thickness [26].

The effect of nozzle temperature on the cellular structure is illustrated in Figure 2.9. A finer and more uniform cell structure is formed, and a clearer boundary between the core and non-cell regions can be observed at lower nozzle temperatures (165~180°C), as illustrated in Figure 2.9 (a) and (b); whereas non-uniform cellular structure with large diameter cells, as shown in Figure 2.9 (c), is observed when higher

nozzle temperatures (such as 190°C) are employed. This may be due to the fact that at lower nozzle temperatures, the PS melt has a higher strength, which helps melt to enwrap gas [26].

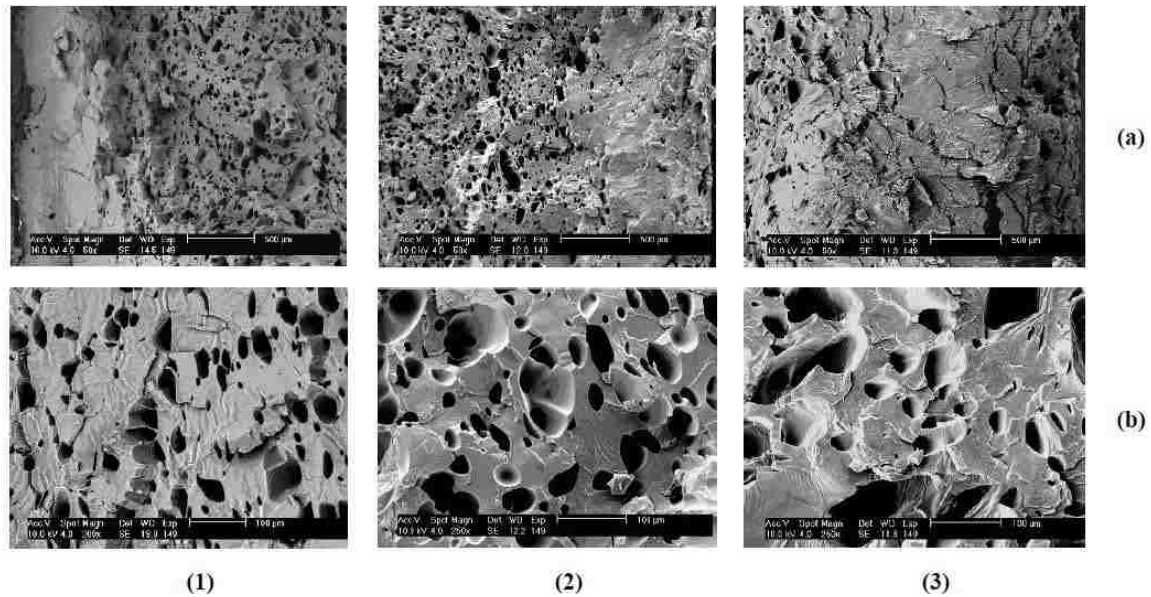


Figure 2.9 SEM graphs with a (a) smaller and (b) larger magnification for moulded sample prepared at nozzle temperature of (1) 165, (2) 180, (3) 190°C [26].

The effect of the injection speed on the cellular structure is illustrated in Figure 2.10. It can be concluded that the increased injection speed results in the decrease of the none-cell thickness, which is about 0.9, 0.7, and 0.6 mm at injection speeds of 35, 45, and 55%, respectively. This is attributed to the fact that an increase in injection speed leads to a corresponding decrease of melt filling time and the convective heat transfer between the mould cavity and melt during melt injection. This gives a more uniform melt temperature distribution near the cavity. Furthermore, it can be observed from Figure 2.10 that cell diameter decreases, cell density increases, and cellular structure uniformity improves with an increase of injection speed. This is due to the fact that a higher injection speed

produces a higher pressure drop and pressure drop rate, which increases the nucleation rate.

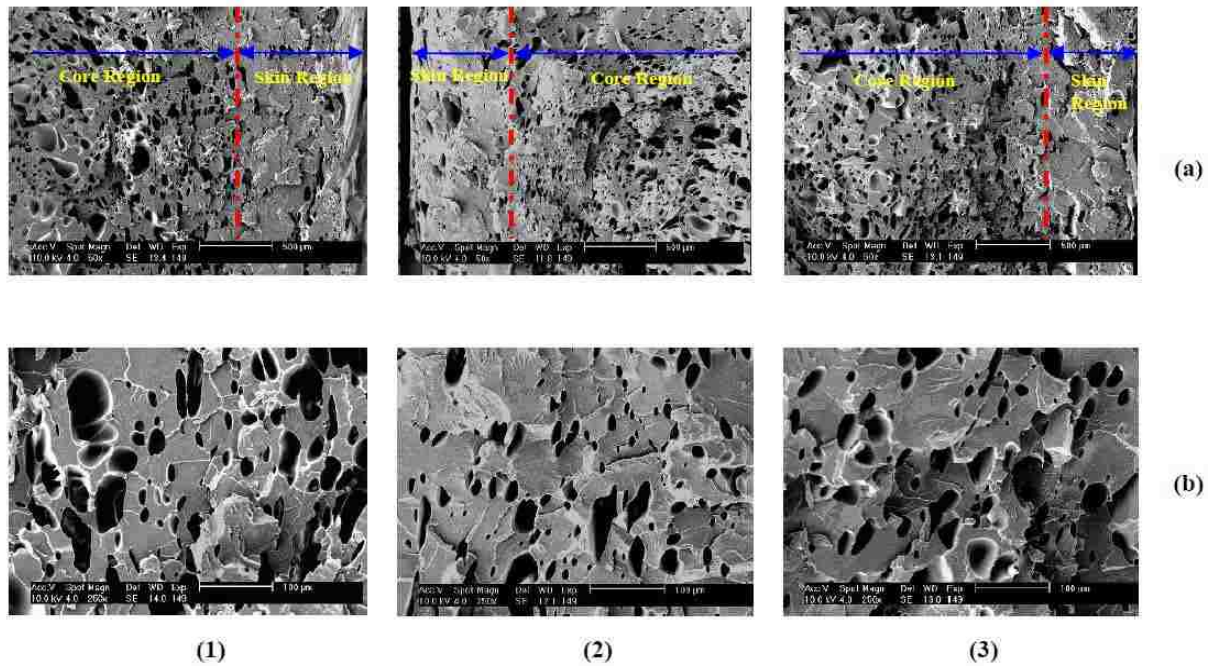


Figure 2.10 SEM graphs with a (a) smaller and (b) larger magnification for moulded sample prepared at injection speed of (1) 35, (2) 45, (3) 55% (percentage of highest injection speed: $84\text{cm}^3/\text{s}$) [26].

It can be concluded from Figure 2.11 that cell diameter decreases, cell density increases, and cellular structure uniformity improves along with shot size increase. This may be due to the fact that at appropriately larger shot sizes, the smaller space between the mould cavity and melt retards the cells' growth. However, the influence of shot size on the thickness of the none-cell region is not observed to be significant. The thickness of the none-cell region is about 0.8 mm for the test samples prepared at these three shot sizes [26].

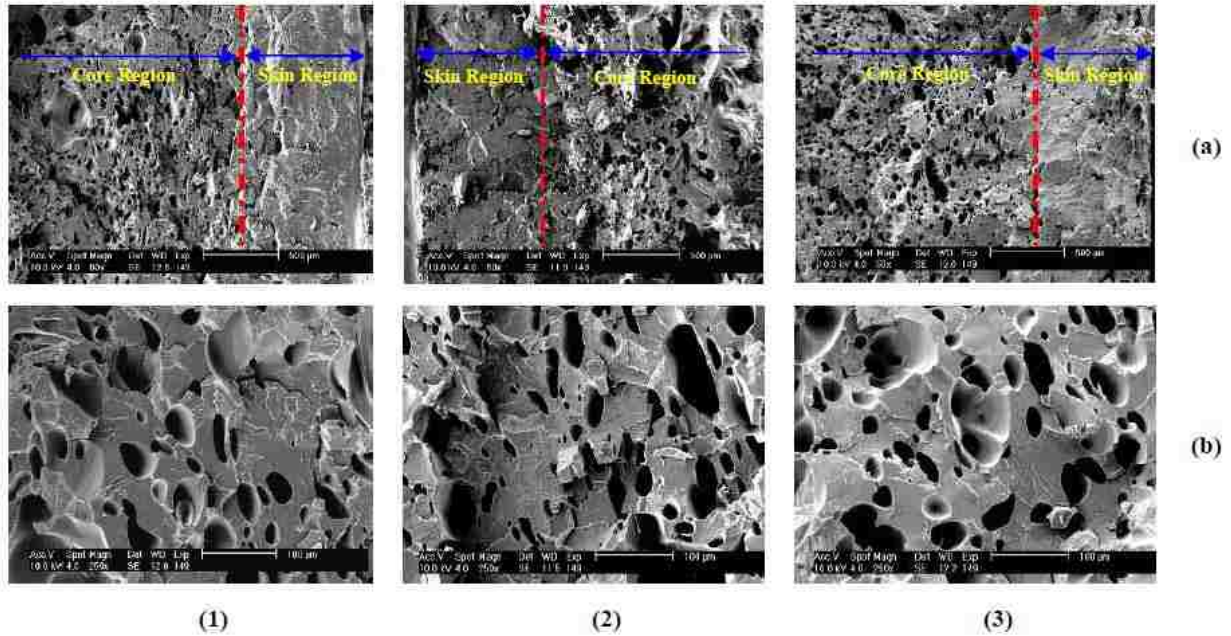


Figure 2.11 SEM graphs with a (a) smaller and (b) larger magnification for moulded sample prepared for shot size of (1) 46, (2) 50, (3) 52 mm [26].

2.5 MECHANICAL PROPERTIES OF MUCCELL® PLASTIC

2.5.1 EFFECT OF MUCCELL® PROCESS ON MECHANICAL PROPERTIES

The part mechanical properties are influenced due to the existence of cells. Previous studies have indicated that the part bend strength of the microcellular part close to the solid one. Therefore, the MuCell® can be used to produce the inner structure part. However, the tensile strength exhibits a decreasing trend along with the increasing density reduction. A tensile test indicates that a 50% density reduction would result in a 50% loss of strength. Impact strength, on the other hand, is more sensitive to the variation of polymers. Thus, the results cannot be generalized. However, the impact strength of PVC foam experiment results show that the impact strength decreases linearly with foam density. It is worth mentioning that the impact strength of polymer added filler is

decreased less than one without any filler. This is because the percentage and properties of the filler have larger effect on the part impact strength [27-29]. Figure 2.12 shows the bend strength, tensile strength, and impact strength of PBT (30% glass fibre) on different weight reduction percentages.

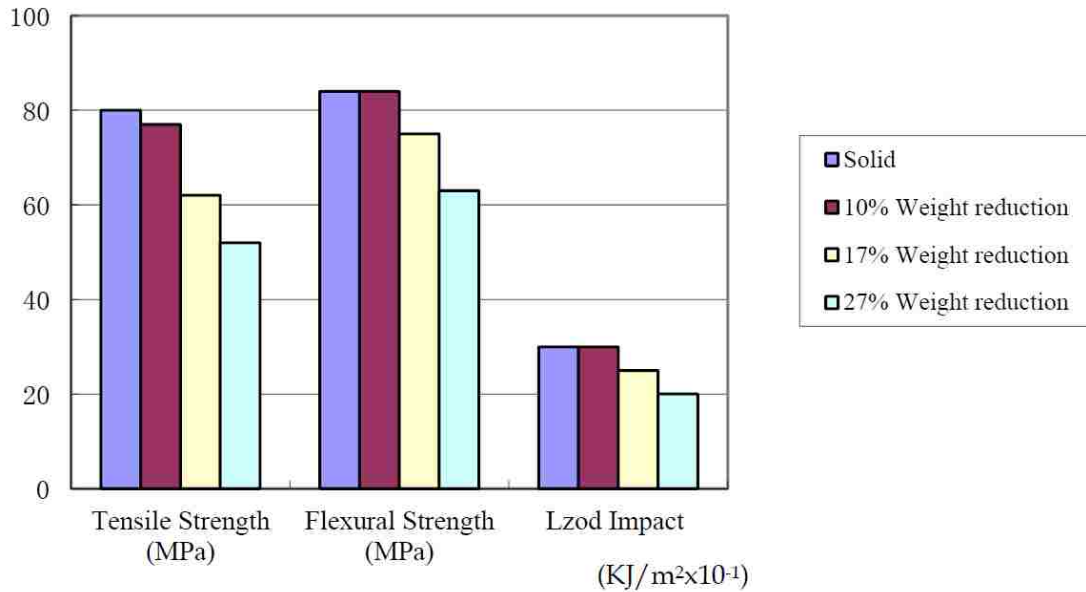


Figure 2.12 PBT mechanical properties with varying weight reductions [66].

2.5.2 RELATIONSHIP BETWEEN MICROSTRUCTURES AND MECHANICAL PROPERTIES

In order to understand how the morphology can be optimised to maximize resistance (for the different loading conditions during service) while minimizing material consumption, numerous studies have been conducted linking different features of the MuCell® microstructure to its mechanical properties. The main variables altered in these cases are density reduction, cell size, and non-cell thickness. The valuable results from the study by Michael et al. [30] are analyzed below, showing the effect of each variable on the tensile modulus, tensile strength, flexural modulus, and impact strength. The

material employed in their study was PC 2405 from Bayer, with CO₂ as the blowing agent.

2.5.2.1 EFFECTS OF MICROSTRUCTURE ON TENSILE PROPERTIES

The proportional contribution of the foam density, none-cell region thickness, and cell size to each of the tensile properties can be seen in Figure 2.13. It is evident that under tensile loading, the predominant parameter is density, and it has a major contribution to all the properties measured. However, almost 20% of the Young's modulus is explained by the none-cell region thickness. This would mean that using the same amount of material, the elastic modulus can be increased if the none-cell region thickness is increased.

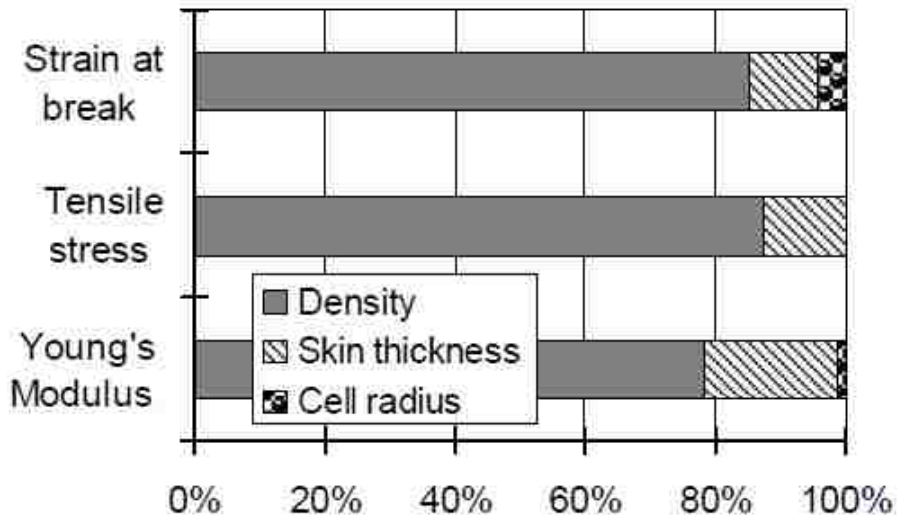


Figure 2.13 Proportional contributions of the MuCell® morphological parameters to the mechanical properties under tensile loading [31].

The cell size has almost no effect on the tensile stress but has a comparatively high relevance in the strain at break. It can also be observed that a finer cell size leads to a higher ductility of the material [31].

2.5.2.2 EFFECT OF MICROSTRUCTURE ON FLEXURAL PROPERTIES

The proportional contribution of the foam density, none-cell region thickness, and cell size to each of the flexural properties can be seen in Figure 2.14. As expected, the none-cell region thickness is more relevant in the flexural properties than in the tensile properties and has almost 50% more relevance in the modulus when the part experiences flexural load. A larger accumulation of material away from the neutral axis under bending load increases the moment of inertia of a structure.

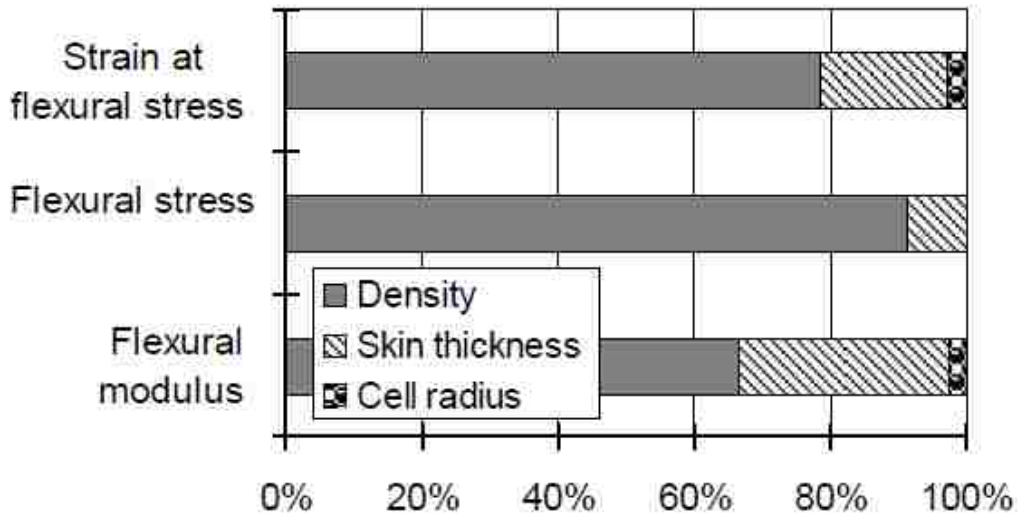


Figure 2.14 Proportional contribution of the MuCell® morphological parameters to the mechanical properties under flexural loading [31].

The relevance of none-cell region thickness in the strain properties under bending load is also larger. It has been proposed that the foamed cell structure impairs the relative movement of molecules [32]. As the deformation increases with increasing distance from the neutral axis, it is expected that a larger region of unimpaired movements (none-cell) will allow for larger deformations.

2.5.2.3 EFFECT OF MICROSTRUCTURE ON IMPACT PROPERTIES

The effects of MuCell® morphology on impact properties are illustrated in Figure 2.15. Comparatively, the none-cell region thickness has a larger relevance than the density and the cell size, both in the maximal impact force and in the energy absorbed during impact. Interestingly, the relevance of none-cell region thickness is larger in the energy absorbed, which means that it is possible to have lighter parts without sacrificing impact resistance if the none-cell region thickness is large enough. This means that the cell size has a lower effect compared to the none-cell region thickness and the foam density, but it can counteract the crack propagation.

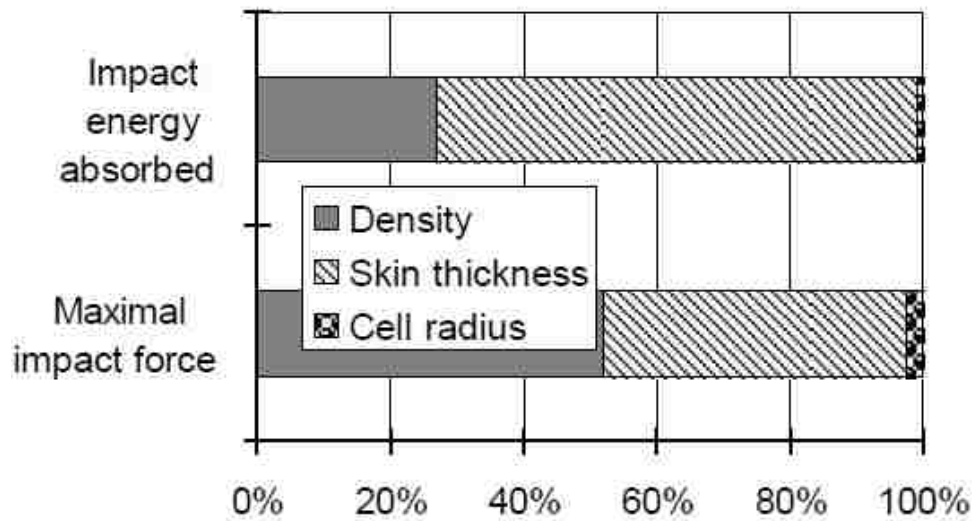


Figure 2.15 Proportional contribution of the foam morphological parameters to the mechanical properties under impact loading [31].

2.5.3 FATIGUE BEHAVIOUR

Since the industrial manufacturers tend to apply MuCell® on glass fibre composites, the behaviour of glass fibre inlays according to the applied force is becoming

an important factor affecting the strength of the moulded part. Various researchers have studied the failure mechanism of glass fibre composites either in tensile experiments [33-35] or in fatigue tests [36-37].

In tensile experiments, the failure mechanism is generally assumed to consist of the following steps:

1. Cracks initiate at fibre ends.
2. Cracks propagate in the matrix along the interface, thus leaving a thin layer of matrix material adhered to the fibre. Only in systems with poor fibre-matrix bonding does the interface itself fail.
3. Matrix cracks grow from the interfacial cracks, possibly after the generation of matrix plastic deformation.

The Schematic of the tensile failure mechanisms is illustrated in Figure 2.16.

In fatigue tests, four stages are usually seen:

1. Initiation of local weakening due to cyclic deformation, generally initiating at the locations of highest stress intensity, the fibre ends [38].
2. Initiation of crack occurs at the fibre end.
3. Crack growth due to cyclic loading. Local modes of crack extension depend on local fibre orientation, matrix ductility, and the degree of interfacial adhesion. The mechanisms during breakdown of the composite are fibre matrix separation along the interfaces of fibres oriented parallel to the crack, deformation and fracture of the matrix between fibres, fibre pull-out, and fracture of transverse (to the crack direction) fibres.

4. Fast (instable) crack growth in the last load cycle, which should be comparable to failure in a tensile test.

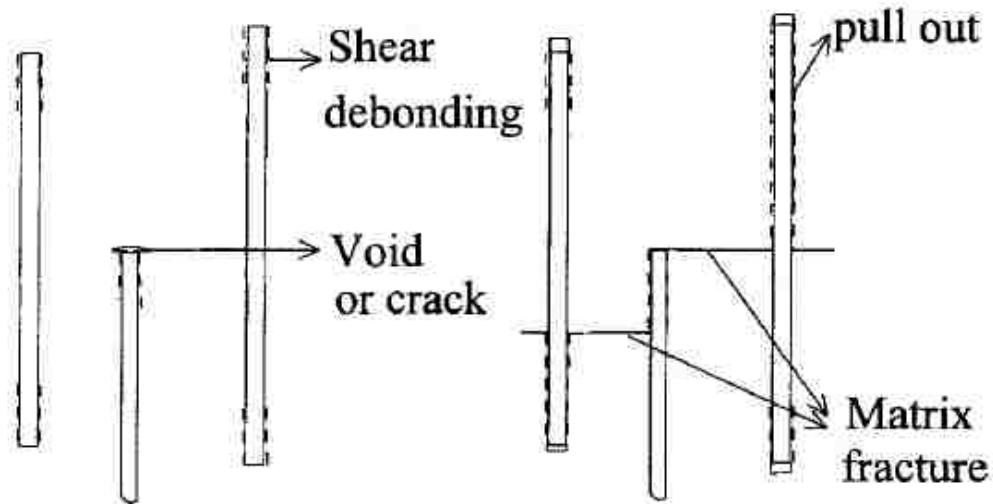


Figure 2.16 Failure mechanism in a tensile experiment. Left: Initiation of crack. Right: growth of crack [67].

A different fatigue mechanism was mentioned by Horst and Spoormaker [35] based on their experimental work:

1. Initiation of damage at the fibre ends.
2. Growth of this damage into voids, accompanied by debonding.
3. The voids grow into micro-cracks, which may remain bridged by either drawn matrix material or unbroken fibres.
4. The debonding relieves the constraint to which the matrix was subjected, which can therefore deform much more easily, forming bridges between the crack walls.
5. The bridged crack grows, until a critical size is reached and the specimen fails.

The Schematic of the fatigue mechanisms is illustrated in Figure 2.17

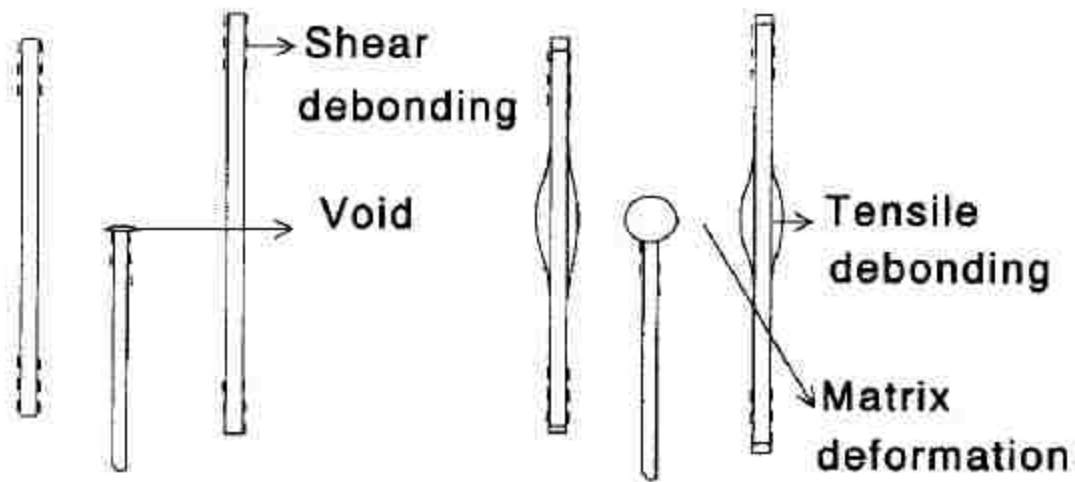


Figure 2.17 The assumed fatigue mechanism. Left: Initiation of damage. Right: development of damage, tensile debonding resulting from lateral contraction of the matrix [35].

Another interesting observation had been achieved by T Harmia [39]. A “heated area” was observed using a thermograph camera at the beginning of the stable crack growth (Figure 2.18), and it is suggested that the heated area corresponds to the adhesion quality of the glass fibres and matrix. When relatively poor adhesion between the fibres and the matrix is found, debonding and the resulting fibre pull out comprise the main fibre-related failure mechanism. In the case of low adhesion, relatively low loads (or strain) enable micro-cracks to grow in the interface of the glass fibres and matrix, which results in the whole or partial debonding of the glass fibres from the matrix. When debonding occurs, these debonded fibres oscillate in the tact of the cyclic loading in “caves” that result from the debonding process (Figure 2.19). Because of this movement and the friction between the fibres and the matrix, small local heating is caused in the matrix.

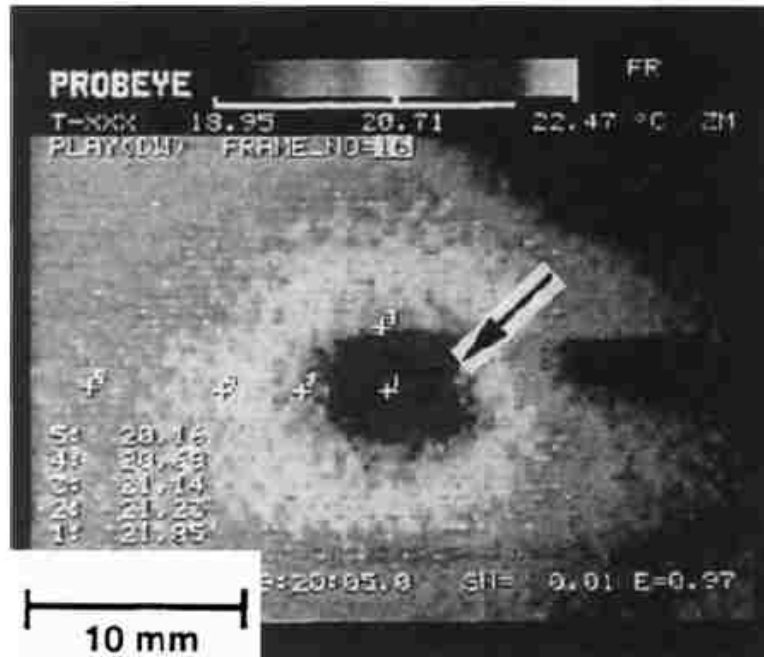


Figure 2.18 Heated area of LGF PP with poor bonding between glass fibre and matrix.

The arrow shows the position of the crack tip [39].

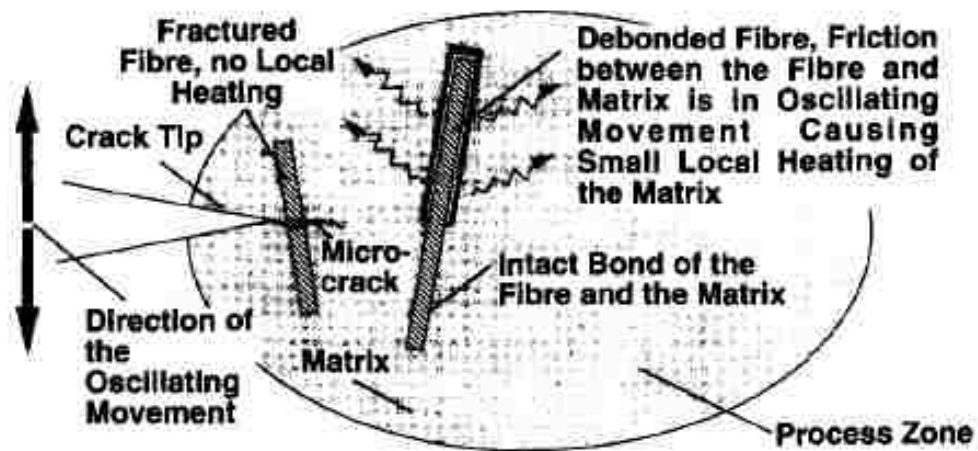


Figure 2.19 Schematic of the heat development in fatigue, when fibre/matrix debonding and fibre fracture was occurring [39].

2.6 ADDITIVES IN MUCELL® PLASTIC AND THEIR EFFECTS ON MECHANICAL PROPERTIES

2.6.1 FIBRE ADDITIVES

The lower manufacturing cost and the enhanced tensile behaviour of fibre-reinforced composites are achieved at the expense of other properties such as ductility and impact resistance [40-42]. Since the microcellular process is known to improve the impact strength, toughness, and fatigue life, the use of the microcellular process on the fibre-reinforced composites would lead to a great improvement in the mechanical property of the composite.

Many research efforts have been conducted to study the effect of processing parameters on the microstructure of the MuCell® materials in various processes [43]. However, very few investigations have been conducted to study the influence of added fibres on the microstructure of microcellular composites.

All mechanisms of cell formation take place mostly in the amorphous regions of the polymer, which is an after-effect of the diffusion and absorption processes [44]. Nucleation in heterogeneous polymers may occur both heterogeneously at the interface between the polymer and the second phase and homogeneously in the free volume of the single matrix phase. Heterogeneous nucleation occurs when a bubble forms at an interface between two phases, such as a polymer and an additive [45]. The gas absorption behaviour of filled and unfilled polymers was investigated to explain heterogeneous nucleation in filled polymers. It was found that filled polymers absorb more gas compared to unfilled ones. The gas accumulates between polymer and filler and helps to create nucleation during the foaming process [46].

An opposite observation was made by Matuana-Malanada et al. [47]. It was observed that for the composites with treated fibres, both the solubility and diffusivity of CO₂ in the composite decreases as the fibre content in the composite increases. The decrease in the solubility of CO₂ indicates that only the amorphous region in the composite absorbs the gas. Adding fibres in the composite tends to decrease the volume of amorphous material available for diffusion. Moreover, fibre regions in the composites obstruct the movement of CO₂ molecules and increase the average length of the paths they have to travel.

2.6.1.1 GLASS FIBRE ADDITIVES

The original purpose of adding glass fibres to polymers was an improvement in stiffness, strength, and heat distortion temperature compared to unfilled thermoplastics. In particular, the reinforcement of thermoplastic compounds by glass fibres has received special attention because of their use in a variety of engineering applications in both the chemical and automotive industries.

Observations from Din and Hashemi's study indicate that the addition of glass fibres enhanced the ultimate tensile strength and modulus of the polymer composites. The results can be concluded from Figure 2.20 and Figure 2.21 [48].

The effect of the glass fibre content on glass fibre-reinforced PC/ABS composite using the MuCell® process had been investigated by Bledzki and Gajdzik [49].

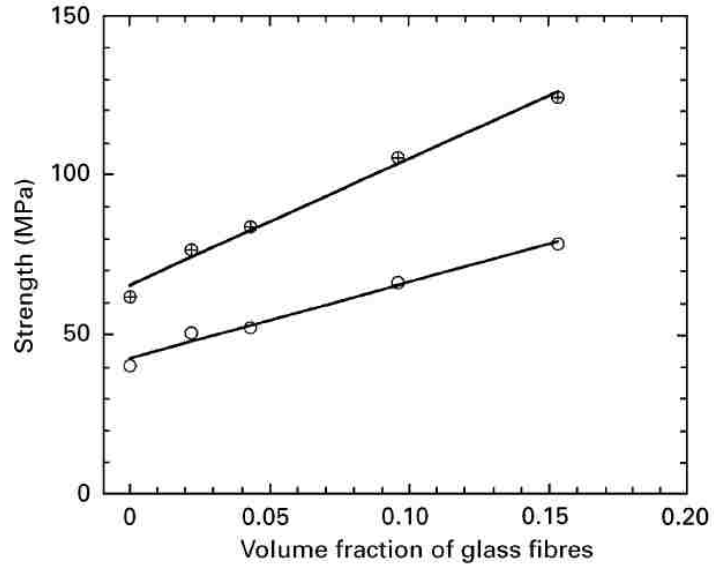


Figure 2.20 (O) Tensile strength and (+) flexural strength versus the volume fraction of the glass fibres [48].

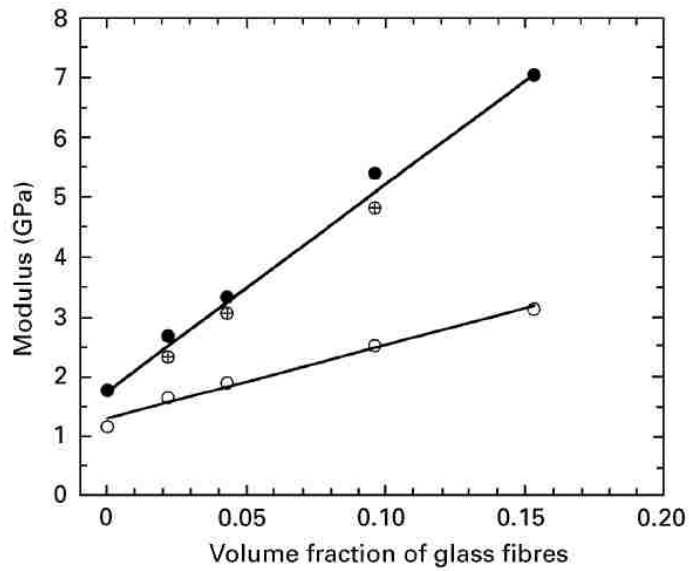


Figure 2.21 The tensile modulus; (O) apparent elastic modulus, (•) actual elastic modulus and (+) flexural modulus versus the volume fraction of glass fibres [48].

One result from their observations was that the specific flexural modulus of the 20 wt. % glass fibre-reinforced PC/ABS moulded using the MuCell® process is significantly higher than the unreinforced one. Moreover, as the density reduction of the microcellular foam glass fibre-reinforced PC/ABS increased, the specific flexural modulus increased linearly. There is an improvement of up to 10% in the case of higher density reduction combined with greater cell size (Figure 2.22).

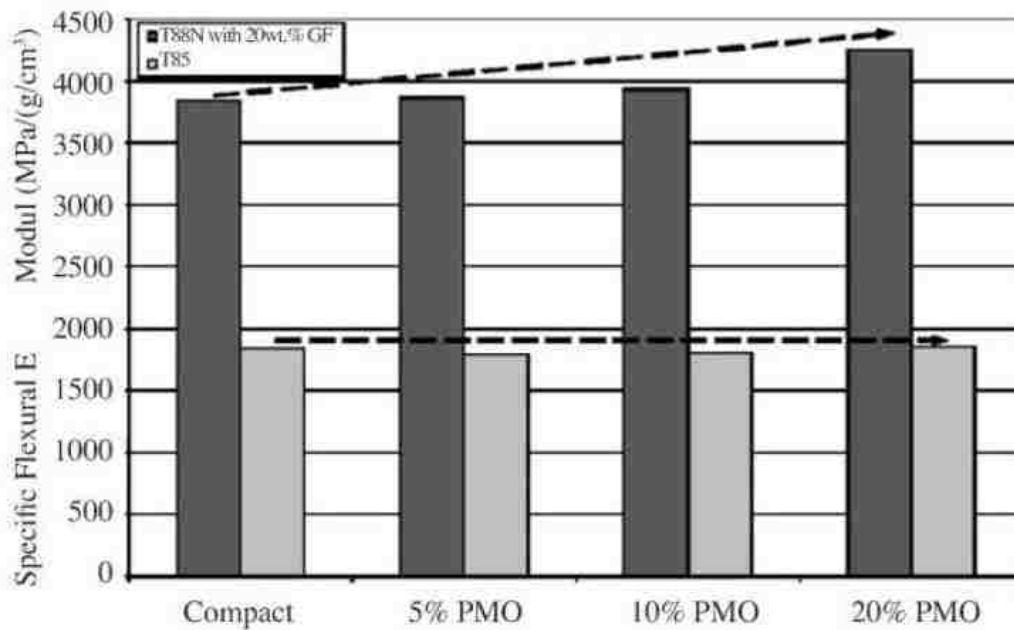


Figure 2.22 Specific flexural modulus of 20 wt. % glass fibre reinforced and unreinforced PC/ABS versus density reduction [49].

One possible disadvantage of reinforcing the glass fibre in the composite was also found during their work. The adhesion between glass fibres and matrix seems to be insufficient. This phenomenon can be observed in Figure 2.23 (d–f), where the glass fibres appear to lay between the cells and demonstrate a weakened interfacial character, indicating a failure at the interface [49].

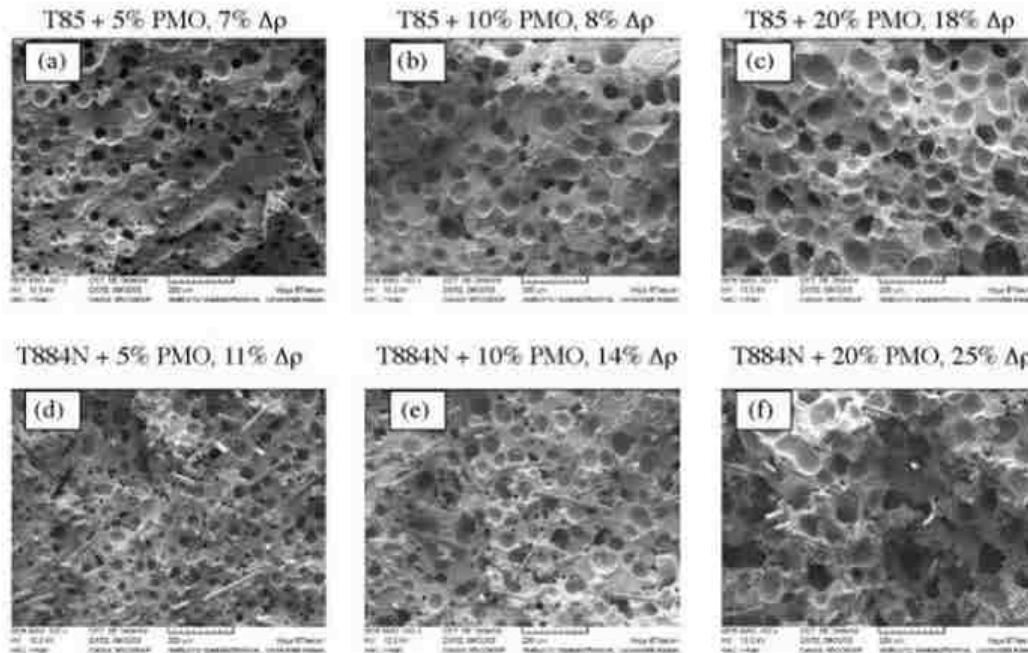


Figure 2.23 SEM micrograph of the centre area of, a-c) microcellular foam unreinforced PC/ABS T85 with density reduction from 7% to 18%; d-f) microcellular foam glass fibre reinforced PC/ABS T884N with density reduction from 11% to 25% [49].

It is well known that as the length of the glass fibres increases, the material properties of the polymer are greatly improved. However, there is a problem when long fibres are included, especially in products using the MuCell® process. Due to the introduction of the foaming agent through direct gas injection, a complete mixture of the polymer and foaming agent must be achieved through the polymer injection moulding screw. The high shear strength during the mixing process has often been found to be excessively damaging to reinforcing glass fibres.

Recently, moulding equipment modified for microcellular injection moulding to solve the potential damage to reinforcing glass fibres in moulded parts has recently become available.

In order to determine the effectiveness of this new process, a study was conducted by Frank and Jaarsma [50]. In their study, two plastic materials were evaluated where the first was polypropylene reinforced with 40% long glass fibres, 11 mm in length, and the second material was a nylon 6 resin, reinforced with 50% long glass fibres, 11 mm in length.

Moreover, two different screw systems were utilized. The first screw was designed as “standard” and is the traditional design used for microcellular moulding, while the second one was designated as the “LGF” screw (Figure 2.24). In order to compare to gain a better understanding of the difference between the products made by the two screws, the outer surfaces of the samples produced by each screw are illustrated in Figure 2.25.

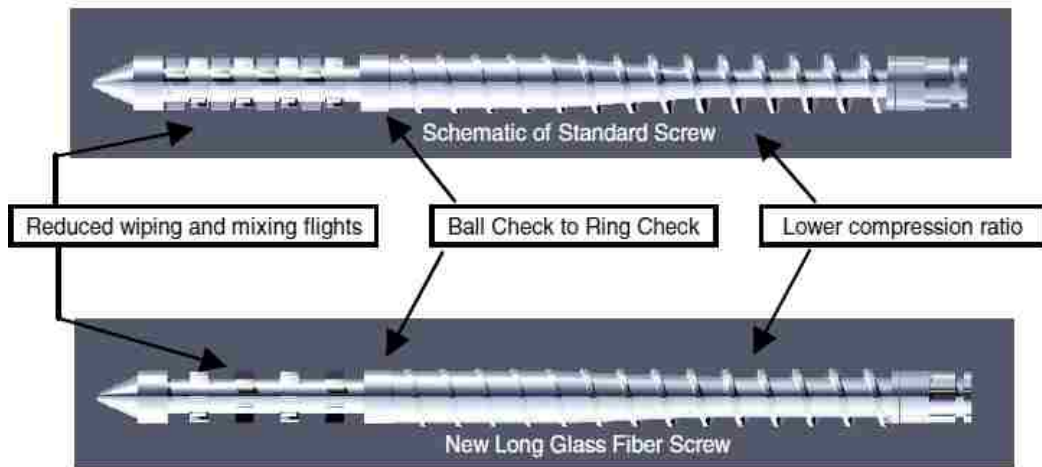


Figure 2.24 Schematic comparison of standard microcellular screw with LGF screw [50].

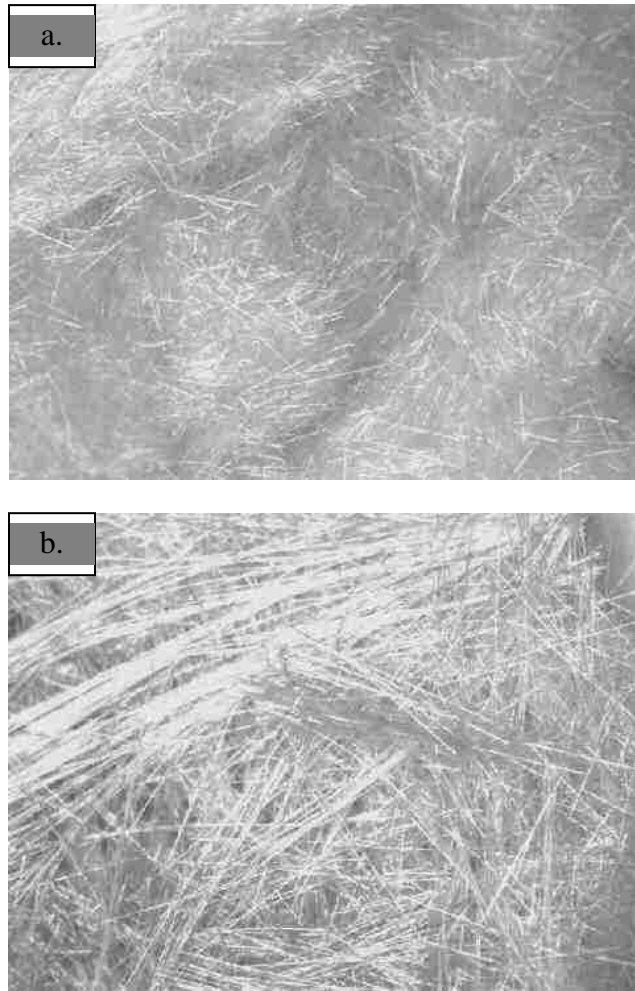


Figure 2.25 Glass Fibers – (a) Standard Screw (b) LGF Screw [50].

Tensile, flex, and impact tests were also employed on the moulded parts. The tested specimens were produced in a single shot, thus insuring all test specimens were moulded in an identical manner. The test results are shown in Table 2.4.

As can be seen by the comparison of the test results shown above, the new LGF screw and processing technology available for the microcellular moulding of long glass fibre-reinforced plastics is shown to be very effective for both polypropylene and nylon materials. Glass fibre length retention was increased up to 115%—more than double in average length. The longer glass fibres bring improvement in every mechanical property

tested, most notably in multi-axial drop impact, which increased by 42%. The data further indicate that these improved properties were obtained while maintaining excellent warpage reduction, microcellular structure, and part weight reduction [51].

Table 2.4 Summary of fibre length and property changes for polypropylene and nylon comparing traditional screw with LGF screw [50].

Test	% Change Polypropylene	% Change Nylon
Fibre Length	114.9%	24%
Drop Impact	23.7%	42.4%
Notched Impact	8.1%	12.8%
Flex Strength	7.5%	5.2%
Flex Strain	-0.9%	-4.9%
Tensile Strength	9.9%	8.8%
HDT Deg. C	0.7%	1.1%

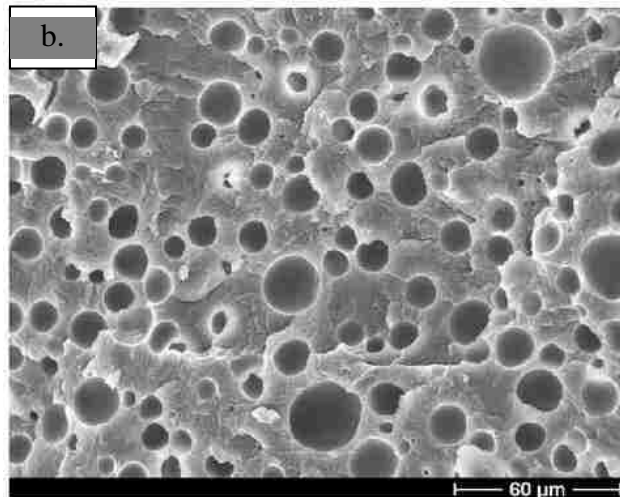
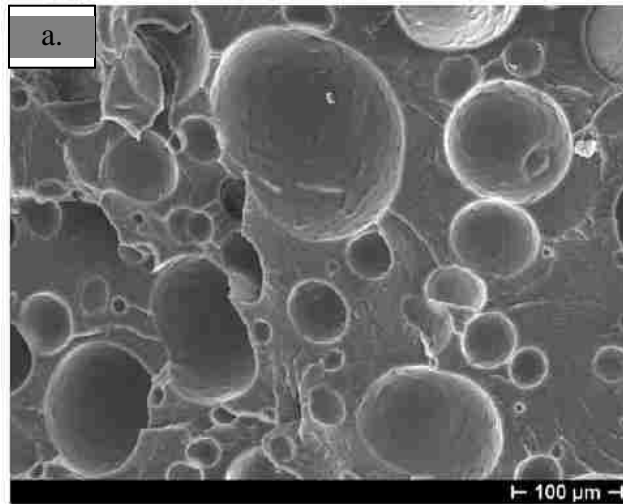
2.6.2 NANO-CLAY PARTICLE ADDITIVES

In order to achieve superior properties such as enhanced mechanical and thermal properties, improved barrier performance, and flame retardancy, nano-clay particles are included into the polymer during manufacturing [52-53].

Recent studies have shown that the addition of nano-clay fillers greatly increases the viscosity of the polymer [52]. On the other hand, blending SCF into the polymer melt effectively reduces the viscosity and the glass transition temperature of the polymer melt, as well as the interfacial tension [53]. Hence, adding nano-clay into the SCF renders a method for tailoring the rheological and surface properties of the polymer to facilitate better microcellular formation and improved mechanical properties, thus creating an

opportunity to take advantage of the synergistic effect of combining the microcellular process with nano-composite materials.

From Yuan and Turng's study, it can be concluded that the nano-clay behaves as a microcell nucleation agent and promotes smaller cell size and larger cell density, which are desirable for attaining better normalized toughness (Figure 2.26 and Figure 2.27) [54].



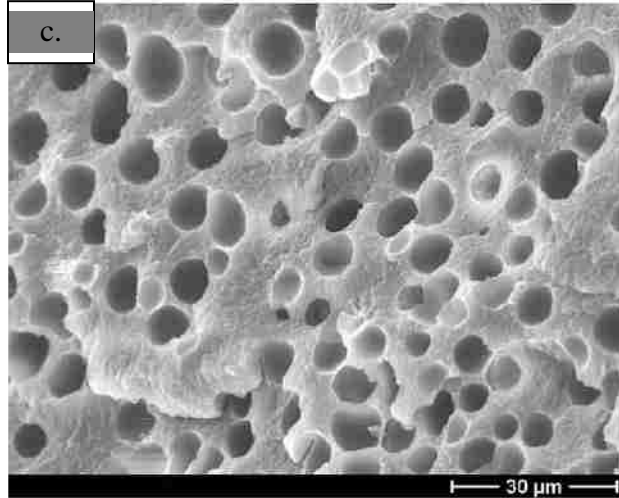


Figure 2.26 Cross-section view of MuCell® sample moulded with (a). Neat PA 6 resin (b). 5% w.t. nano-clay reinforced PA 6 resin (c). 7.5% w.t. nano-clay reinforced PA 6 resin

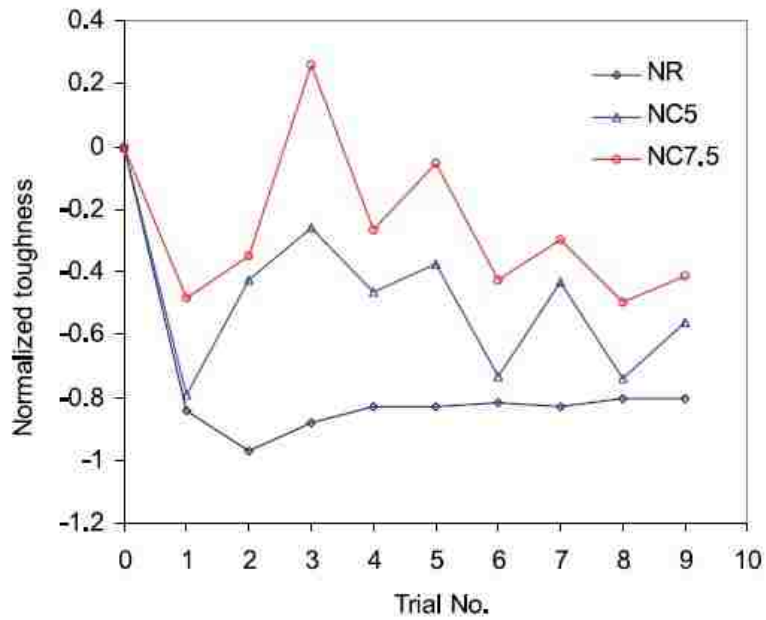


Figure 2.27 Normalized toughness of sample moulded with different content of nano-clay [54].

2.7 VIBRATION WELDING

There are a number of welding technologies for polymer used in the market today including vibration welding, ultrasonic welding, hot plate welding, and spin welding. Of these, vibration welding is the most common for large parts with complex parting lines, such as air intake manifolds, and is of more interest with microcellular foamed parts as these larger parts typically achieve greater benefits from the MuCell® process. In vibration welding, the plastic parts are fixtured in such a manner that the weld surfaces are brought into contact under pressure. The weld surfaces are then rubbed together in either a linear or orbital manner at a given frequency, pressure, and time. As the parts move, friction builds, causing the surfaces in contact to melt. Once sufficient material has been melted, the movement between parts stops and the molten plastic at the interface cools and solidifies to form a bond between the parts. The process is shown schematically in Figure 2.28.

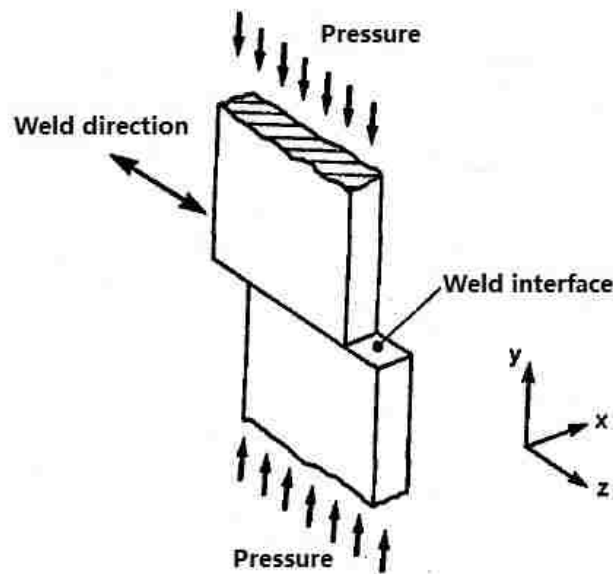


Figure 2.28 Schematic of the weld process [68].

2.7.1 ADVANTAGES AND SHORTCOMINGS

The vibration welding process can ideally be employed on thermoplastic parts along flat seams. The process can also accommodate seams with very small curvature. This technique has many potential advantages for joining large flat-seamed thermoplastic parts: (1) relatively short cycle times, (2) simple equipment, and (3) insensitivity of the process to weld surface preparation. In contrast to adhesive bonding, no foreign material is introduced; therefore, the weld interface is of the same material as the parts to be welded. Also, in contrast to hot-tool welding, in which the interfaces to be welded are heated conductively by direct contact with a hot tool, the heating is very localized. In addition, the vibration welding process is more controllable and is much less likely to be overheated at the interface, resulting in material degradation [55].

Besides these benefits, the main shortcoming of this process is that it is limited to near flat-seamed parts, although stepped parallel seams can also be welded. Also, this process is not suited to welding low-modulus thermoplastics, such as some thermoplastic elastomers.

2.7.2 TYPICAL APPLICATIONS FOR VIBRATION WELDING

Recently, the most demanding application of vibration welding was the all plastic automotive bumper that could withstand an 8 km/h impact. Other automotive applications of this technology include the welding of headlight, taillight, and instrument panel assemblies involving welds of polycarbonate to itself and to acrylic, acetal gasoline reservoirs, 30% glass fibre-filled nylon brake fluid reservoirs, and polypropylene compartment access doors welded in two planes. In the appliance industry, this technology has been used for assembling glass- and particulate-filled polypropylene

washer and dishwasher pumps and particulate-filled soap dispensers and dishwasher spray arms. It has also been applied on welding chain saw motor housings made of 30% glass fibre-filled nylon [55-56].

2.7.3 TYPICAL STRUCTURE OF THE WELD REGION

The welded interface achieved by vibration welding normally exhibits a heat affected zone (HAZ) whose structure and property is always related to welding pressure. For example, low welding pressure produces a thicker HAZ and more random fibre orientation [57]. It is well known that a thicker HAZ is associated with higher weld strength. Also, for glass fibre-reinforced material, HAZs with more random glass fibres are considered to achieve higher weld strength [58].

The most detailed study of the microstructure of the weld interface was reported by Schlarb and Ehrenstein [59], who obtained polarization micrographs of polypropylene butt welded joints. They observed that the weld interface produced at high pressure consists of two layers: an inner layer and a band of deformed spherulites. On the other hand, the weld interface produced at low pressure has three microstructural zones, consisting of an inner layer, a recrystallized zone with spherulites of different sizes, and a transition zone with deformed spherulites. In addition, the entire interface produced under low pressure is about three times thicker than the two-layer structure produced under high pressure. Schlarb and Ehrenstein [59] suggested that the critical factor for weld strength is the pressure rather than the amplitude or another parameter.

As illustrated below, molecular orientation and crystal phase studies show that the central HAZ layer (HAZ-I) is a recrystallized layer, which originates from a molten polymer core. The outer layer (HAZ-II) is a deformed layer, which originates from

rubbery polymer deformation above T_g (Figure 2.29). The morphology of the recrystallized layer is greatly influenced by the processing conditions. The content of γ crystal phase was higher in the recrystallized layer than in the bulk phase. A slight elevation of the γ -phase was also observed in the deformed layer. Molecular orientation in the recrystallized layer was higher than in the deformed layer.

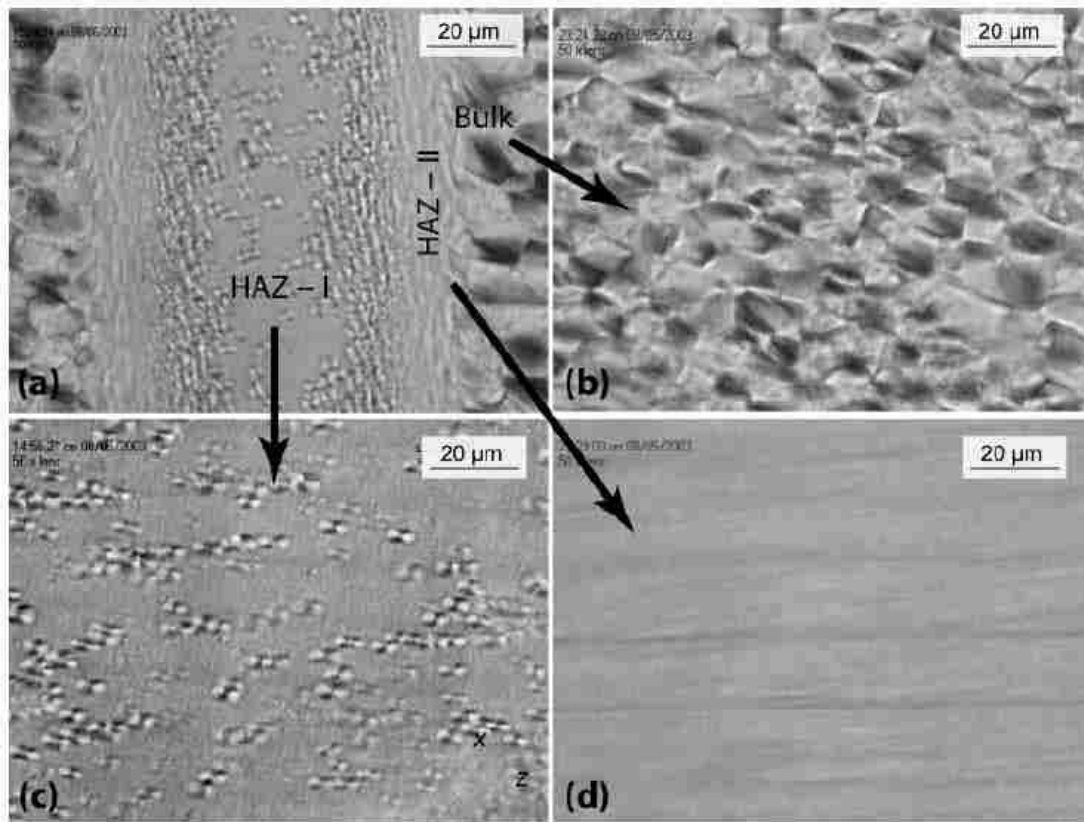


Figure 2.29 Polarized transmitted light micrographs of microtomed sections of unreinforced polyimide-6 (a) HAZ-I (b) Bulk layer (c) deformed layer [68].

The SEM observation on an etched HAZ sample shows a distinct etched line at the boundary between the recrystallized layer and the deformed layer, which again suggests that the HAZ-I and HAZ-II are formed from different processes (Figure 2.30). During tensile loading, the welded samples tend to fail at the interface between the

recrystallized layer and the deformed layer, as shown in Figure 2.31. The crystallinity of the deformed layer is higher than that of the bulk phase. The recrystallized layer obtained at high vibration amplitude and high welding pressure has the lowest crystallinity, which yields the lowest weld strength. The results suggest that the determining factor for weld strength is the crystallinity of the recrystallized layer.

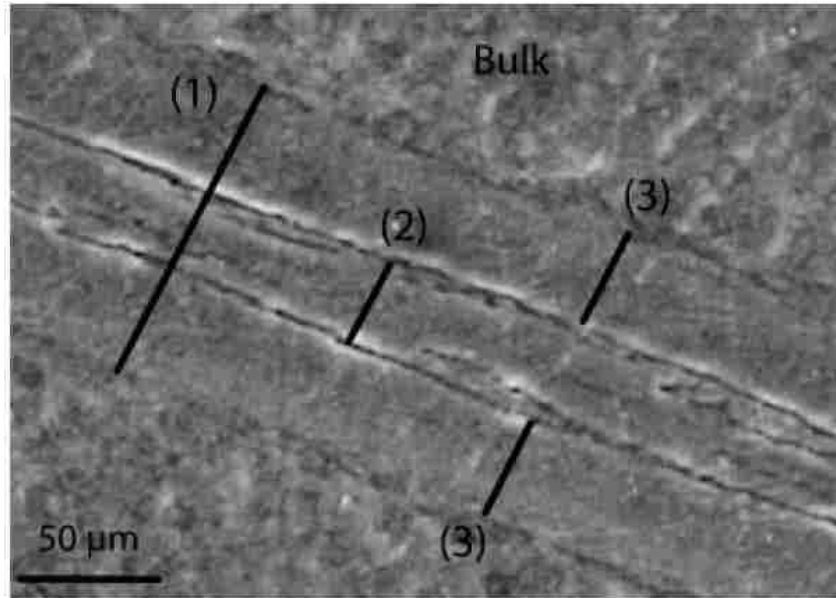


Figure 2.30 SEM image of etched surface of HAZ from unreinforced polyamide-6 welded At 5 MPa. (1), (2), and (3) indicate HAZ, HAZ-I, and HAZ-II, respectively [68].

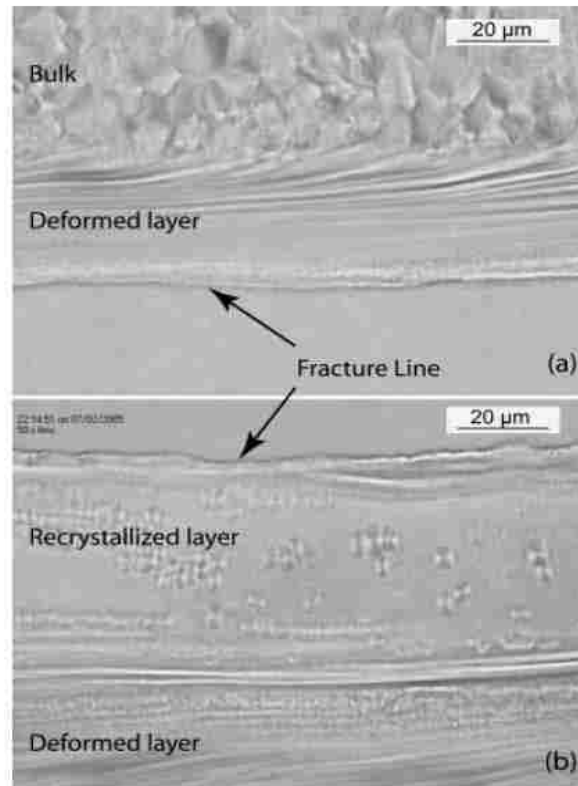


Figure 2.31 Fracture surface of HAZ: (a) failed surface of the deformed layer; (b) the other failed surface of the recrystallized layer [68].

2.7.4 VIBRATION WELDING FOR GLASS FIBRE REINFORCED COMPOSITE

As illustrated in Figure 2.32, for MuCell® plastic, the tensile strength loss at the weld joint of the glass fibre-reinforced material is less than that of the one of unfilled material, and for plastic moulded using the MuCell® process the trend is observed to be more significant at higher weight reduction levels [25].

However, other researchers hold different opinions. Bates et al. [60] mentioned in their study that when joining glass fibre-reinforced composites through vibration welding, the strength of the overall weld is gravely dependent on the fibre glass inlays' alignment and the number of fibres breaching the welding joint and heat affected zones.

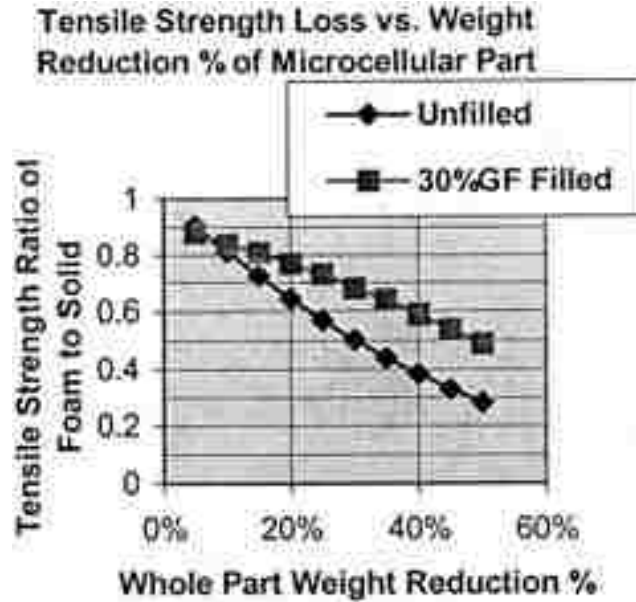


Figure 2.32 Comparison of tensile strength loss for unfilled and 30% glass fibre filled PA6 with different weight reductions [25].

In order to establish an efficient way to determine the orientation of fibres in the polymer matrix, vibration welded joints of polyamide-6 (PA-6) reinforced with 30 wt. % glass fibres were studied by Kamal et al. (Figure 2.33 and Figure 2.34) [61].

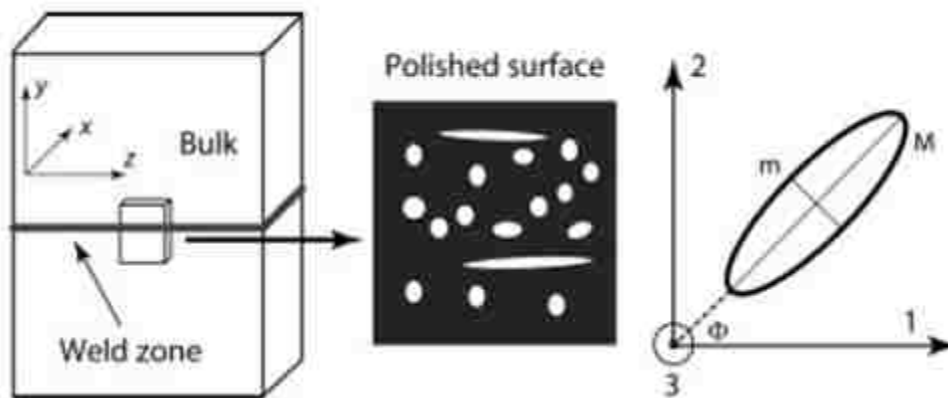


Figure 2.33 Elliptical cross section of a cylindrical fibre: in this case, coordinates 1, 2, and 3, correspond to z, x, and y, respectively [61].

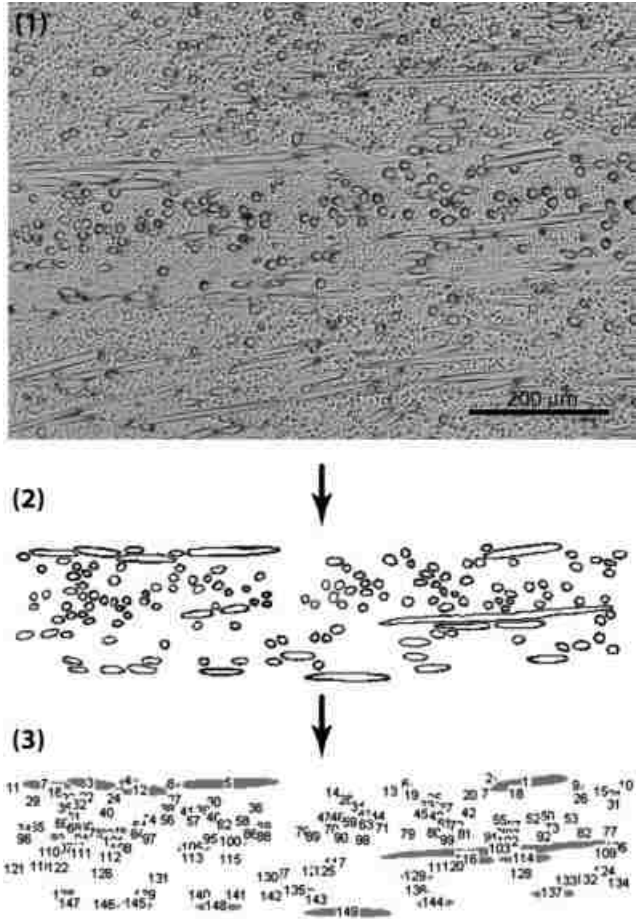


Figure 2.34 Treatment of images to obtain the fiber orientation tensor. (1) Micrograph (2) binary image (3) image analysis [61].

To determine the orientation of the fibres present in the weld section, a naming convention is devised for the direction vector of each fibre in space. Each vector is defined as a second-order symmetric tensor:

$$a_{ij} = \begin{pmatrix} a_{11} & a_{21} & a_{31} \\ a_{12} & a_{22} & a_{32} \\ a_{13} & a_{23} & a_{33} \end{pmatrix}$$

where each component a_{ij} represents alignment along a major axes, whereas components a_{ij} represent directions off the main axes. Whereas a_{12} , for example represents a vector off of axis 1 in the direction of axis 2.

Each of the tensor values can be easily calculated from the shape and orientation of the fibre glass profile data obtained from a selection of the sample.

2.7.4.1 DETERMINING FIBRE ORIENTATION

As illustrated above, the effect of friction welding on fibre orientation was observed on 30 wt. % glass fibre-reinforced PA-6 through friction welding (along the z axis). Two samples were taken from each plaque. One of the samples was cut through the middle, exposing the centerline of the weld, while the other one was cut through one quarter of the thickness (details are outlined in Figure 2.35).

Table 2.5 Component of the second order orientation tensor in terms of angles and elliptical axes dimensions: m, minor axis and M major axis [61]

Component	Expression
(a_{11})	$(1-m^2/M^2) \cos^2\phi$
$(a_{12}) = (a_{21})$	$(1-m^2/M^2) \cos^2\phi \sin\phi$
$(a_{13}) = (a_{31})$	$m^2/M^2(M^2-m^2)^{1/2} \cos\phi$
(a_{22})	$(1-m^2/M^2) \sin^2\phi$
$(a_{23}) = (a_{32})$	$m^2/M^2(M^2-m^2)^{1/2} \sin\phi$
(a_{33})	(m^2/M^2)

Each sample is then observed and analyzed using the method outlined in Table

2.5

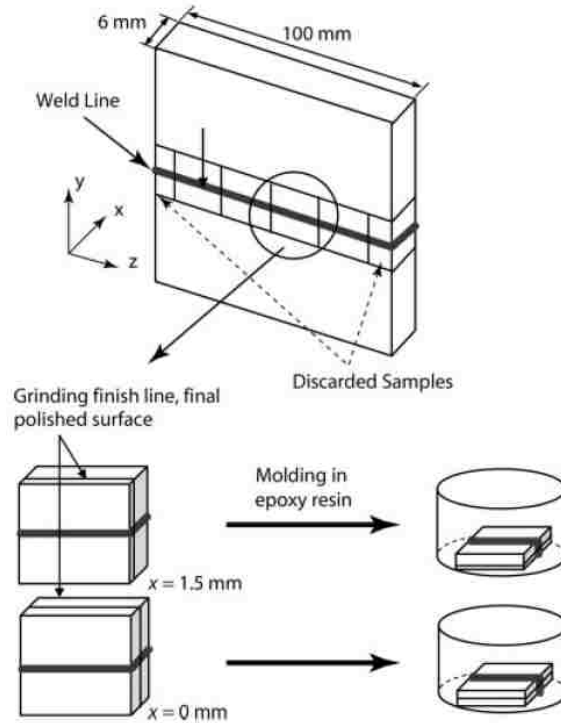


Figure 2.35 Specimen preparation for fiber orientation measurement [61]

When looking at fibre orientation, the heat affected zone of each vibration welding condition is compared with the bulk fibre orientation for the sample. The characteristics of the bulk material are used as controls to determine the change in each condition. In the bulk section, the fibres tend to (80%) orient in the direction of material flow during moulding, which is parallel to the vibration direction, whereas 14% of glass fibre is observed to be normal to the weld (a_{yy} direction), and 6% is normal to the plate. In conclusion: $a_{zz} > a_{yy} > a_{xx}$.

Looking at the fibre orientation of each of the samples' HAZ (summarized in Figure 2.37), it can be seen that the largest amount of fibre reorientation occurs for samples welded at high pressure and low amplitude.

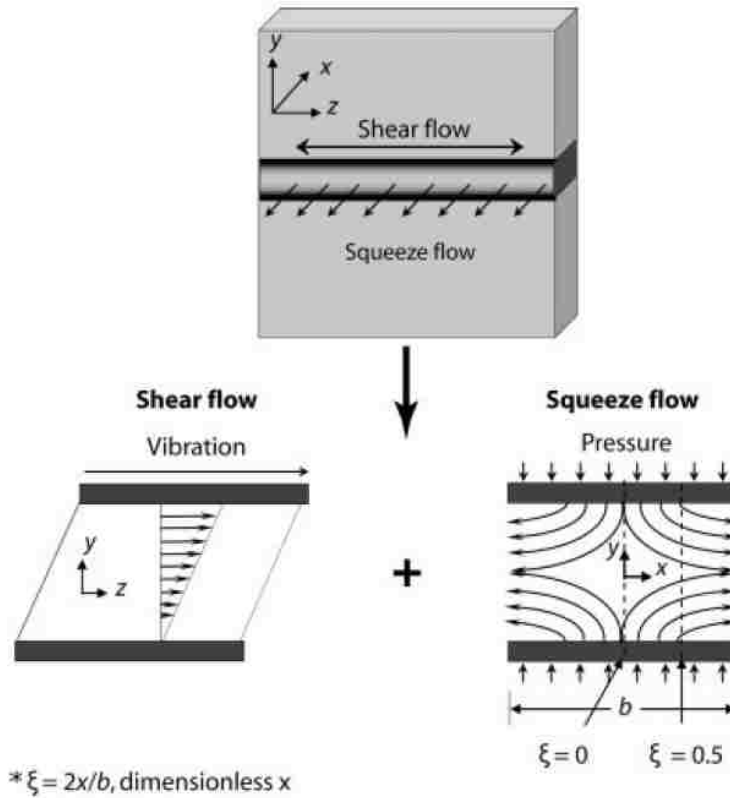
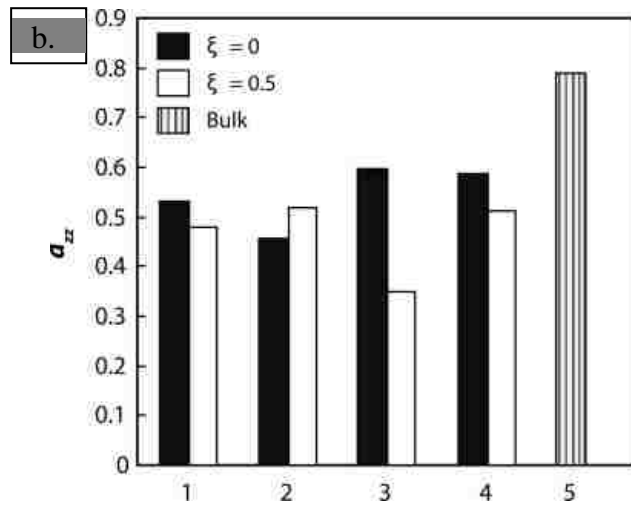
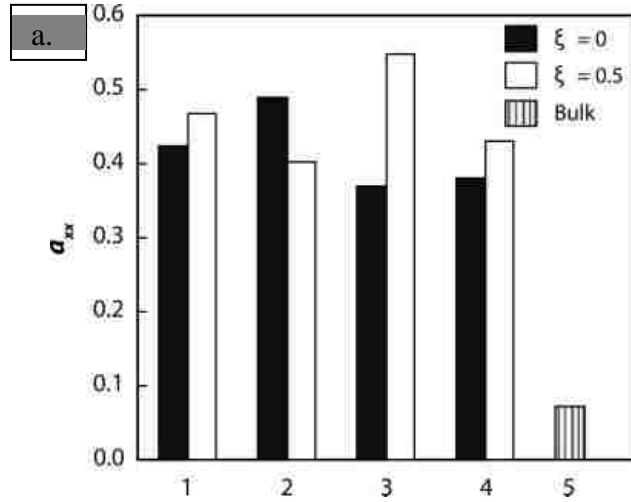


Figure 2.36 A schematic of shear and squeeze flow during the vibration welding process. [61]

All the samples show a decrease from the main bulk fibre directions in the z axis (along the weld line) and a sharp increase in the x direction (normal to the plate). This can be mainly attributed to the squeeze flow of the material during welding. The orientation along the y axis (breaching the weld surface) also decreases from the bulk into the HAZ. The fact that the high pressure, low amplitude sample showed the most

realignment in the y direction suggests a correlation between the amount of pressure flow in the sample and the re-alignment in this direction [61].



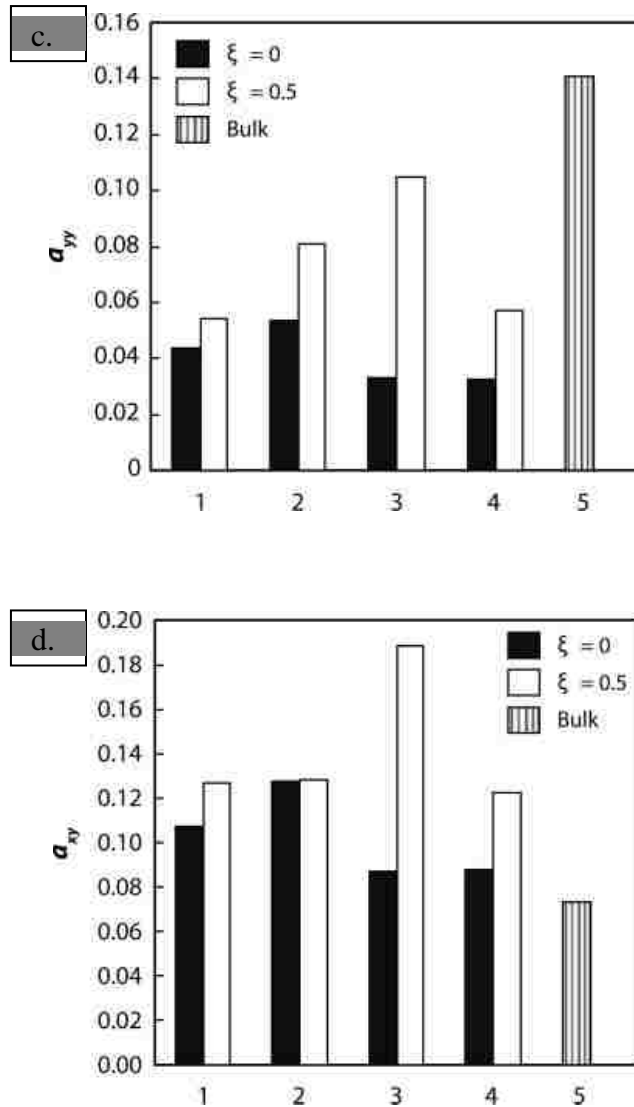


Figure 2.37 Average amount of fibre with (a) a_{xx} orientation (b) a_{zz} orientation (c) a_{yy} orientation (d) a_{xy} orientation at HAZ welded at different welding parameters (1) HAZ welded at 0.6 MPa and 1 mm. (2) HAZ welded at 0.6 MPa and 1.78 mm. (3) HAZ welded at 5 MPa and 1 mm. (4) HAZ welded 5 MPa and 1.78 mm. (5) Bulk [61].

Figure 2.38 illustrates the tensile test results of different samples. It can be seen that low welding pressure yields higher weld strength than high welding pressure. However, the results also show that low amplitude, combined with high pressure, can yield strength almost as high as that of low pressure. Gehde et al. [62] also observed that higher welding pressure along with higher amplitudes could be attributed to a weaker vibration weld joint. A comparison between reinforced and unreinforced samples moulded and welded under similar conditions indicates that, contrary to common assumptions, the weld joint between the reinforced samples exhibits lower tensile strength than joints corresponding to unreinforced samples. Gehde et al. [62] reported similar observations, indicating a decrease in weld strength in the presence of glass fibre reinforcement.

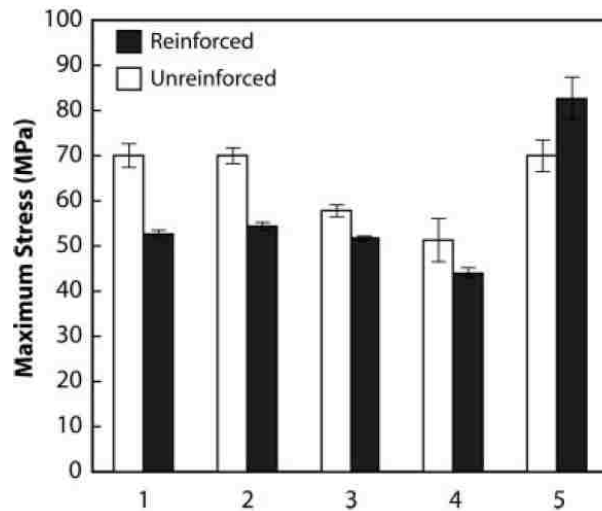


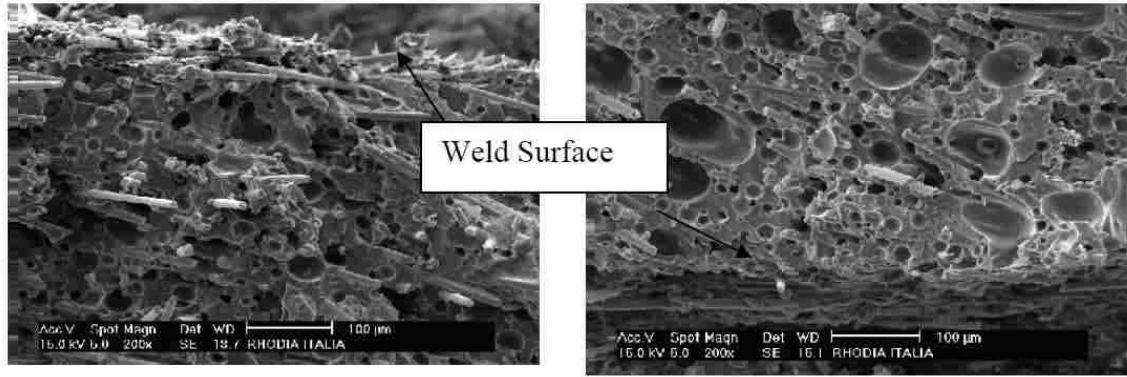
Figure 2.38 Tensile test results. (1) HAZ welded at 0.6 MPa and 1 mm. (2) HAZ welded at 0.6 MPa and 1.78 mm. (3) HAZ welded at 5 MPa and 1 mm. (4) HAZ welded at 5 MPa and 1.78 mm. (5) Bulk [61].

Two conditions which are important for obtaining good joint strength are suggested by Kamal et al.: (a) retention of the largest fraction of the original fibres in the joint and (b) achieving a high level of orientation of the retained fibres in the tensile direction. Under high welding pressure, the squeeze flow caused more flash and loss of both polymer and fibres. Thus, more fibres are retained at low welding pressure, which could result in higher tensile strength. However, in their study, the vibration welding process altered the distribution of fibre orientation, thus the fibre orientation in the tensile direction was diminished dramatically. This explains why the weld joint is weaker than the bulk section.

In addition, the lower weld strength of the fibre-reinforced samples compared with the unreinforced ones can be attributed to the diminished fibre orientation in the tensile direction in all the vibration welded joints. This may perhaps be improved by changing the configurations of fibre orientation in the two mouldings or the processing conditions, so that the orientation of the fibres in the weld becomes more favourable [61].

2.7.5 VIBRATION WELDING OF GLASS FIBRE REINFORCED PLASTIC MOULDED BY MUCCELL® PROCESS

It has been reported by Levi Kishbaugh et al. [63] that the friction welding of MuCell® parts is problematic since these welds tend to create joints that are significantly weaker than their solid counterparts. In vibration welding, it is difficult to keep the cell structure from the weld area as these areas, due to the nature of the process, are flat and relatively wide (Figure 2.39).



PA 6 Near Weld

PA 6.6 Near Weld

Figure 2.39 Cell structure close the weld area [63].

The results from the weld study show that even using optimized welding conditions, a 12% and 20% decrease in burst strength is still observed in MuCell® parts moulded using PA 6 and PA 66, respectively (Figure 2.40).

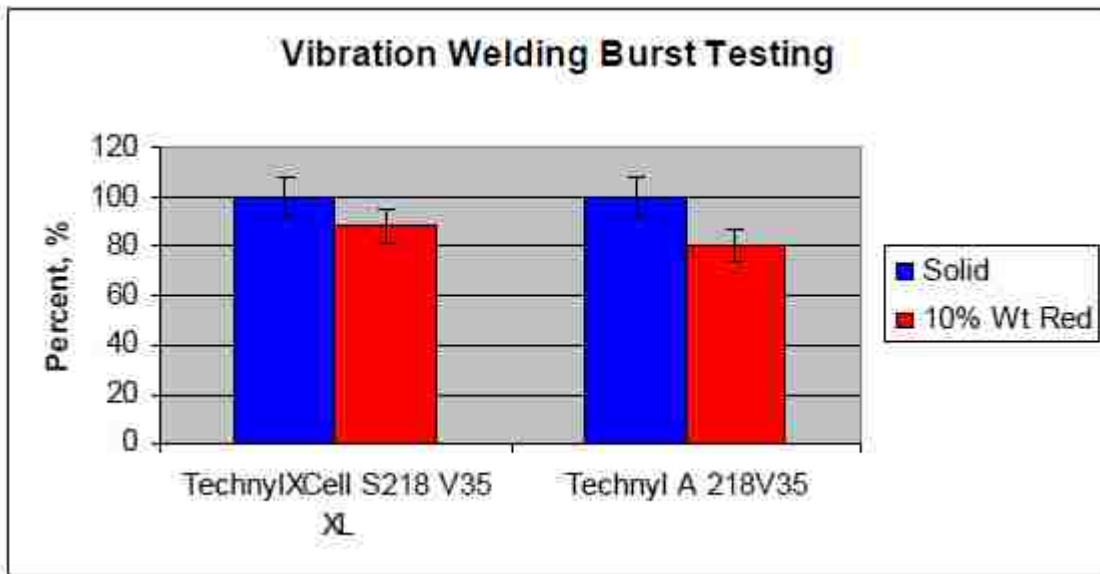


Figure 2.40 Burst test results for MuCell® samples moulded with PA6 (TechnylXCell S218 V35) and PA66 (Technyl A 218V35) [63].

This inability of manufacturers to achieve sufficient strength in the joints of the MuCell® friction welded sample has prevented the utilization of the MuCell® injection moulding procedure and its advantages. Thus, research into optimizing the weld strength for the welding of MuCell® part is epically needed.

CHAPTER 3 MATERIALS AND EXPERIMENTAL METHODS

3.1 OVERVIEW

In this chapter, the weld strength and fatigue properties of MuCell® moulded glass fibre-reinforced nylon 6/66 are evaluated. In the first phase of our study, the burst tests were carried out using BASF water-filled burst test facilities. Pressure cycle fatigue tests were conducted on each sample using a Thermotron testing machine (series 27484). The materials studied included parts moulded using the MuCell® process as well as their solid counterparts for reference. The material that was optimized in the mechanical test was selected for further investigation in the second phase.

To study the effect of the MuCell® process on mechanical properties, cell morphology was observed under optical microscopy and scanning electron microscopy (SEM). Cell size and cell density were studied and measured using image analysis software (ImageJ®). After the burst test, SEM was employed to characterize the fracture surface features. In addition, the degree of crystallinity and glass fibre content at the weld region were analyzed using differential scanning calorimetry (DSC) and thermal gravimetric analysis (TGA).

3.2 MATERIALS

Nylon 6 and Nylon 66 resins with 30-50 wt. % glass fibre content were injection moulded using nitrogen as supercritical gas with weight reductions (WR) of 7% and 10% in form of hemisphere shells with a diameter of 190.5 mm using a Krauss Maffei CX 500 moulding machine. The shells were moulded in two forms, having either 4 or 6 mm flattened beads, which form the weld region. Detailed information for the tested materials

is illustrated in Table 3.1. And the moulding conditions are expressed in Table 3.2 and Table 3.3 .

Table 3.1 Descriptions of the tested materials

Materials	Description	Weight reduction
Ultramid® B3WG7 BK564	35wt.% glass fiber reinforced, pigmented black, injection molding PA6 grade.	0%,4%,7%, 10%
Ultramid® B3WG6- GPX BK23238	30wt.% glass fiber reinforced, black, heat stabilized injection molding PA6 grade for primary use in welded air intake manifolds.	0%,4%,7%,10%
Ultramid® A3WG10 BK 564	50wt.% glass fiber reinforced,PA66 grade	0%,4%,7%,10%
MAHLE-72141328	50/50 blend, 30wt.% glass fiber reinforced PA6 post-consumer/post industrial	0%, 4%,7%,10%

Table 3.2 Moulding conditions of PA6 grades

Moulding conditions of PA6 grades				
	Solid	MuCell® 4% WR	MuCell® 7% WR	MuCell® 10% WR
Machine Parameters				
Shot size	3.8	1.88	1.8	1.73
Trans Pressure	730	9775	9772	9772
Injection Time	2.11	1.15	1.1	1.05
Hold Profile				
Time	12	0.5	0.5	0.5
Part Information				
% SCF	0	0.2	0.2	0.2
Mold Temperature				
Stationary	180	180	180	180
Moving	180	180	180	180

Table 3.3 Moulding conditions of PA66 grades

Moulding conditions of PA66 grade				
	Solid	MuCell® 4% WR	MuCell® 7% WR	MuCell® 10% WR
Machine Parameters				
Shot size	3.8	1.87	1.78	1.67
Trans Pressure	580	6379	7073	6696
Injection Time	1.77	1.14	1.08	1.01
Hold Profile				
Time	12	0.5	0.5	0.5
Part Information				
% SCF	0	0.2	0.2	0.2
Mold Temperature				
Stationary	200	200	200	200
Moving	200	200	200	200

3.3 VIBRATION WELDING

The moulded hemisphere shells were welded using a Telsonic 615e vibration welder (Figure 3.1) at a frequency of 222.2 Hz, amplitude of 1.78 mm and a meltdown distance of 1.5 mm (Figure 3.2). The moulding and welding were processed in BASF Corporation, Michigan, USA.



Figure 3.1 Vibration welder

In order to have a better representation of the average weld of the entire part and reveal possible systematic local differences of the weld areas due to the unidirectional welding process, before and after welding, three sections on the samples were selected to be investigated (Figure 3.3), and labeled 12, 1.5 and 3 locations. The 12 location is oriented with the cross-section perpendicular to the weld direction, while the cross-section of the 3 location is parallel to the weld direction.

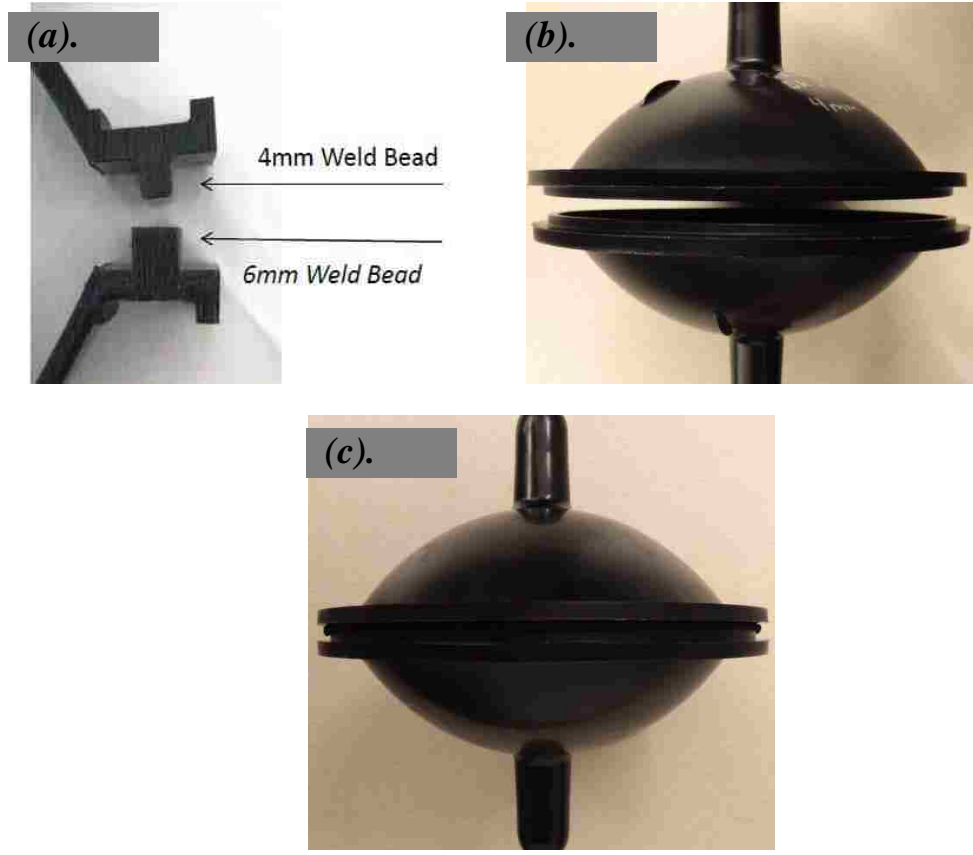


Figure 3.2 (a). cross-section of the 4mm and 6mm weld bead. (b). un-welded shells (c). welded shells. 4 mm and 6mm weld bead were welded together

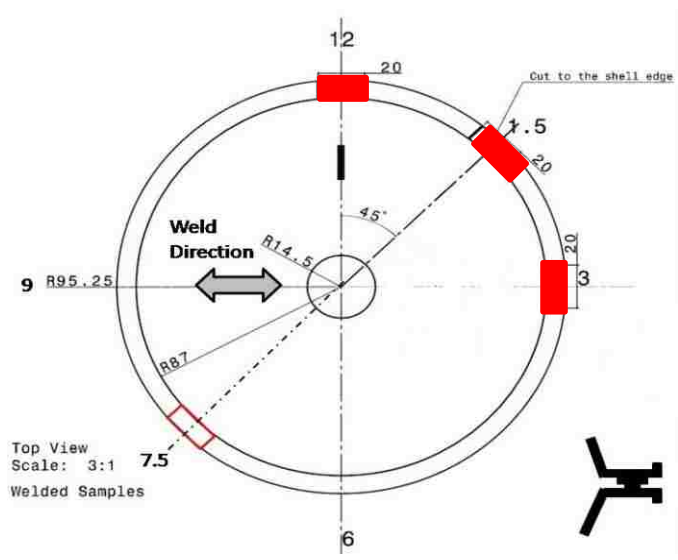


Figure 3.3 Selection of the samples

3.4 METALLOGRAPHY SAMPLE PREPARATION FOR CROSS-SECTIONAL VIEW

The samples were cut (refer to Figure 3.3) using a diamond saw and mounted using fast curing cold mounting material with the weld region normal to the viewing surface, as shown in Figure 3.4. The surface of the mounted samples was ground using SiC grinding papers in succession: P180, P400, P600, P1200 and P2400. Each sample was washed using a laboratory glassware washing solution between each step. After the grinding, the samples were polished using polishing cloths impregnated with 1 μm , 0.3 μm and 0.05 μm suspension aluminum oxide. The sample surface was then air-dried to avoid any scratches or residue on the surface.

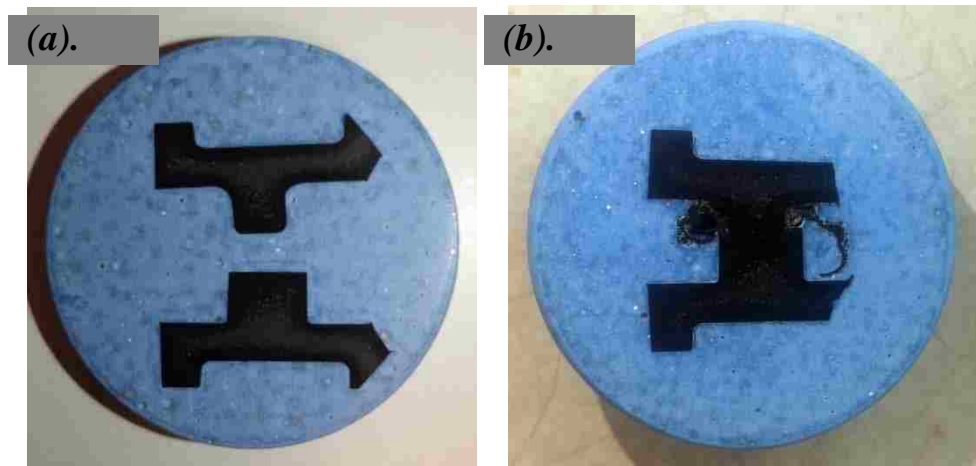


Figure 3.4 Cross-sectional view of (a) un-welded and (b) welded 4 mm and 6 mm beads samples prepared for microscopy investigation.

3.5 MECHANICAL PROPERTIES TEST

3.5.1 PRESSURE CYCLE FATIGUE TEST

To determine the fatigue life of welded sample under a specific pressure cycle, a pressure cycle fatigue test was conducted on each sample using a Thermotron testing

machine (Series 27484) which is shown on Figure 3.5. The pressure cycle fatigue test machine provided pressure and thermal cycling through the span of testing. One pressure cycle consisted of a pressure increase from zero to two atmospheres, followed by a decrease back to zero, all of which occurred over a span of four seconds period (Figure 3.6). While undergoing a pressure cycle each sample was also progressing through a thermal cycle ranging from 120 to -40 °C over the course of five and a half hours. This cycle is shown in detail in Figure 3.7. The test cycle stopped for each sample once they broke, began to leak or reach 200000 cycles.



Figure 3.5 Pressure cycle fatigue testing machine and test set-up

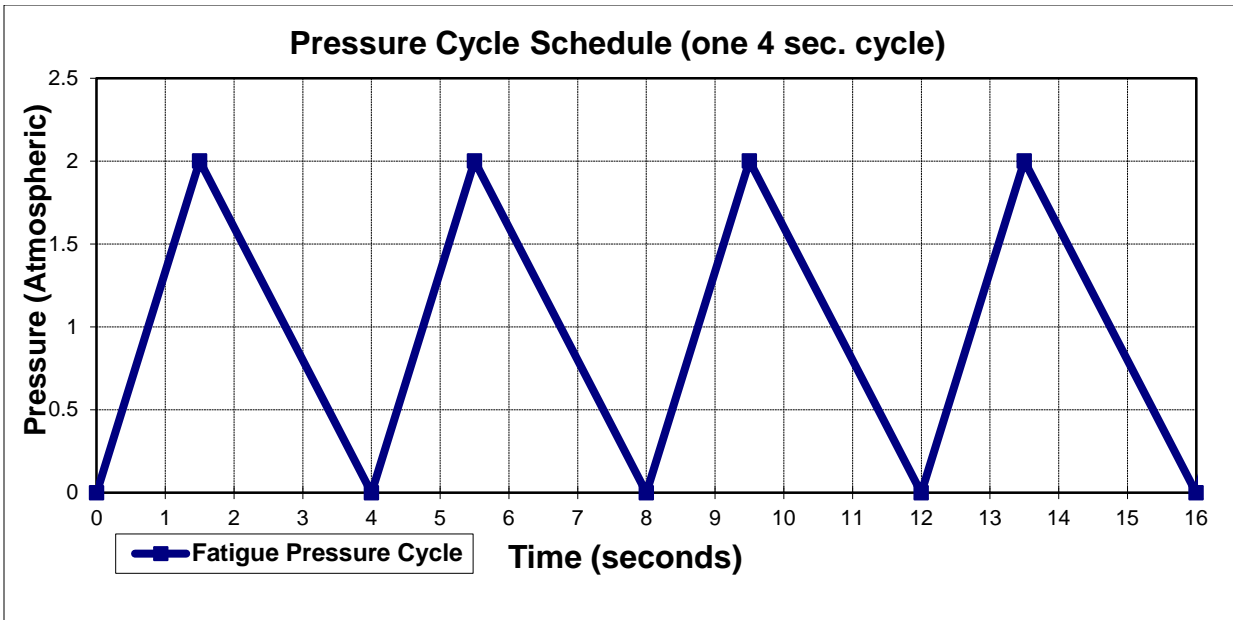


Figure 3.6 Pressure cycle during pressure cycle fatigue test

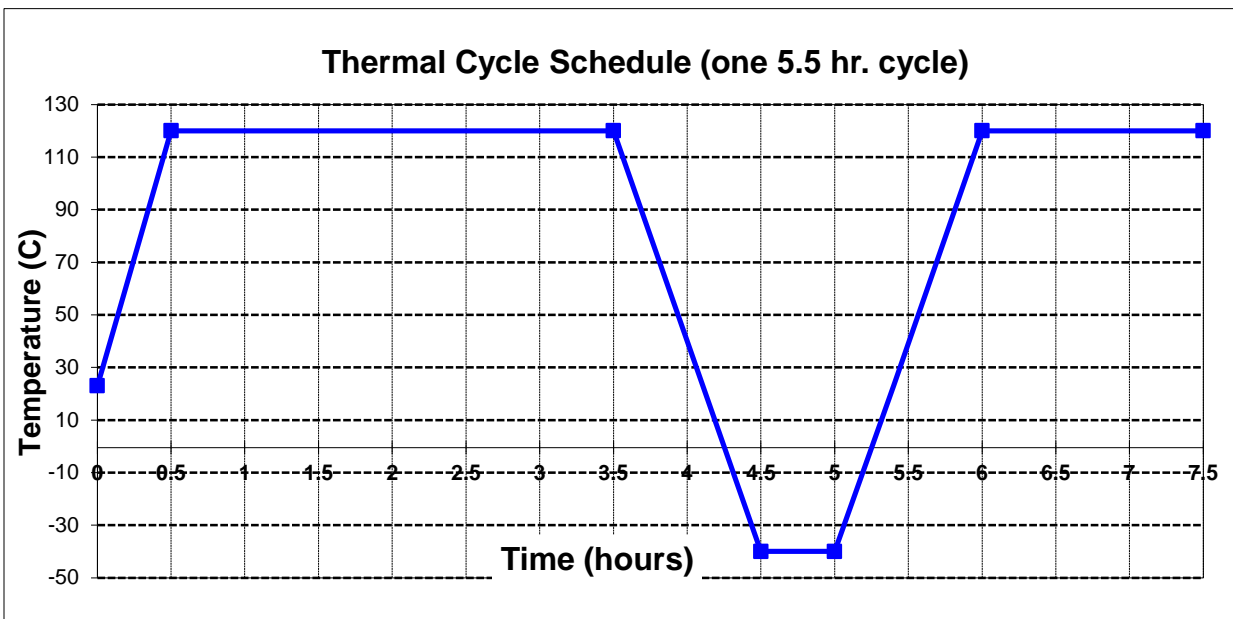


Figure 3.7 Thermal cycling during pressure cycle fatigue test

After testing, the samples were individually bagged, in order to preserve the fracture surface and placed in aluminum-lined moisture-resistant bags along with a desiccant bag to prevent moisture absorption.

3.5.2 BURST TEST

The samples underwent a water-filled burst test after welding process. The welded shells were laid in a water-filled burst tank while water was injected into the parts. The test stopped when the samples broke or when the part began to leak. This test is useful for measuring the ability of welded parts to withstand rapid internal pressurization by yielding an ultimate failure pressure throughout the process. The burst pressure peak value recorded is helpful in determining if the weight reductions achieved by MuCell® have negative effects on weld strength. The test set-up carried out at BASF for burst testing is shown in Figure 3.8.

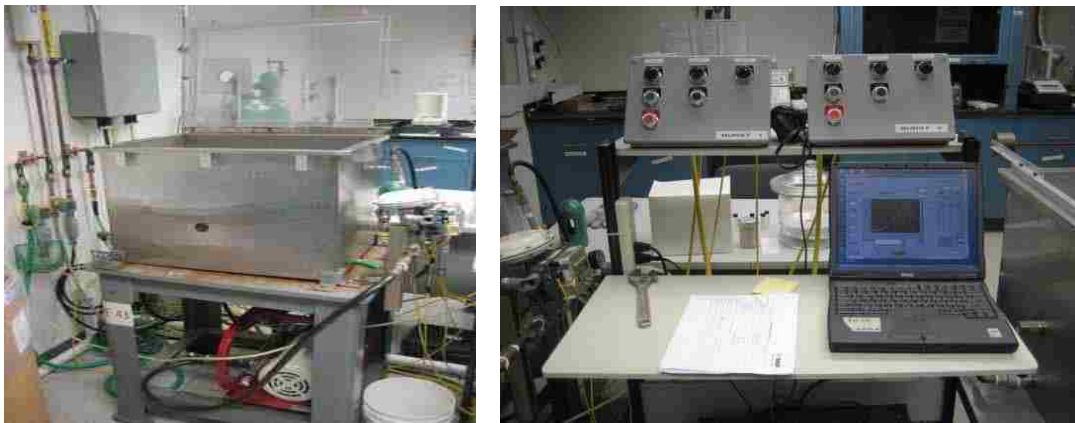


Figure 3.8 BASF burst test set-up

3.6 MICROSTRUCTURE INVESTIGATION

3.6.1 OPTICAL MICROSCOPY ANALYSIS

An optical microscope and image analyzer (Image J®) were used to analyze the cross-sectional views of the welded and un-welded MuCell® samples in order to determine the microstructural features, such as cell morphology and none-cell region thickness.

In order to have better knowledge of the cell size and parentage of the area occupied by the cells, images were taken from the center section of the cell region, which was defined as the section of the sample showing the most uniform cells (Figure 3.9).

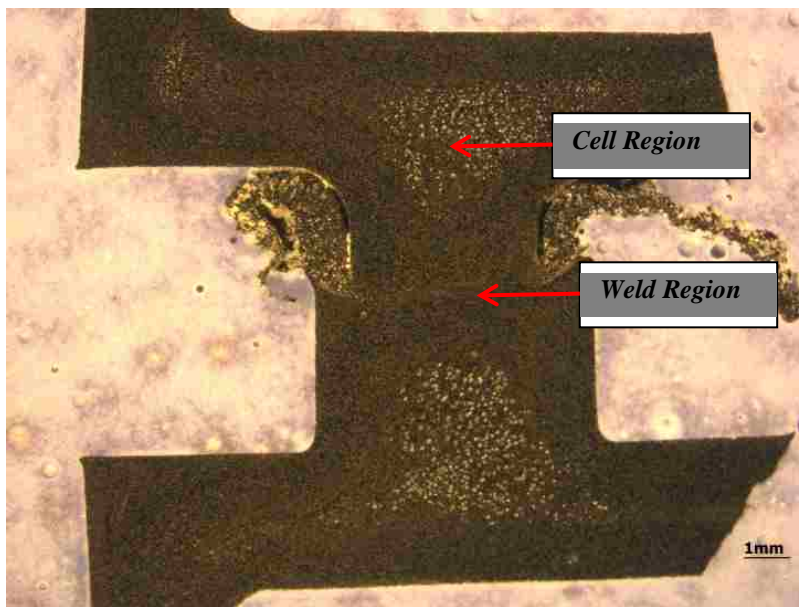


Figure 3.9 Sections to be observed using optical microscopy

The none-cell region thickness, in this study, refers to the distance from the outer layer to the region where the cells appear and is indicated in Figure 3.10. The region thicknesses were measured at three positions on the samples, close to the welding surfaces of both the 4 and 6 mm beads for the un-welded samples.

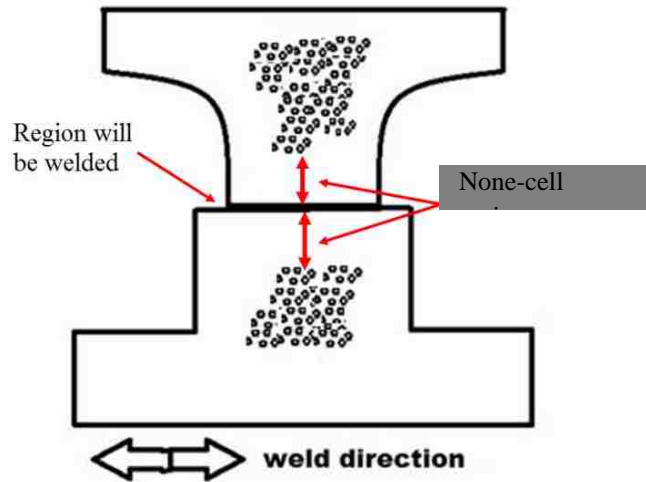


Figure 3.10 Measurement of none-cell region. It refers to the distance from the outer layer to the region where the cells appear.

3.6.2 SCANNING ELECTRON MICROSCOPY ANALYSIS

In order to determine the failure mechanism and why the MuCell® process lowers the strength of a weld joint, the fracture surfaces of several samples that had undergone a burst test were observed using scanning electron microscopy (Figure 3.11). When observing the failed part, an obvious whitened section was noticed; during the test that section was determined to be a stress mark where failure started during the test. As shown in Figure 3.12, the samples were selected from the stress mark.



Figure 3.11 Scanning electron microscopy employed in research objective from Great Lakes Institute for Environmental Research at University of Windsor



Figure 3.12 Fractured sample underwent a burst test

Besides the fracture surface, the weld region was also investigated by SEM. In order to avoid the influence of polishing on the microstructural observation, the welded sample was cryogenic fractured in liquid nitrogen with the cross-section of the weld region normal to the viewing surface and then analyzed under the SEM.

3.7 CRYSTALLINITY AND GLASS FIBRE CONTENT ANALYSIS

3.7.1 DIFFERENTIAL SCANNING CALORIMETER ANALYSIS

Crystallinity studies were performed on a Mettler Toledo DSC 822e. (Figure 3.13) The DSC samples were selected from weld region and cell region. The samples were first heated from -50°C to 250°C at a rate of $10^{\circ}\text{C}/\text{min}$ to probe their melting as processed materials. In a second experiment, the samples were first slowly cooled from 250°C to 150°C at a cooling rate of $1^{\circ}\text{C}/\text{min}$ to obtain the maximum degree of crystallinity, and then the samples were heated again to 250°C at a rate of $10^{\circ}\text{C}/\text{min}$. All the samples were run in aluminum crucibles.



Figure 3.13 DSC testing fixture

3.7.2 THERMOGRAVIMETRIC ANALYSIS

Thermogravimetric (TGA) experiments were also employed in order to have a better knowledge of the glass fibre content at weld region. The TGA was performed using TGA/DTA-MS 851e/SF (Figure 3.14) with a nitrogen flow. Samples (around 10 mg) selected from weld regions on welded samples with different weight reductions were heated in 150 ul alumina pans from 30 K up to 1000K at heating rates of 10k/min.

For comparing the MuCell® samples with their solid counterpart, all preparations, measurements and analyses listed above were also carried out on the solid sample.



Figure 3.14 TGA testing fixture

CHAPTER 4 EXPERIMENTAL RESULTS

4.1 OVERVIEW

This chapter is divided into two major sections: the first section features a discussion of the characterization of the weld strengths of the MuCell® moulded PA6 and PA66, including the pressure cycle fatigue test and water-filled burst test results. The fatigue life and burst strength for samples with different weight reductions are compared. In the second section, detailed studies of the material which provided the optimized weld joint strength are presented. Cell morphologies, including cell size and area occupied by cells along with the non-cell region thickness, were examined under optical microscopy. The fractured surface after the burst test and the cross-section of the weld region were observed using SEM. At the same time, the degree of crystallinity and glass fibre content at the weld region were determined and are discussed in this section.

To compare the MuCell® samples with their solid counterparts, most of the tests and analyses listed above were also carried out on the solid samples.

4.2 WELD STRENGTH TEST RESULTS

4.2.1 PRESSURE CYCLE FATIGUE TEST RESULTS

Figure 4.1 depicts the pressure cycle fatigue test results of different samples. It can be observed that, compared with the MuCell® samples, the solid samples exhibit significantly longer fatigue life. When comparing the fatigue lives between different materials, B3WG6-GPX shows the best performance—it did not fail even after reaching 200,000 cycles. The B3WG7 and A3WG10 samples are observed to be sensitive to the MuCell® process in that the MuCell® samples have a much shorter fatigue life compared

with the solid samples. A positive correlation between the test results and weight reduction is found on the MAHLE MuCell® samples in this study. The fatigue lives of the MAHLE samples increase when the weight reduction is increased from 4% to 10%.

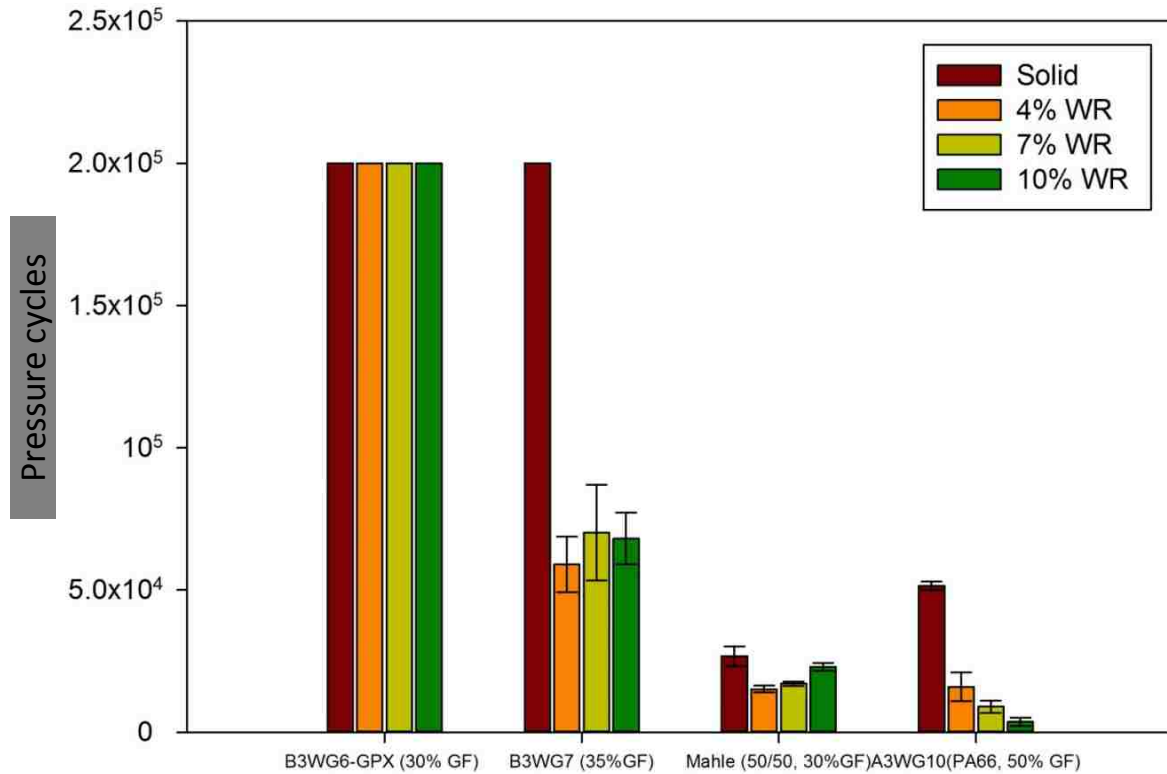


Figure 4.1 Pressure cycle fatigue test results. Comparing with MuCell® samples, the solid samples exhibit significantly longer fatigue life. Additionally, B3WG6-GPX material exhibited the longest fatigue life among all the matrices.

4.2.2 BURST TEST RESULTS

As is shown in Figure 4.2, the results collected from the burst test are similar to those of the pressure cycle fatigue test. The solid samples, as expected, show the highest weld strength in the burst test, and again the B3WG6-GPX samples are observed to have the best performance. However, variations in test results between the samples moulded

with different matrices are not as significant as in the pressure cycle fatigue test. It should be noted that after both tests, all the test samples were found to fail at the weld joint, indicating that those two tests are a good representation of the weld strength.

Combing the results of the pressure cycle fatigue test and burst test, the B3WG6-GPX samples are observed to have the maximum weld strength. Therefore, this material is selected to be further investigated for the effect of MuCell® process on weld performance.

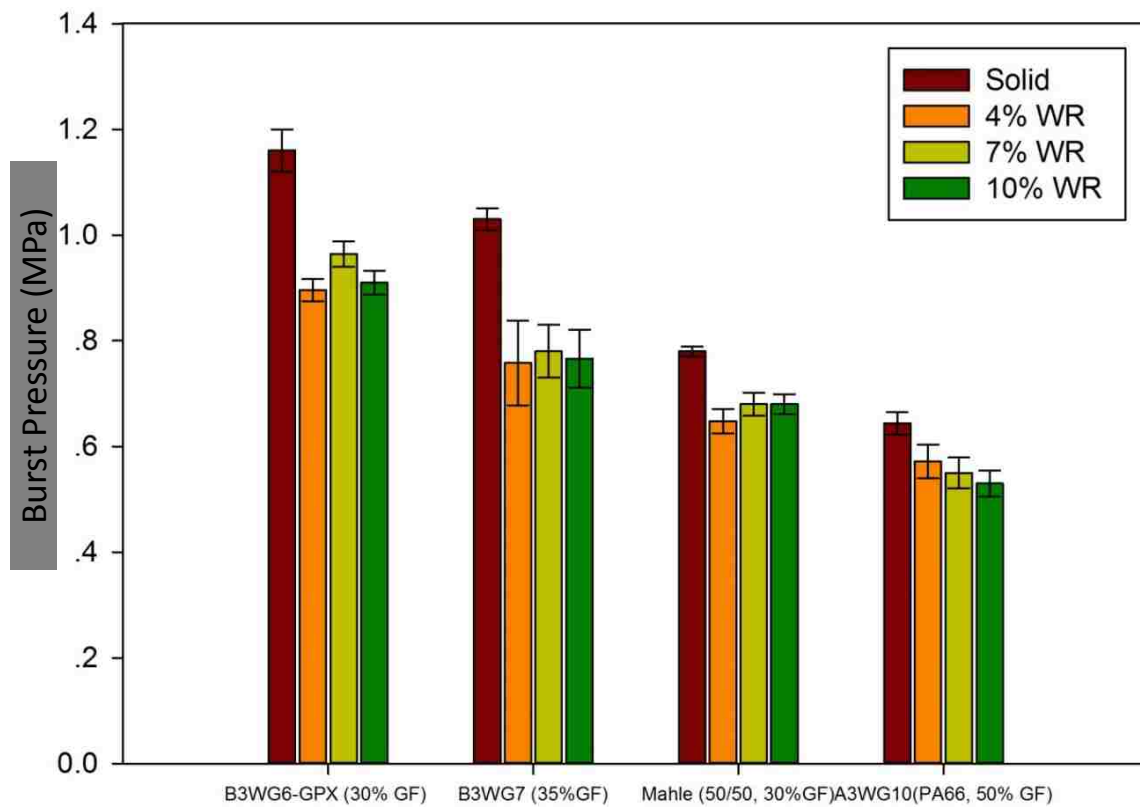
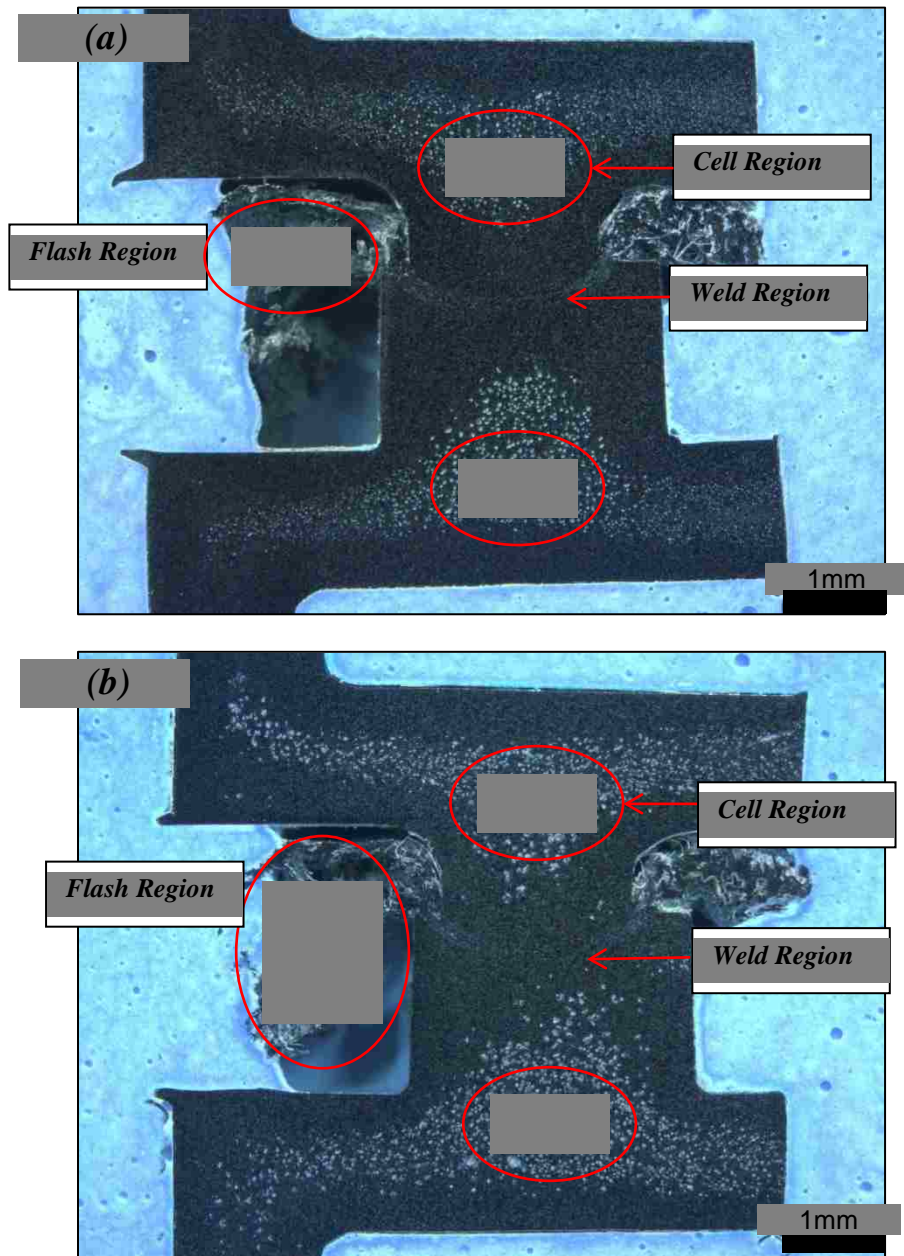


Figure 4.2 Burst Test Results. The solid samples show the highest weld strength in the burst test, and the B3WG6-GPX samples are observed to have the best performance comparing with other matrices.

4.3 OPTICAL MICROSCOPY INVESTIGATION

The typical structures of the welded MuCell® samples are illustrated in Figure 4.3. As can be seen from the images, several regions can be observed on the weld samples; including weld region, flash region, and cell region on both 4 mm and 6 mm weld beads.



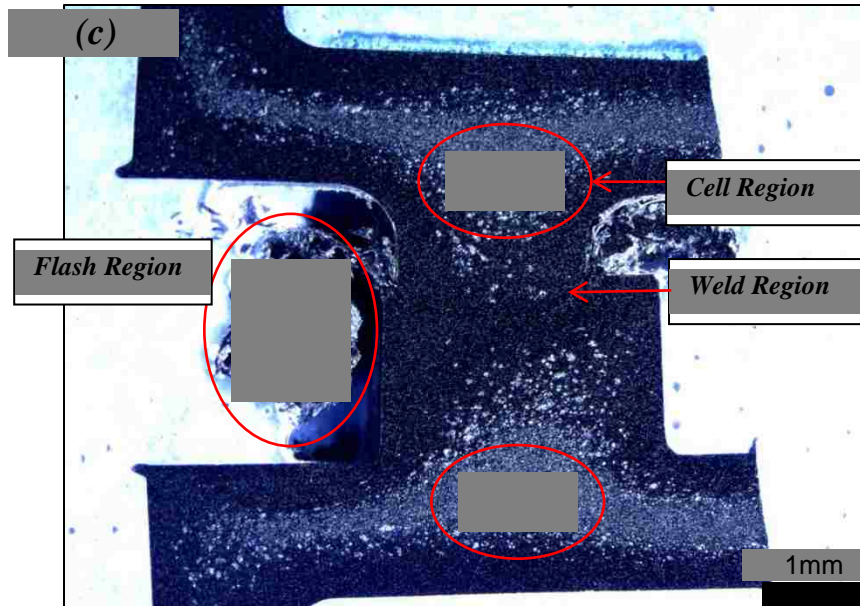


Figure 4.3 Typical structure of welded a. B3WG6-GPX 4% WR sample b. B3WG6-GPX 7% WR sample c. B3WG6-GPX 10% WR sample. The weld region, the flash and the cell region on the 4 mm and 6 mm parts can be observed on all the samples.

4.3.1 CELL MORPHOLOGY: CELL SIZE AND AREA OCCUPIED BY CELLS

For the B3WG6-GPX samples, the change in cell size and the area occupied by the cells is mostly achieved by varying the weight reduction of the moulded samples. Figure 4.4 (a) shows the average radius of the cells on the different samples. The largest cells can be observed on the 7% WR samples, which also have a relatively smaller standard deviation, while the 10% WR samples show the smallest cells as well as the lowest standard deviation.

The results of the cell area analysis of the MuCell® samples are shown in Figure 4.4 (b). It should be noted that the percentage of the area occupied by cells is analyzed from the cell region, not the calculation for the size of the cell region. The cells region of

sample produced with the weight reduction of 7% tend to contain more area occupied by cells up to 15.63% (3.3% and 5.1% area more than 4% WR and 10% WR samples).

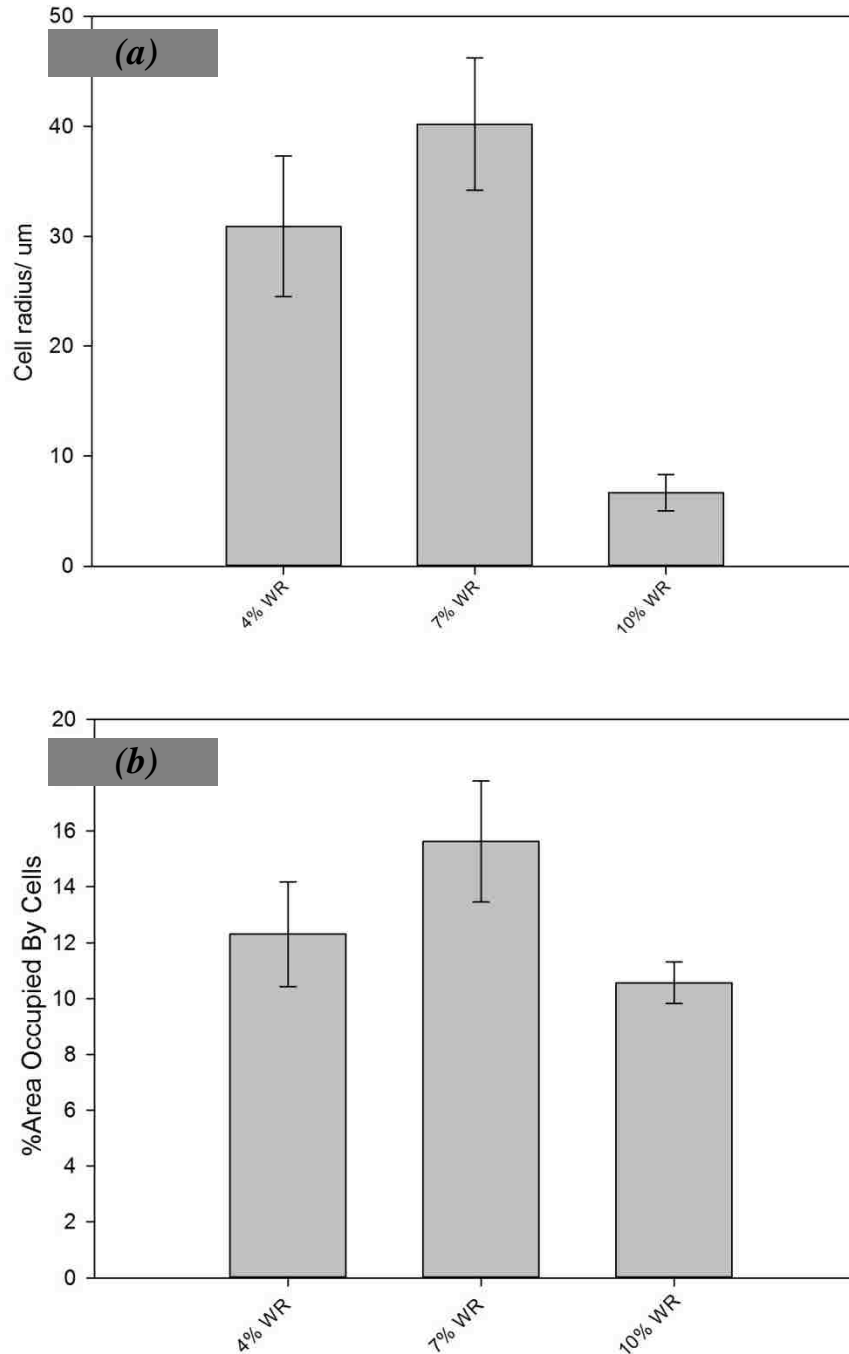
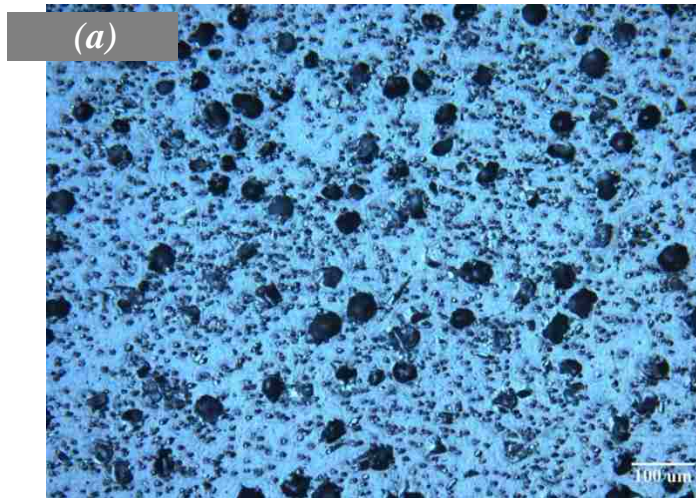


Figure 4.4 (a) Average cell radius with standard deviation. The Largest and smallest cell radius can be observed on the 7% WR and 10% WR samples respectively. (b) Average

cell area with standard deviation. Comparing with 4% WR and 10% WR samples, 7% WR samples tend to show larger cell size and area occupied by cells. Error bar is standard deviation.

Combining the observations for both Figure 4.4 (a) and (b), a brief conclusion can be firstly made that the 7% WR samples tend to exhibit the largest cell size along with a relatively larger area occupied by cells at the cell region, whereas much smaller cells and the smallest area occupied by cells can be found on the 10% WR samples.

Additionally, through the author's observation, a trend can also be observed that the cells become more uniformly sized and evenly distributed at the center of the cross-section as the weight reduction increases from 4% to 10% (Figure 4.5).



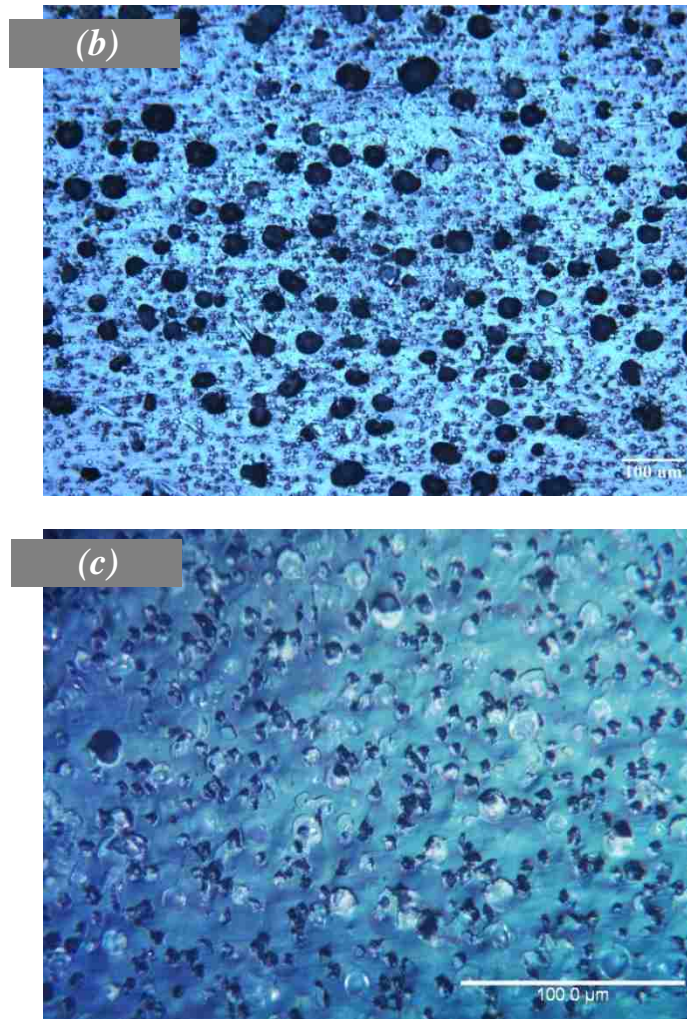


Figure 4.5 Optical microscopy images for the cells regions a.4% WR sample b. 7% WR sample c. 10% WR sample. more uniformly sized and evenly distributed at the center of the cross-section as the weight reduction increases from 4% to 10%.

4.3.2 NONE-CELL REGION THICKNESS

The variation of none-cell thickness close to the weld region with weight reduction varying from 4% to 10% is shown in Figure 4.6. The thickness of the none-cell layer is the highest at 4% WR but decreased with increasing weight reduction. This trend became more significant from 7% WR to 10% WR. More specifically, the 10% WR sample exhibited a 35% thinner none-cell layer than the 7% WR sample. This trend could be

attributed to a larger cell region resulting from the greater number of nucleation sites created by the additional nitrogen gas giving a higher weight reduction.

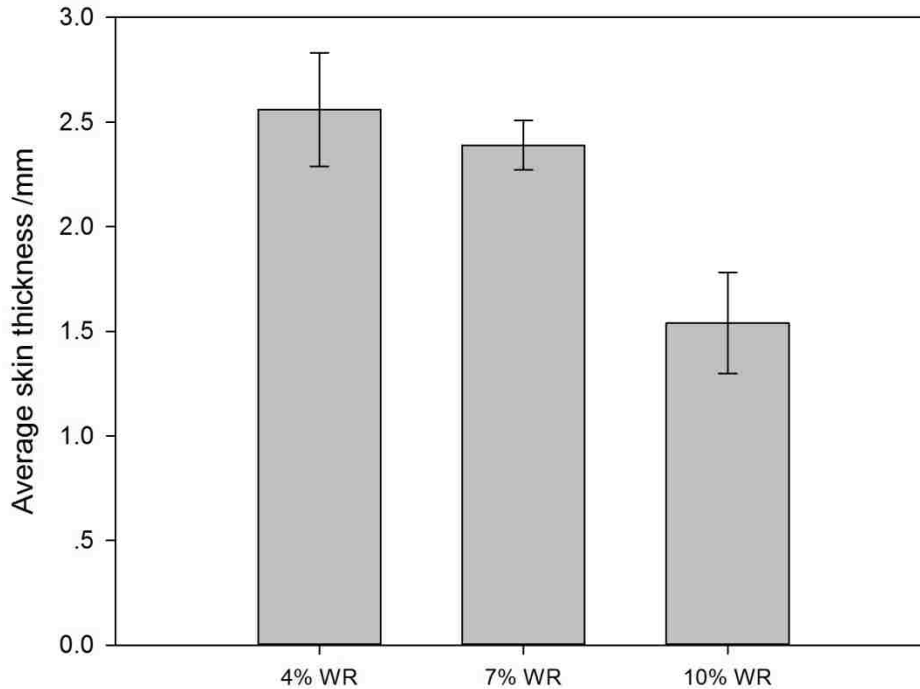


Figure 4.6 Average none-cell thickness with standard deviation. The thickness of none-cell layer was the highest at 4% WR and decreased with increasing weight reduction. Error bar is standard deviation.

4.4 CRYSTALLINTY AND GLASS FIBRE CONTENT

4.4.1 THERMOGRAVIMETRIC ANALYSIS

The thermal degradation behaviours of the weld region selected from different samples were investigated by TGA and are shown in Figure 4.7. All the samples degraded in one step and had similar thermal degradation behaviour. However, the 7% WR and solid samples showed significantly lower mass loss than the 4% and 10% WR samples. Besides, only glass fibres were observed when checking the residual in the pans.

Thus, the difference in TGA curve is mainly caused by the variation of glass fibre content in the samples. In another words, it is suggested from the data that the solid and 7% WR samples exhibit higher glass fibre content at the weld region than the other samples.

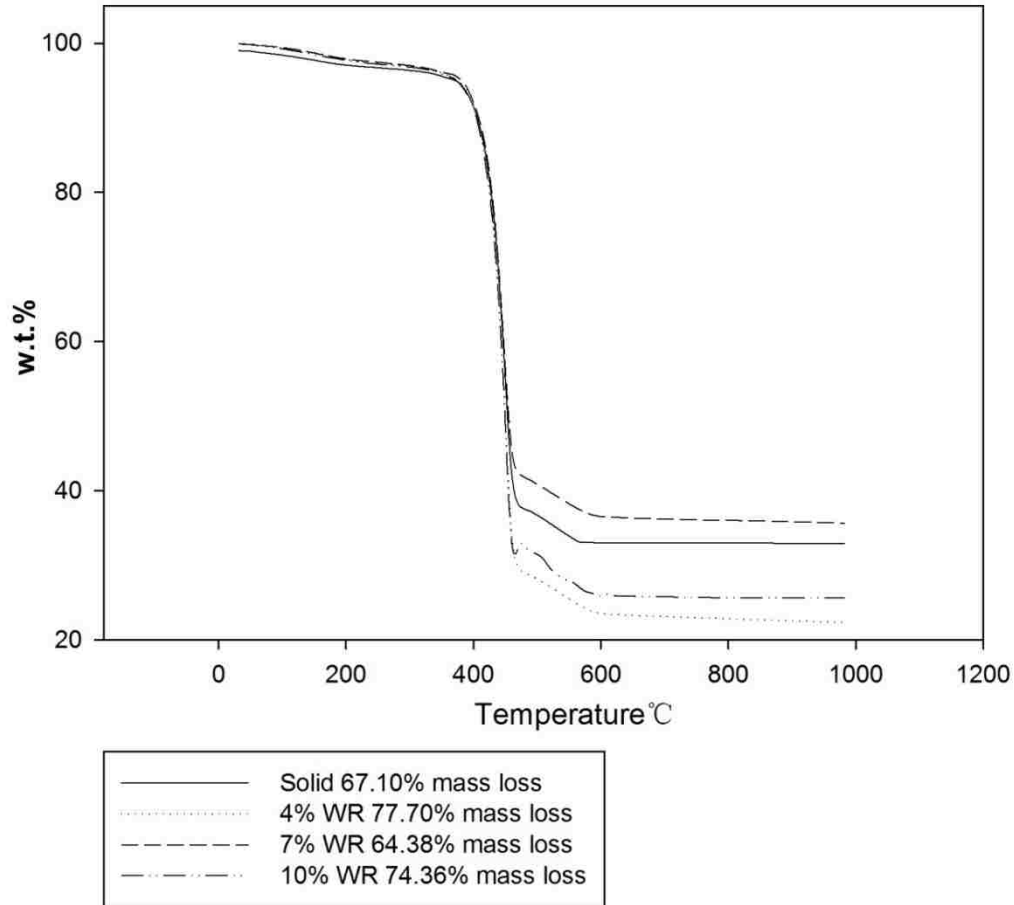


Figure 4.7 The variation of TGA test results at weld region with varying weight reductions. The 7% WR sample exhibits the highest glass fibre content at weld region (35.19%), and the solid sample shows 2.3% lower content. Whereas, the glass fibre content for 4% WR sample is just 22.3% which is the lowest among all samples tested.

4.4.2 DIFFERENTIAL SCANNING CALORIMETRY RESULTS

The tested curves for cell region and weld region are illustrated in Figure 4.8 and Figure 4.9, and all measured values are summarized in Figure 4.10. For all samples, the onset of melting is at approximately 150 °C and is followed by cold crystallization, which eventually converges with the main melting transition at about 200°C. Most melting enthalpies are between 35 and 50 Jg⁻¹ and are calculated by integration of the entire endothermic melting transition followed by subtraction of the enthalpy of the exothermic cold crystallization process.

As expected, in most cases the melting enthalpies after slow cooling at 1°C min⁻¹ are larger than those for the first heating of the “as moulded” samples. These differences in melting enthalpies are used to calculate their relative differences in degrees of crystallinity, which amounted to a 3–12% lower degree of crystallinity for the tested samples.

It also can be observed from Figure 4.10 that, for all samples, the obtained enthalpy was higher in the weld region than in the cell region. In addition, for samples selected from the cell region, the melting enthalpies decreased along with increasing weight reduction, whereas the enthalpies fluctuate more dramatically for the samples selected from the weld region. Higher values were achieved by the 4% WR and 10% WR samples, whereas the solid and 7% WR samples exhibited lower enthalpies.

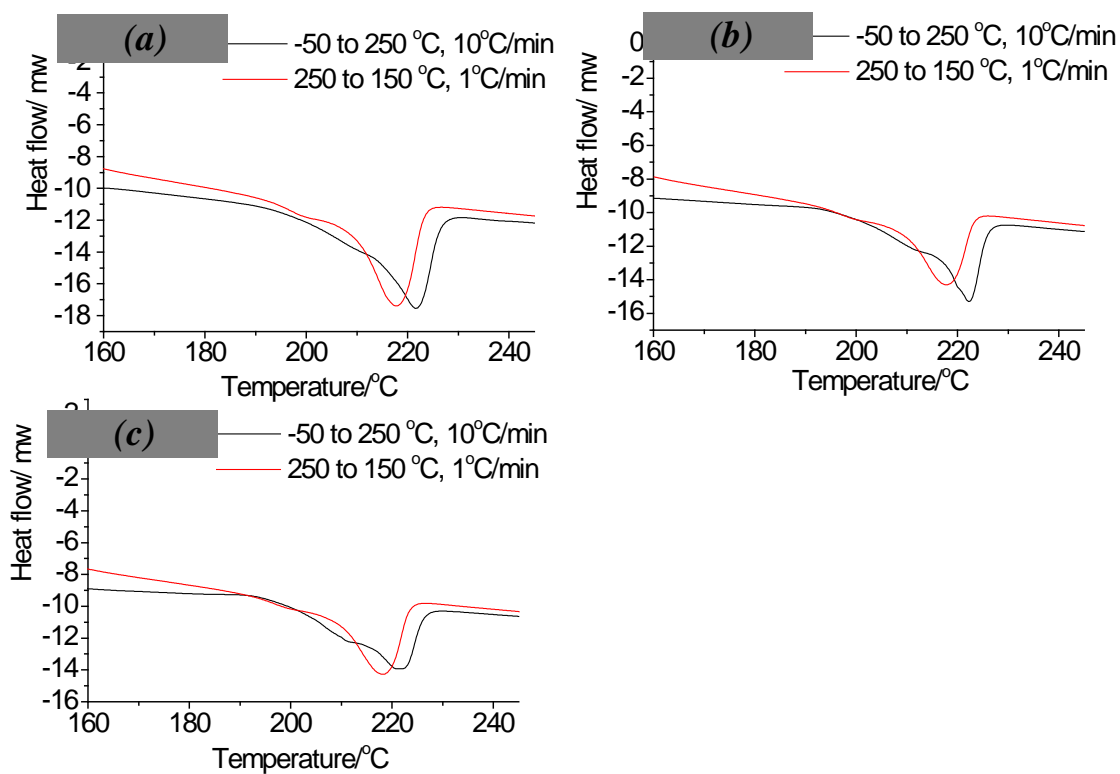


Figure 4.8 Results achieved by differential scanning calorimetry analyze for cell region. a. B3WG6-GPX 4% WR b. B3WG6-GPX 7% WR c. B3WG6-GPX 10% WR

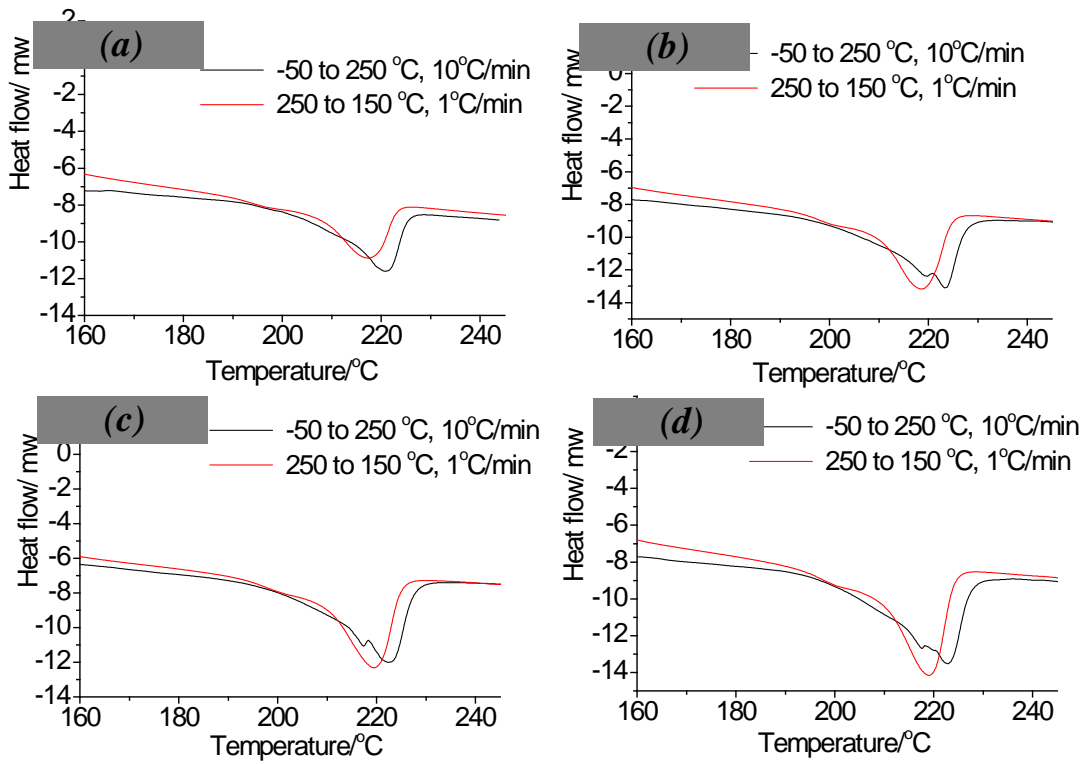


Figure 4.9 Results achieved by differential scanning calorimetry analyze for weld region.
 a. B3WG6-GPX solid b. B3WG6-GPX 4% WR c. B3WG6-GPX 7% WR d. B3WG6-GPX 10% WR

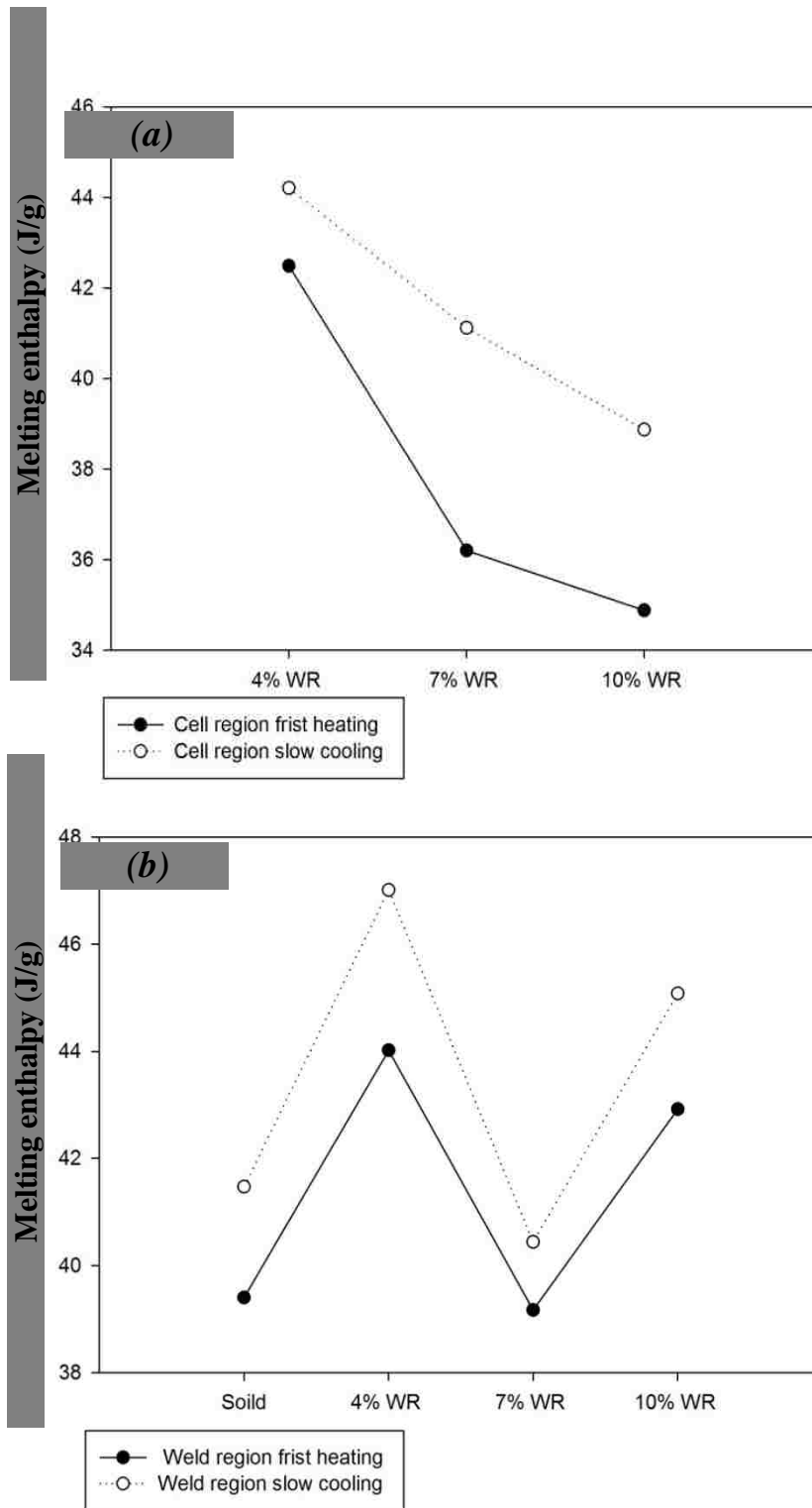


Figure 4.10 The variation of melting enthalpies with varying locations of samples. a. Cell region b. Weld region. The melting enthalpies after slow cooling at $1^{\circ}\text{C min}^{-1}$ tend to be larger than for the first heating of the “as moulded” samples. Besides, the obtained enthalpy was higher in the weld region than in the cell region.

4.5 SCANNING ELECTRON MICROSCOPY OBSERVATION

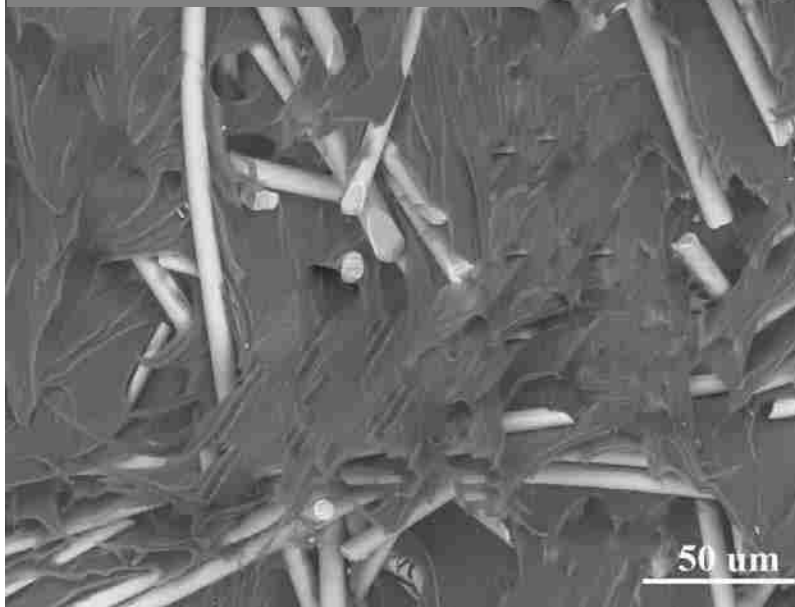
4.5.1 FRACTURE SURFACE INVESTIGATION

In order to determine the failure mechanism and why the MuCell® process lowers the strength of the weld joint, the fracture surfaces of the MuCell® samples that had undergone a burst test were observed using SEM.

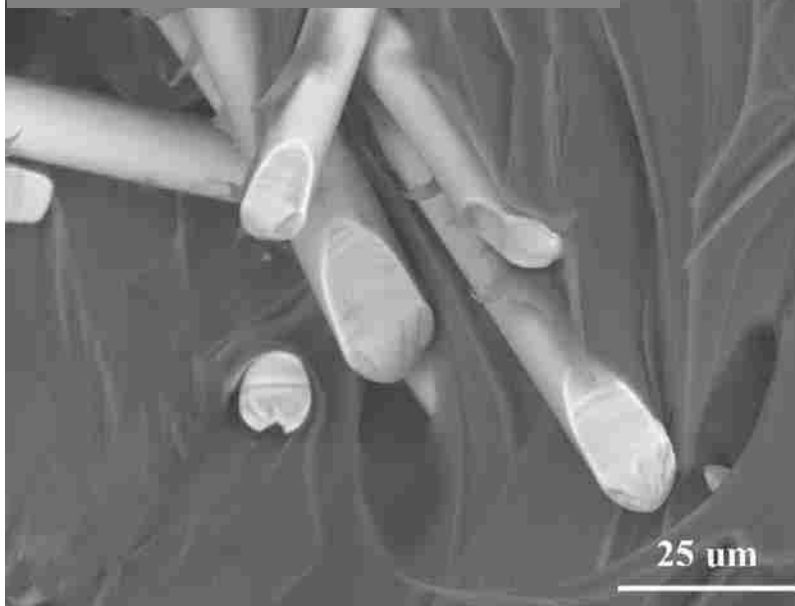
The investigation of the fracture surface was based on the burst test results for the B3WG6-GPX samples. Comparing the solid sample and the MuCell® samples, the solid sample has significantly higher weld strength than the MuCell® samples. Additionally, appearance differences were observed on the fracture surfaces between the two groups. As can be seen from Figure 4.11, compact cells are observed on the fracture for all MuCell® samples. The shape of the cells is near-spherical, and the distribution of cell sizes is relatively uniform (with a diameter of 5–9 µm).

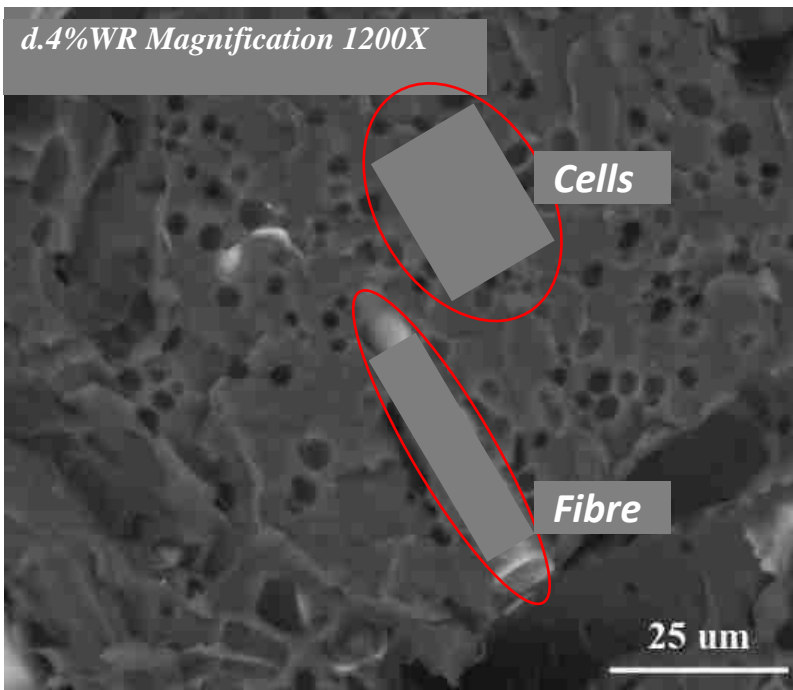
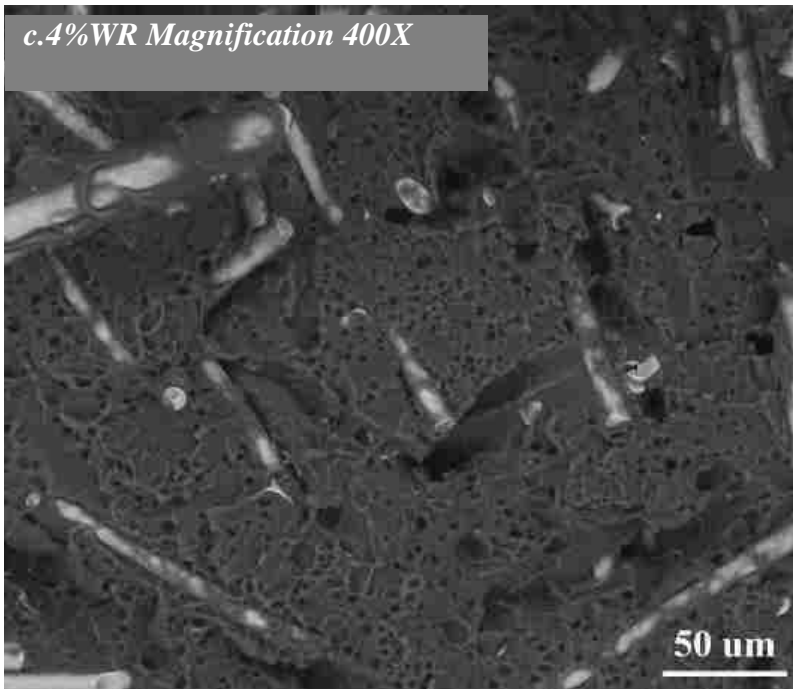
However, it can be seen that the fibres on the B3WG6-GPX samples are randomly aligned and are well bridged in the matrix. The high magnification images show that the surface is free of gaps; this result indicates that few fibres are pulled out of the matrix and therefore remain in place to contribute to a stronger weld joint.

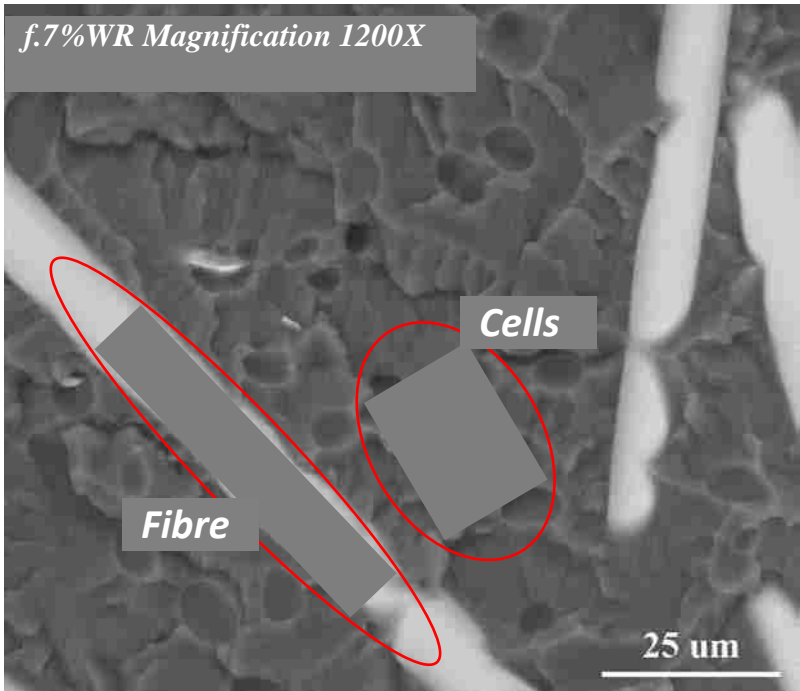
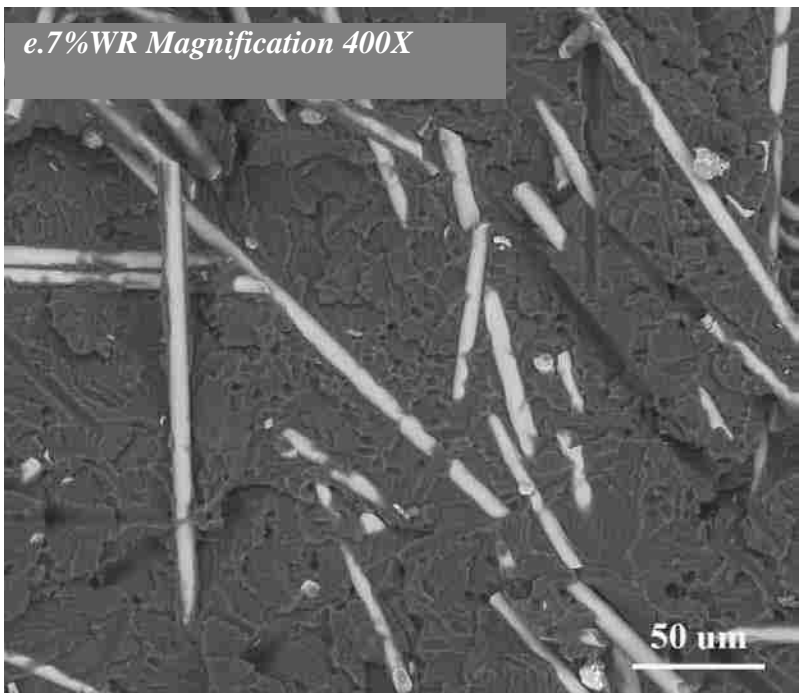
a. Solid sample Magnification 400X



b. Solid sample Magnification 1200X







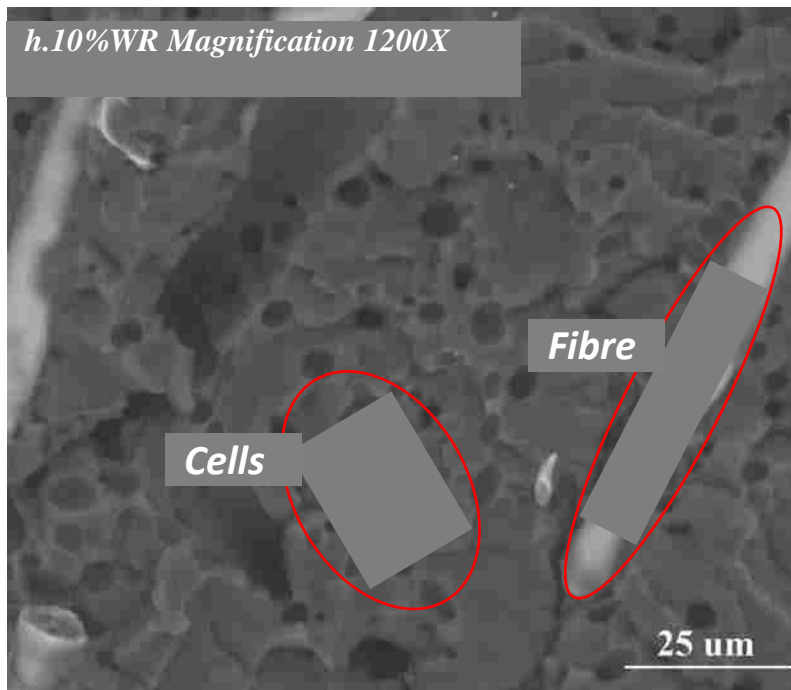
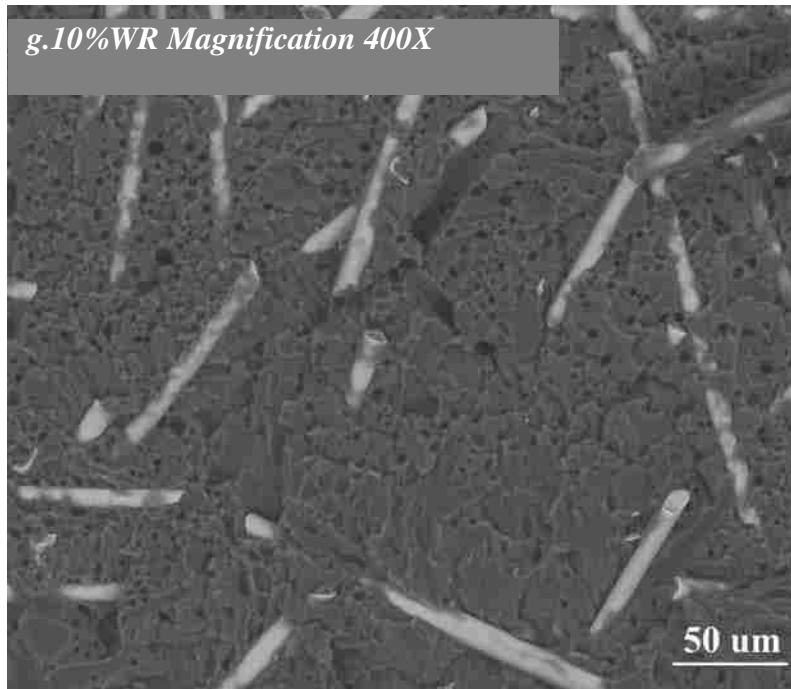


Figure 4.11 SEM morphologies of fracture surface for (a) solid sample with magnification of 400x. (b) solid sample with magnification of 1200x. (c) 4% WR sample with magnification of 400x. (d) 4% WR sample with magnification of 1200x. (e) 7% WR sample with magnification of 400x. (f) 7% WR sample with magnification of 1200x. (g)

10% WR sample with magnification of 400x. (h) 10% WR sample with magnification of 1200x.

4.5.2 WELD REGION INVESTIGATION

In all samples, failure originated in the weld joint during the burst and the pressure cycle fatigue tests. During the welding process, the contact surfaces of the two halves began to melt due to induced friction. By applying pressure, the material began to melt and flow laterally away from the weld seam, resulting in a potentially suitable condition for cell nucleation and leaving some oriented glass fibres behind. The cells foamed during welding would weaken the joining strength by replacing matrix material at the weld joint. Moreover, the lateral flow may cause the glass fibres to become aligned perpendicularly to the applied tensile force acting during the mechanical test, making them less effective in strengthening the weld joint. The weld regions were analyzed to observe whether those processes were occurring.

In order to avoid the side-effect from polishing and grinding, one group of the welded sample was cryogenic fractured in liquid nitrogen with the cross-section of weld region normal to the viewing surface and then observed under SEM.

The SEM images of the weld region show that the fibres are oriented parallel to the weld direction, which form a significant “weld line” at the weld region (Figure 4.12). In addition, compact but slightly distorted cells are observed at the weld region (Figure 4.13).

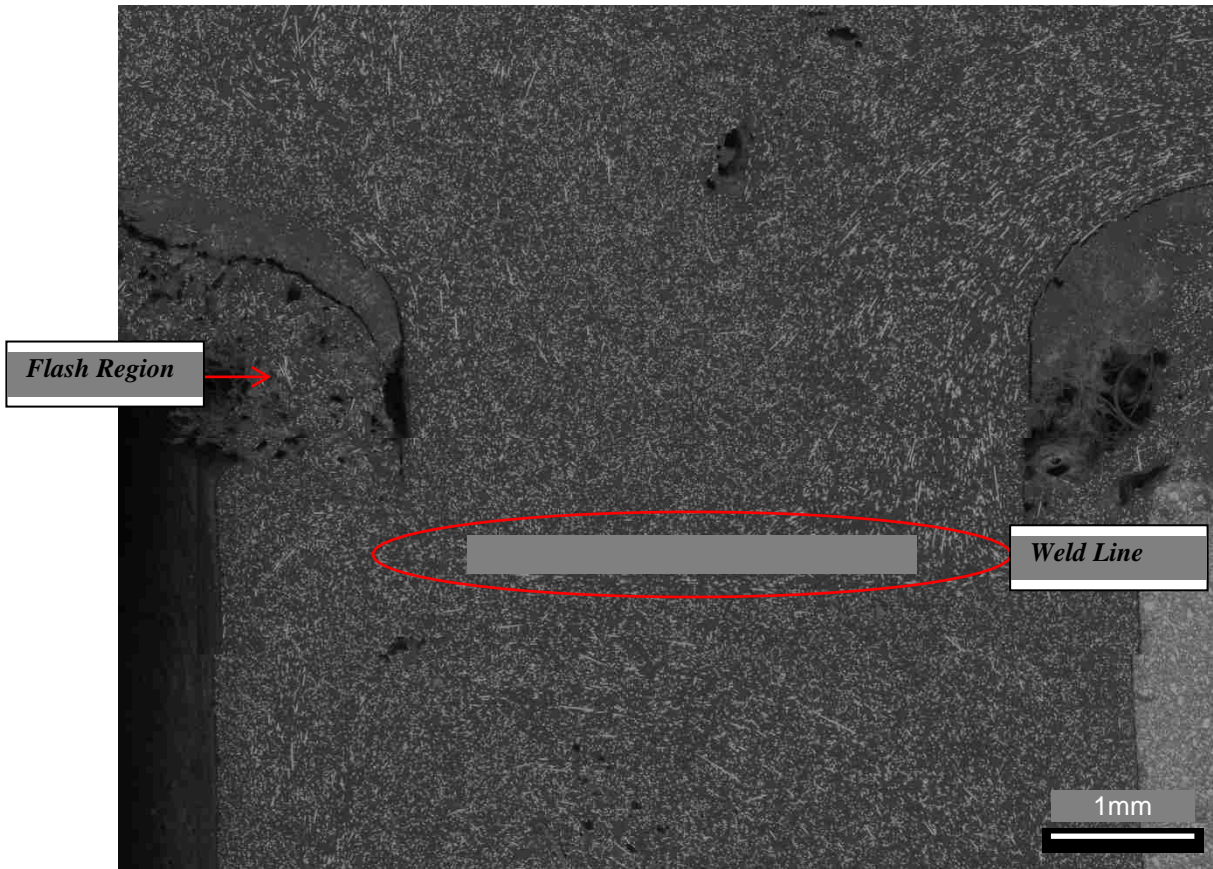
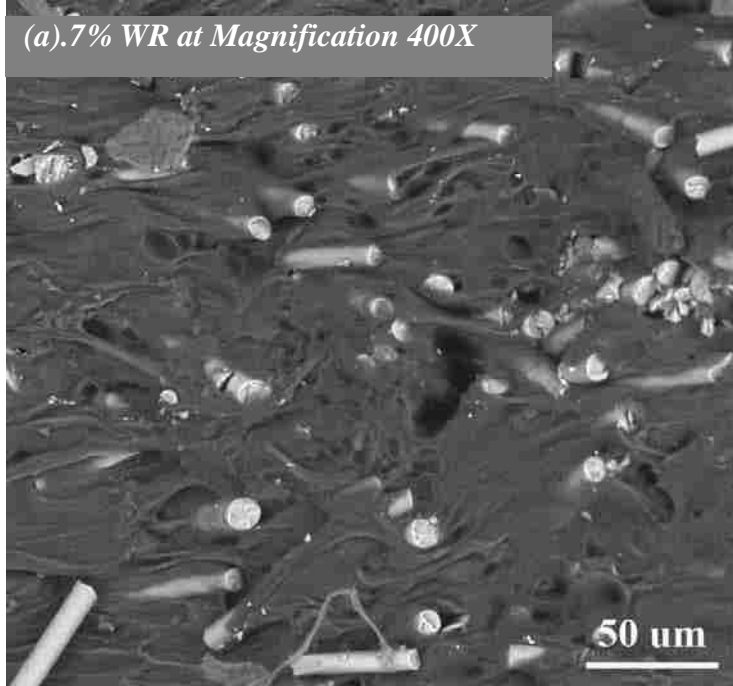
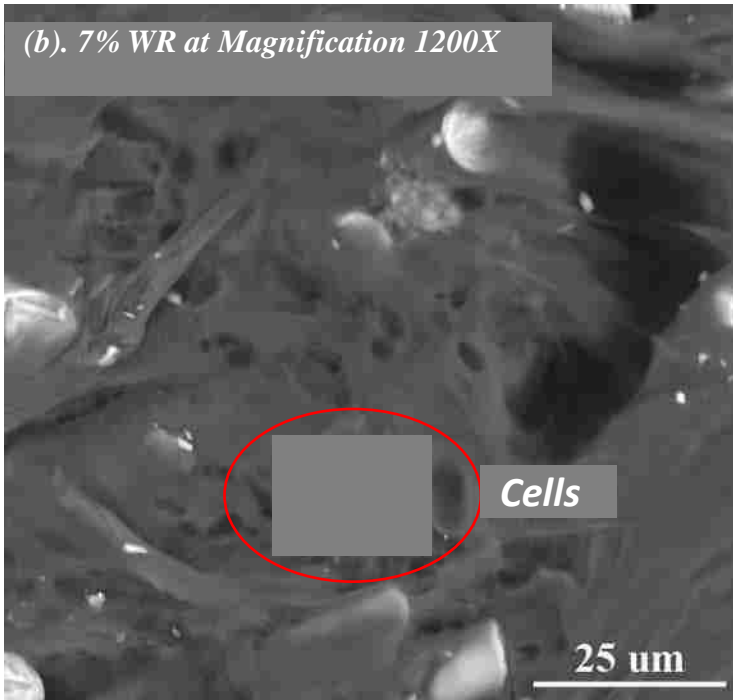


Figure 4.12 Typical weld Region observed under SEM. A weld line created by re-orientation of glass fibre is observed.

(a). 7% WR at Magnification 400X



(b). 7% WR at Magnification 1200X



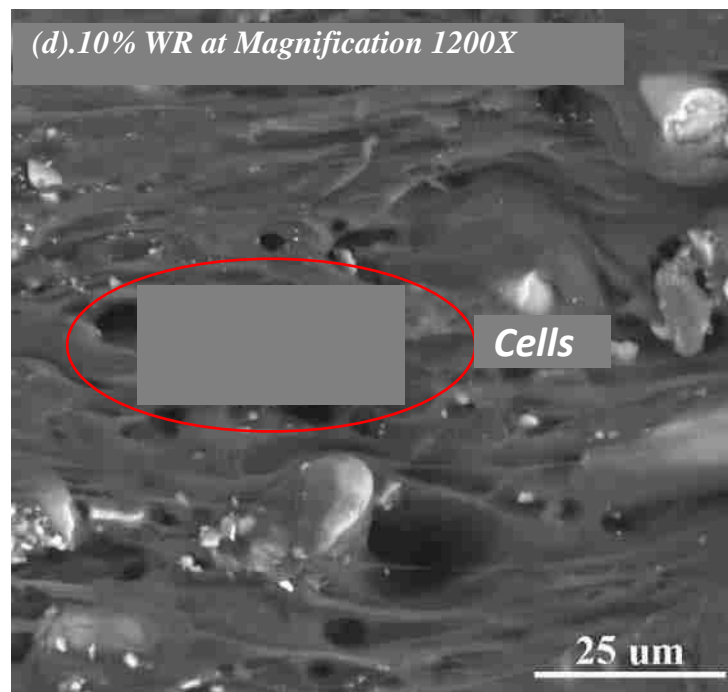
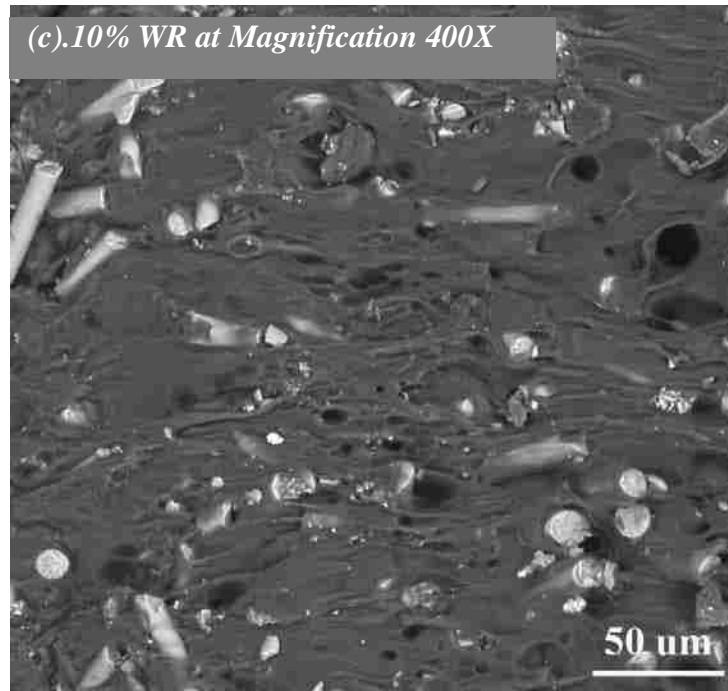


Figure 4.13 Cells observed at weld region after cryogenic fracturing. (a)SEM image for 7% WR with the magnification of 400x (b) SEM image for 7% WR with the magnification of 1200x. Compact and deformed cells were found at the weld region.

CHAPTER 5 DISCUSSION

As discussed in Chapter 4, the B3WG6-GPX, which exhibits the maximum weld strength, is selected to be further analyzed in our study. The burst strength for the solid and MuCell® B3WG6-GPX samples are compared in Figure 5.1. As can be seen in the figure, the solid sample shows significantly higher burst strength than the MuCell® samples. For the MuCell® samples, the burst strength increases with increasing weight reductions (from 4% to 7%) up to 0.964 MPa and then decreases to 0.8 MPa as the weight reduction reaches 10%.

In this work, all the samples were moulded under similar conditions, and the welding was carried out on the two halves of moulded beads, as indicated in the experimental section. Besides the influence of inherent material properties, the MuCell® process itself may have an effect on the weld performance. Furthermore, the weld strength of the microcellular samples might be related to their non-cell region thickness close to the weld, cell morphology, and degree of crystallinity. The changes in these factors were normally achieved by varying weight reductions. The correlation between these factors and burst strength will be considered and discussed separately below.

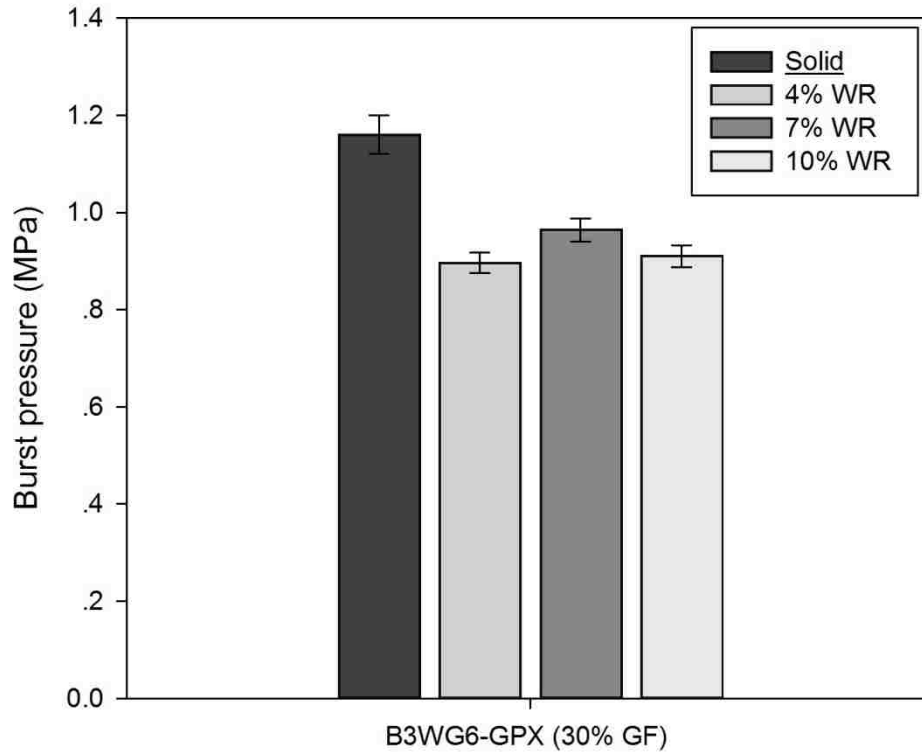


Figure 5.1 Burst strength of the welded samples with standard deviation. Highest burst strength was observed on solid sample and the weld strength increased as the weight reduction of MuCell® sample increased from 4% to 7%.

5.1 EFFECT OF NONE-CELL REGION THICKNESS

Very limited literature is available regarding the relationship between none-cell thicknesses and weld strength in microcellular injection moulded parts. One possible influence is assumed here: If the combined thicknesses of the none-cells close to the weld region are lower than the weld depth that was set during the friction welding process (1.511 mm), the beads on the test samples will be worn away to the level of the cell region during the friction welding. This results in the loss of weld strength. This assumption is supported by Kishbaugh et al.'s study [63], which investigated the weld

strength of friction-welded solid and 10% density-reduced PA 6. It was found that the drop in burst pressure for MuCell® parts with a 10% density reduction as compared to welded assemblies using solid parts is 12% higher when the cell structure was observed within the weld area [69–70].

However, it can be concluded from Table 5.1 that for all samples examined in this study, the thickness of the none-cell close to the weld region is much thicker than the weld depth, which was set during welding process (1.511 mm total for the combined 4 and 6 mm parts). This observation indicates that the possibility of the two parts penetrating to the cell region during the friction welding was negligible. Variations in the none-cell layer thickness, in this case, may not have an obvious effect on the weld strength, since the total of the two thicknesses is always greater than the set weld depth.

Table 5.1 Average none-cell region thickness and weld depth for solid, 4%, 7% and 10% WR samples

<i>Sample</i>	<i>Solid</i>	<i>4% WR</i>	<i>7% WR</i>	<i>10% WR</i>
<i>Average None-cell region thickness</i>	<i>NA</i>	<i>5.24</i>	<i>4.78mm</i>	<i>3.08mm</i>
<i>Number of samples observed</i>	<i>4</i>	<i>4</i>	<i>4</i>	<i>4</i>
<i>STD</i>	<i>NA</i>	<i>0.12</i>	<i>0.12</i>	<i>0.24</i>
<i>Weld depth</i>	<i>1.511mm</i>	<i>1.511</i>	<i>1.511mm</i>	<i>1.511mm</i>

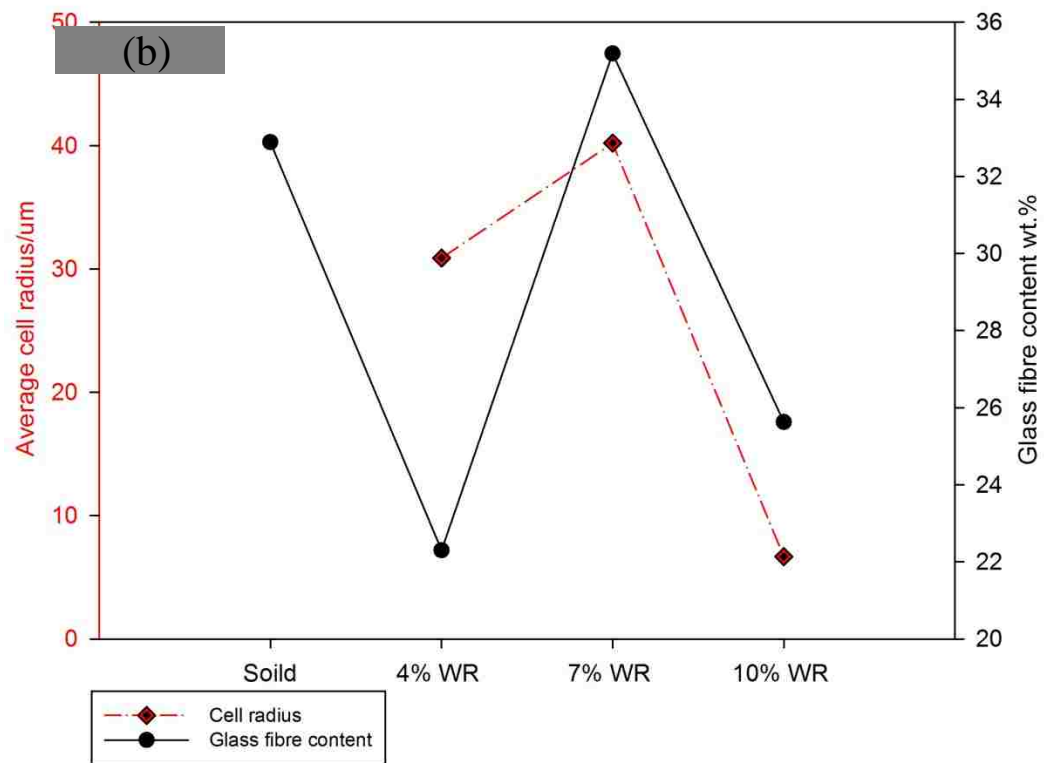
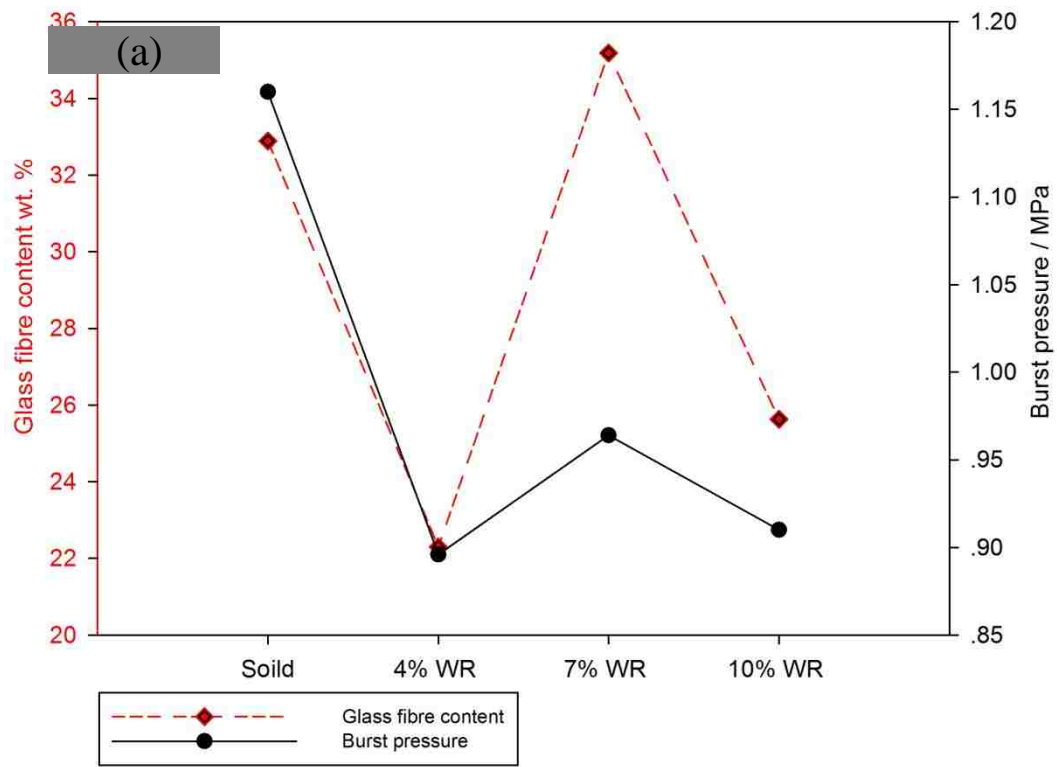
5.2 EFFECT OF GLASS FIBRE AND CELL MORPHOLOGY

Among the MuCell® samples tested in this study, an increase in burst strength was observed with higher glass fibre content at the weld region (Figure 5.2 (a)). According to Kamal et al. [71], the retention of larger fractions of glass fibres in the weld joint is an important factor for obtaining higher joint strength.

Beside, a trend can be observed as is illustrated in Figure 5.2 (b) and (c). The 7% WR sample, which has the largest cell size and area occupied by cells at cell region, exhibited the highest glass fibre content at the weld region among the MuCell® samples. For the 10% WR sample, the average cell radius is just 6.67 μm , which is similar to the radius of glass fibre (5.05 μm) filled in the composite. As a result, a lower content of glass fibres in the weld region can be seen for 10% WR sample.

Based on these results, it is tempting to speculate that with appropriate cell size and cell area at the cell region, the internal pressure provided by cell growth may “push” the glass fibre out of the cell region and lead to relatively higher fibre content close to the weld region, which contributes to higher weld strength. Similar assumptions have been made by several studies that proper cell growth may result in the redistribution and orientation of glass fibres during mould filling and improve the tensile properties of microcellular foamed fibre glass-reinforced parts [72-74].

An interpretation of the “push” effect of cell growth on glass fibres is shown schematically in Figure 5.3.



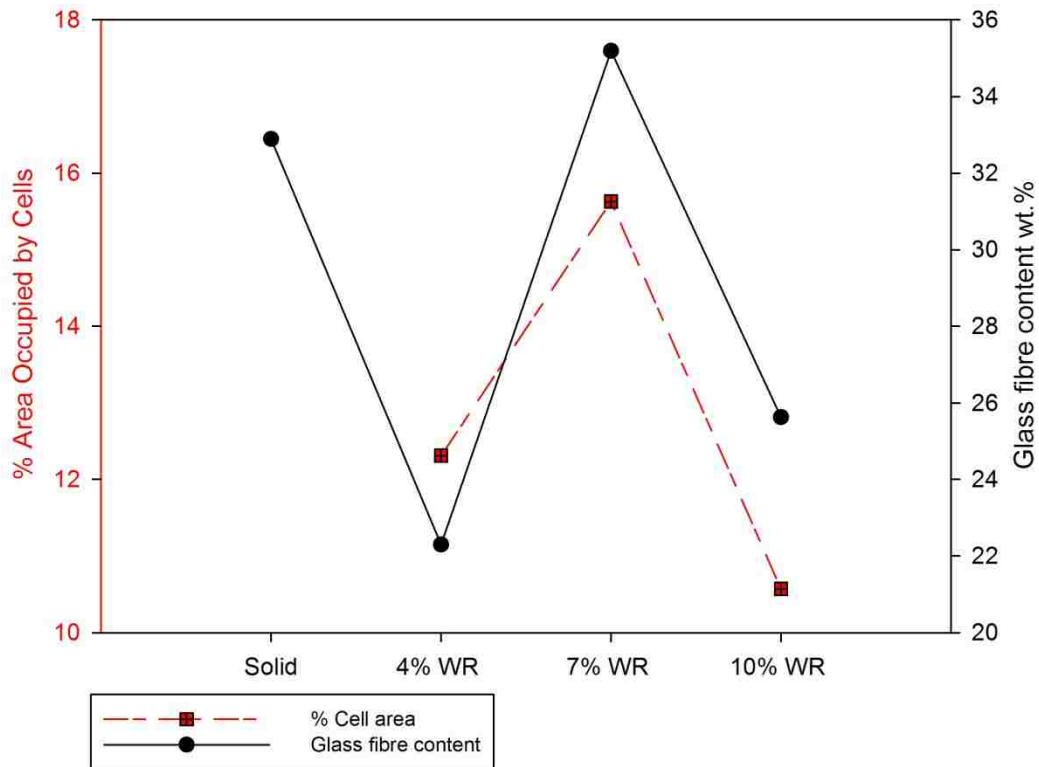


Figure 5.2 (a) Fibre content at weld region for solid, 4%, 7% and 10% WR samples VS burst pressure. (b) Average cell radius VS glass fibre content at weld (c) Area occupied by cells VS glass fibre content at weld. Higher fibre content at the weld region would possibly result in higher weld strength among the MuCell® samples.

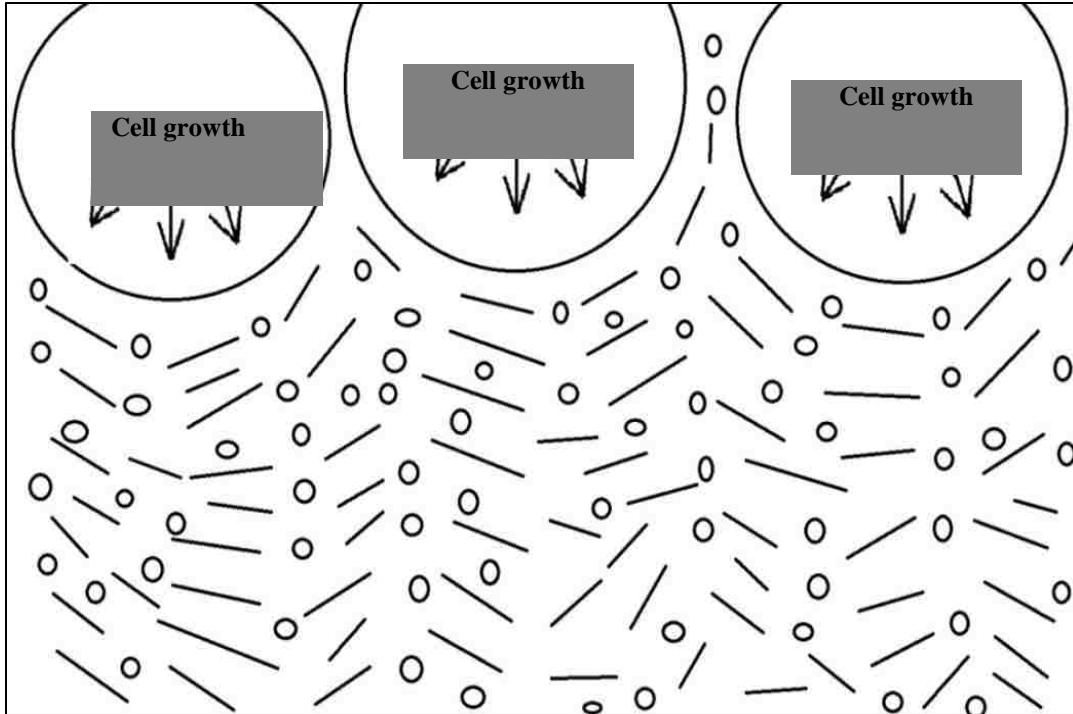


Figure 5.3 Schematic of the “push” effect of cell growth on glass fibre. The internal pressure provided by proper cell growth may result in the redistribution and orientation of glass fibre.

Even though our data suggest that higher fibre content close to the weld region plays a role in increasing weld strength, it is worth mentioning that there is a limitation regarding this trend. For instance, superfluous glass fibre will result in the lack of a matrix to protect the fibre and insufficient adhesion between fibre and polymer matrix. The lack of sufficient matrix to hold onto the fibres means they will be exposed to the applied force during the test and be easily broken.[41] The weakened interfacial character indicates a failure at the interface between the fibre and matrix, which can significantly lower the weld strength. In addition, the effect of cell size and cell density on weld strength might turn from positive to negative if they are beyond certain critical values.

Besides, it should also be noted that since the cell region is away from the weld region, the variation of cell size and cell morphology and the resulting change of the glass fibre content at the weld region may not be the main effect on weld strength among all samples. Further studies are still necessary in order to conclude a causal association.

5.3 EFFECT OF CRYSTALLINITY

Incorporate with the TGA results, a comparison of the melting enthalpies of the measured samples after first heating with the average melting enthalpy achieved by slow cooling (maximum achievable degree of crystallinity) suggests a suppression of the crystallization of the tested samples in the formulations.

The crystallinity of the weld region is shown in Figure 5.4. The lowest degree of crystallinity was measured for the solid sample, and the highest value was observed for the 4% WR sample. Besides, the variation of degree of crystallinity between the 4% WR and 10% WR samples is relatively small.

Moreover, referring to Figure 5.1 and Figure 5.4, no obvious relationship between degree of crystallinity of the weld region and the weld strength can be found in this study.

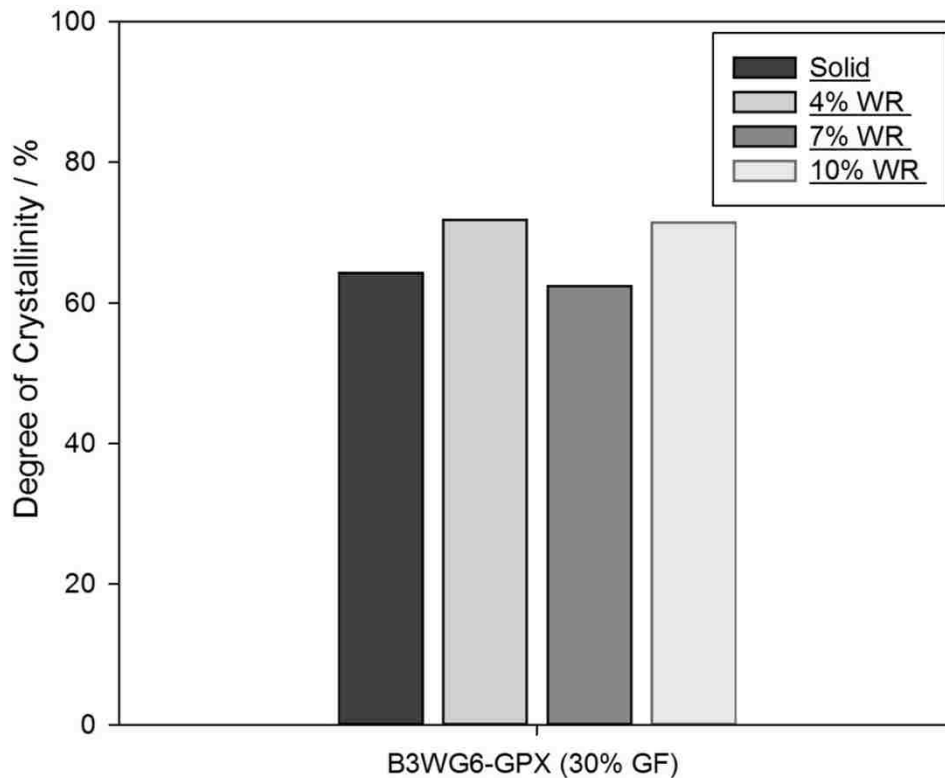


Figure 5.4 The degree of crystallinity for B3WG6-GPX with varying weight reduction

5.4 EFFECT OF CELLS AT WELD REGION

Although the previous discussion explains that the highest weld strength among all tested MuCell® samples can be attributed to the largest cell size and cell area, which increases the glass fibre content at the weld region, the reason why lower weld strength can be observed on the MuCell® samples (compared with their solid counterpart) is still unknown and therefore is discussed in this section.

As discussed above, the weld depth set during vibration welding is much lower than the none-cell region thickness in order to avoid the weld region penetrating the cell

region. However, microstructural analysis by SEM and optical microscopy indicated that uniform cells are nevertheless observed at the weld region of the MuCell® parts. This observation seems to suggest that cells can be generated in the molten polymer during vibration welding.

It is commonly known that the primary cell nucleation happens during the filling stage. Through injection moulding, the thermodynamic instability, created by the rapid pressure drop of the gas-melt solution, will promote drastic cell nucleation. However, at the region which will be welded (located at the filling end); the polymer front was cooled rapidly after being pushed to the cavity wall. Therefore, the temperature and time subjected to the phase separation and cell nucleation at this region are quite low and short, respectively. Consequently, cells were found to be non-existent at this area [75-78]. Furthermore, Wang et al. [79] indicated that besides rapid cooling, the formation of the none-cell region layer can also be attributed to the dissolving of gas into polymer melt at part none-cell region during filling stage. Combining this conclusion with results from the weld region observation, it can be concluded that vibration welding causes a “second-nucleation” of cells at the welded none-cell region. This theory is strongly supported when observing the fracture surface by SEM. As can be seen from Figure 4.11, compact cells were observed on the fracture for all MuCell® samples. The shape of the cells is near-spherical, and the distribution of cell sizes is relatively uniform (with a diameter of 5–9 μm).

The mechanism of foaming during vibration welding can be explained as follows: When vibration welding was applied, the frictional heat generated will reduce the viscosity of the polymer until a suitable viscosity is reached where the gas will separate

out of the polymer and nucleate by overcoming the peripheral nucleation resistance, including the surface tension, shear stress, and the elasticity (Figure 5.1). In addition, it is worth noting that in order for the nucleation to occur, the weld pressure employed should be sufficiently low. This assumption is clearly supported by the presence of the distorted cells (deformed by the shear stress created by welding) observed at the weld region.

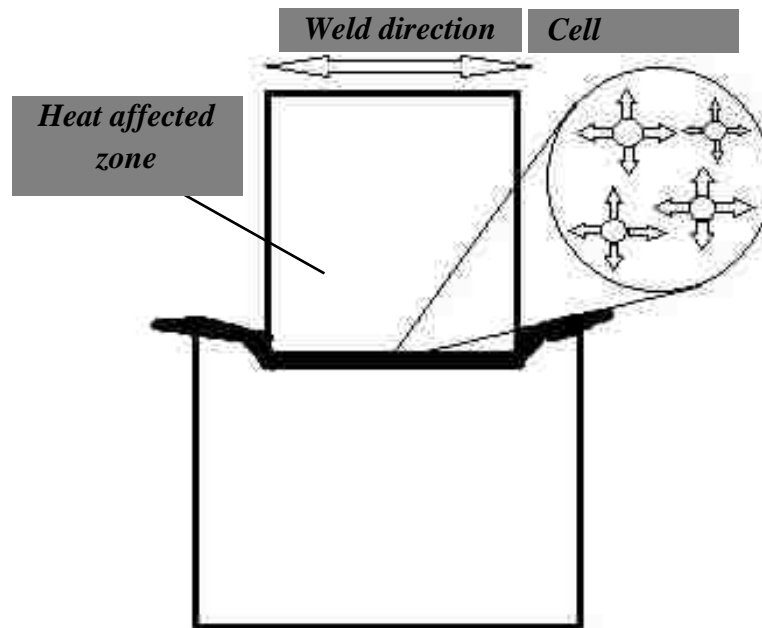


Figure 5.5 Schematic of the cell nucleating during vibration welding. Frictional heat generated will melt the polymer at the weld joint which creates a suitable condition for cells to nucleate.

It can be concluded from Figure 5.1, Figure 4.11, and Figure 4.13 that the existence of cells at the weld region has negative influence on weld strength. The cells on the welding surface weaken the joint strength by replacing matrix material at the weld joint. In addition, it is especially problematic that the cells tend to nucleate at the interface between fibres and matrix (Figure 5.6). Since there is more interfacial energy at

the fibre surface, the nucleation's driving force at the fibre surface is larger than in other regions, meaning that less free energy needs to be overcome for nucleating [80-81]. Those interfacial cells lead to poor fibre-matrix bonding and can be considered interfacial cracks which dramatically increase the risk of fibre being pulled out and interfacial failure during the burst test [82-85].

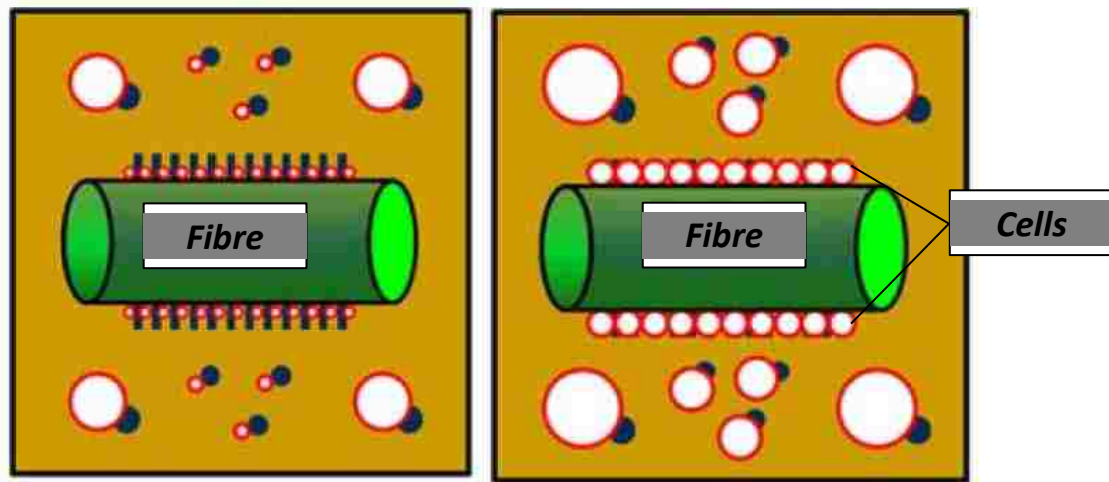


Figure 5.6 Schematic of cell growth beside glass fibre

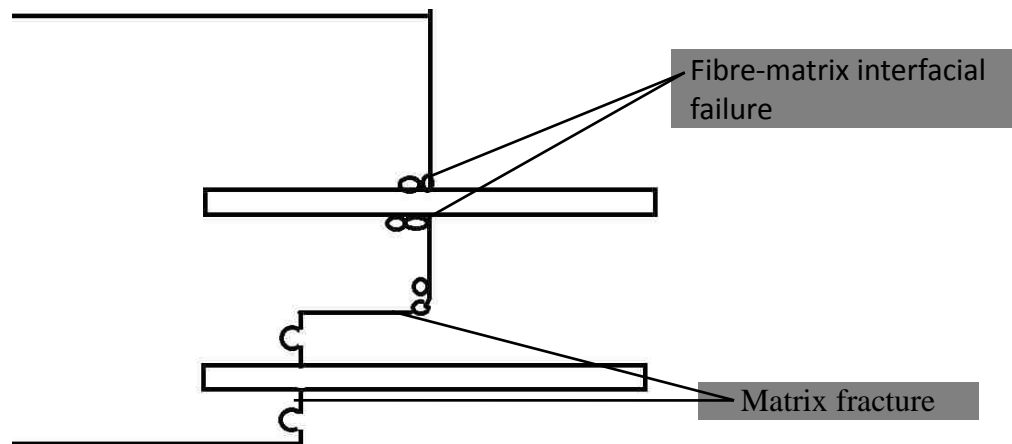


Figure 5.7 Cells on the welding surface would weaken the part joining and fibre-matrix bonding

CHAPTER 6 CONCLUSIONS AND RECOMMENDATIONS

6.1 OVERVIEW

The aim of this study is to determine the optimal material for MuCell® manufacturing to achieve maximum weld strength and the effect of this process on weld strength and fatigue life.

Three different nylon-fibre glass composites with 30– 35 wt. % glass fibre and one 50 wt. % glass fibre fabricated using the microcellular (MuCell®) injection moulding process were studied by burst test and pressure cycle fatigue test. The conclusions are presented below:

- The MuCell® process results in a decrease of weld strength.
- B3WG6-GPX shows the highest weld strength and is selected for microstructural and thermal investigation.

6.1.1 EFFECT OF THE MUCCELL® PROCESS ON WELD STRENGTH

- The weld depth set for the selected sample during vibration welding was much lower than the none-cell region thickness. Thus, the potential for the two parts to “touch” the cell region during welding, resulting in lower weld strength, is negligible.
- The 7% WR sample was observed to give the highest weld strength among all tested MuCell® samples, and this might be attributed to higher fibre glass content at the weld region.
- The frictional heat generated by the vibration welding will cause the gas to be separated from the matrix again and nucleate into distinctive cells at the weld region.

- The cells on the welding joint weaken the matrix joining and fibre-matrix bonding between two parts, which can be considered an explanation for the lower weld strength observed in the MuCell® samples.

6.2 RECOMMENDATIONS FOR FUTURE RESEARCH

- Alternate the weld parameters (such as decrease weld depth or increase weld pressure) to optimize the weld features (smaller or fewer cells at the weld region).
- Assemble the two weld beads and joining them only by applying heat at the weld joint instead of employing friction welding, to analyse whether the frictional heat is the cause for secondary nucleation of cells at the weld region.
- Verify whether the secondary cells are the only cause of reduced weld strength, since the MuCell® process also lowers the tensile strength and possibly leads to lower weld strength due to increased peel behaviour in the weld failure. It would be helpful to also perform tensile tests on both 4 mm and 6 mm weld beads.

REFERENCES

- [1] M Stumpf, A Spörrer, H Schmidt, V Altstädt. Influence of supramolecular additives on foam morphology of injection-molded i-PP, *Journal of Cellular Plastics*. 47 (2011) 519-534.
- [2] J Li, Z Chen, X Wang, T Liu, Y Zhou, S Luo. Cell morphology and mechanical properties of microcellular mucell® injection molded polyetherimide and polyetherimide/fillers composite foams, *J Appl Polym Sci*. 130 (2013) 4171-4181.
- [3] D Elduque, I Clavería, Á Fernández, C Javierre, C Pina, J Santolaria. Methodology to analyze the influence of microcellular injection molding on mechanical properties with samples obtained directly of an industrial component, *Polym.Polym.Compos*. 22 (2014) 743.
- [4] T Liu, H Liu, L Li, X Wang, A Lu, S Luo. Microstructure and Properties of Microcellular Poly (phenylene sulfide) Foams by Mucell Injection Molding, *Polym.Plast.Technol.Eng*. 52 (2013) 440-445.
- [5] JF Gómez-Gómez, D Arencón, MÁ Sánchez-Soto, AB Martínez. Influence of the injection moulding parameters on the microstructure and thermal properties of microcellular polyethylene terephthalate glycol foams, *Journal of Cellular Plastics*. (2012) 0021955X12460044.
- [6] T Liu, S Zhou, Y Lei, Z Chen, X Wang, J Li, et al. Morphology and Properties of Injection Molded Microcellular Poly (ether imide)(PEI)/Polypropylene (PP) Foams, *Ind Eng Chem Res*. 53 (2014) 19934-19942.
- [7] PA Toensmeier. Microcellular foam could increase appeal of nylon in underhood parts, *Plast.Eng*. 62 (2006) 10-11.
- [8] A Chandra, S Gong, M Yuan, L Turng, P Gramann, H Cordes. Microstructure and crystallography in microcellular injection-molded polyamide-6 nanocomposite and neat resin, *Polymer Engineering & Science*. 45 (2005) 52-61.
- [9] NP Suh, Impact of microcellular plastics on industrial practice and academic research, 201 (2003) 187-202.
- [10] S Hwang, Z Ke. The dimensional stability of a microcellular injection molded gear shaft, *Int.Communicat.Heat Mass Transfer*. 35 (2008) 263-275.
- [11] JE Martini-Vvedensky, NP Suh, FA Waldman. Saturation with inert gas, depressurization, and quick-cooling. (1984).

- [12] SW Cha, NP Suh, DF Baldwin, CB Park. Microcellular thermoplastic foamed with supercritical fluid. (1992).
- [13] CB Park, NP Suh, DF Baldwin. Method for providing continuous processing of microcellular and supermicrocellular foamed materials. (1999).
- [14] KP Johnston, JM Penninger, Supercritical fluid science and technology, American Chemical Society 1989.
- [15] E Kiran, JF Brennecke. Supercritical fluid engineering science: fundamentals and applications. (1993).
- [16] Aim, Karel, and Maurizio Fermeglia. "Solubility of Solids and Liquids in Supercritical Fluids." *The Experimental Determination of Solubilities*, Volume 6 (2002): 491-555.
- [17] Wikipedia contributors, Supercritical fluid, Wikipedia, The Free Encyclopedia. . 2 July 2014 18:58 UTC (28 June 2015 23:55 UTC)
https://en.wikipedia.org/w/index.php?title=Supercritical_fluid&oldid=669113819.
- [18] W Michaeli, T Krumpholz, D Obeloer, Profoam, A New Foaming Process for Injection Molding, (2008).
- [19] Kauffmann, A. Walter, B. Diemert, J. Eyerer, P. Extruded particle foams – Material- and process Investigations, (2007).
- [20] JS Colton. The nucleation of microcellular thermoplastic foam. (1985).
- [21] J Colton, N Suh. The nucleation of microcellular thermoplastic foam with additives: Part I: Theoretical considerations, *Polymer Engineering & Science*. 27 (1987) 485-492.
- [22] JS Colton, NP Suh. Nucleation of microcellular foam: theory and practice, *Polymer Engineering & Science*. 27 (1987) 500-503.
- [23] N Ramesh, DH Rasmussen, GA Campbell. The heterogeneous nucleation of microcellular foams assisted by the survival of microvoids in polymers containing low glass transition particles. Part I: Mathematical modeling and numerical simulation, *Polymer Engineering & Science*. 34 (1994) 1685-1697.
- [24] AK Bledzki, M Rohleder, H Kirschling, A Chate. Correlation between morphology and notched impact strength of microcellular foamed polycarbonate, *Journal of Cellular Plastics*. 46 (2010) 415-440.
- [25] G Lin, X Zhang, L Liu, J Zhang, Q Chen, L Zhang. Study on microstructure and mechanical properties relationship of short fibers/rubber foam composites, *European Polymer Journal*. 40 (2004) 1733-1742.

- [26] H Huang, J Wang. Equipment development and experimental investigation on the cellular structure of microcellular injection molded parts, *Polym.Test.* 27 (2008) 513-519.
- [27] JM Williams, DA Wroblewski. Microstructures and properties of some microcellular foams, *J.Mater.Sci.* 24 (1989) 4062-4067.
- [28] Matuana, L. M. "Solid state microcellular foamed poly (lactic acid): morphology and property characterization." *Bioresource technology* 99.9 (2008): 3643-3650.
- [29] D Miller, V Kumar. Microcellular and nanocellular solid-state polyetherimide (PEI) foams using sub-critical carbon dioxide II. Tensile and impact properties, *Polymer.* 52 (2011) 2910-2919.
- [30] W Michaeli, L Flórez, T Krumpholz, D Obeloer, Effects of the foam morphology in the mechanical properties of injection molded thermoplastic foams, (2008).
- [31] Dominik Obeloer, et al. Improvement Of The Mechanical Properties Of Thermoplastics Foams Through Modification Of The Foam Structure, ANTEC. (2009) 2840-2844.
- [32] W Michaeli, L Florez, D Obeloer, M Brinkmann. Analysis of the Impact Properties of Structural Foams, *Journal of Cellular Plastics.* 45 (2009) 321-351.
- [33] T Czigány, J Karger-Kocsis. Comparison of the failure mode in short and long glass fiber-reinforced injection-molded polypropylene composites by acoustic emission, *Polymer Bulletin.* 31 (1993) 495-501.
- [34] N Sato, T Kurauchi, S Sato, O Kamigaito. Mechanism of fracture of short glass fibre-reinforced polyamide thermoplastic, *J.Mater.Sci.* 19 (1984) 1145-1152.
- [35] J Horst, J Spoormaker. Mechanisms of fatigue in short glass fiber reinforced polyamide 6, *Polymer Engineering & Science.* 36 (1996) 2718-2726.
- [36] V Karbhari, B Parks, A Dolgopolsky. Effect of mean load levels on fatigue in random short-fibre injection-moulded composites, *J.Mater.Sci.Lett.* 8 (1989) 220-221.
- [37] Hertzberg, Richard W., H. Nordberg, and J. A. Manson. "Fatigue crack propagation in polymeric materials." *Journal of Materials Science* 5.6 (1970): 521-526..
- [38] MR Piggott, Load bearing fibre composites, Springer 2002.
- [39] T Harmia. Fatigue behavior of neat and long glass fiber (LGF) reinforced blends of nylon 66 and isotactic PP, *Polymer composites.* 17 (1996) 926-936.

- [40] J Thomason. The influence of fibre length and concentration on the properties of glass fibre reinforced polypropylene: 5. Injection moulded long and short fibre PP, Composites Part A: Applied Science and Manufacturing. 33 (2002) 1641-1652.
- [41] LM Matuana, CB Park, JJ Balatinecz. Cell morphology and property relationships of microcellular foamed pvc/wood-fiber composites, Polymer Engineering & Science. 38 (1998) 1862-1872.
- [42] J Thomason. The influence of fibre length, diameter and concentration on the strength and strain to failure of glass fibre-reinforced polyamide 6, 6, Composites Part A: Applied Science and Manufacturing. 39 (2008) 1618-1624.
- [43] M Mahmoodi, AH Behravesht. The Effect of Pressure Drop Rate on Microstructures of Unfilled and Glass-filled ABS Microcellular Foams, Iranian Polymer Journal. 16 (2007) 839.
- [44] HE Naguib, CB Park, U Panzer, N Reichelt. Strategies for achieving ultra low-density polypropylene foams, Polymer Engineering & Science. 42 (2002) 1481-1492.
- [45] JS Colton, NP Suh. The nucleation of microcellular thermoplastic foam with additives: Part I: Theoretical considerations, Polymer Engineering & Science. 27 (1987) 485-492.
- [46] L Chen, H Sheth, R Kim. Gas absorption with filled polymer systems, Polymer Engineering & Science. 41 (2001) 990-997.
- [47] L Matuana-Malanda, C Park, J Balatinecz. Characterization of microcellular foamed PVC/cellulosic-fibre composites, Journal of Cellular Plastics. 32 (1996) 449-469.
- [48] K Din, S Hashemi. Influence of short-fibre reinforcement on the mechanical and fracture behaviour of polycarbonate/Acyilonitrile Butadiene Styrene polymer blend, J.Mater.Sci. 32 (1997) 375-387.
- [49] AK Bledzki, J Kuehn-Gajdzik. Microcellular of Glass Fibre Reinforced PC/ABS: Effect of the Processing Condition on the Morphology and Mechanical Properties, Cell.Polym. 29 (2010) 27-43.
- [50] Jaarsma, Frank. "Fiber reinforced cellular foam product." U.S. Patent No. 8,647,543. 11 Feb. 2014..
- [51] RA Vaia, EP Giannelis. Polymer melt intercalation in organically-modified layered silicates: model predictions and experiment, Macromolecules. 30 (1997) 8000-8009.
- [52] H Wang, C Zeng, M Elkovitch, LJ Lee, KW Koelling. Processing and properties of polymeric nano-composites, Polymer Engineering & Science. 41 (2001) 2036-2046.

- [53] Yuan, Mingjun, et al. "Study of injection molded microcellular polyamide-6 nanocomposites." *Polymer Engineering and Science* 44.4 (2004): 673-686.
- [54] M Yuan, L Turng. Microstructure and mechanical properties of microcellular injection molded polyamide-6 nanocomposites, *Polymer*. 46 (2005) 7273-7292.
- [55] V Stokes, Toward a weld-strength data base for vibration welding of thermoplastics, (1995) 1280-1284.
- [56] VK Stokes. Joining methods for plastics and plastic composites: an overview, *Polymer Engineering & Science*. 29 (1989) 1310-1324.
- [57] P Bates, J Mah, H Liang, Microstructure of vibration welded nylon 66 joints. In ANTEC 2001 Conference (2001) 5-6.
- [58] V Kagan, S Lui, G Smith, J Patry. The Optimized Performance of Linear Vibration Welded Nylon 6 and Nylon 66 Butt Joints, Imaging and image analysis applications for plastics. (1999) 1.
- [59] AK Schlarb, GW Ehrenstein. The impact strength of butt welded vibration welds related to microstructure and welding history, *Polymer Engineering & Science*. 29 (1989) 1677-1682.
- [60] P Bates, J MacDonald, V Sidiropoulos, M Kontopoulou. Comparison of experimental and analytical vibration welding meltdown-time profiles for nylon 66 and polypropylene, *Polymer Engineering & Science*. 45 (2005) 789-797.
- [61] MR Kamal, Y Chung, R Gomez. Three-dimensional fiber orientation in vibration welded joints of glass fiber reinforced polyamide-6, *Polymer Composites*. 29 (2008) 954-963.
- [62] M Gehde, M Giese, GW Ehrenstein. Welding of thermoplastics reinforced with random glass mat, *Polymer Engineering & Science*. 37 (1997) 702-714.
- [63] Levi Kishbaugh (Trexel Inc.), Uwe Kolshorn (Trexel GmbH), Gerard Bradley (Rhodia Engineering Plastics s.r.l.), Vibration and ultrasonic welding conditions and performance for glass fibre filled PA 6 and PA 6.6 injection moulded using the MuCell® microcellular foaming process. R&D Trexel (Company report). (2007) 1-9.
- [64] L Hyde, L Kishbaugh, The MuCell® Injection Molding Process: A Strategic Cost Savings Technology for Electronic Connectors, (2003).
- [65] J Colton, N Suh. The nucleation of microcellular thermoplastic foam with additives: Part II: Experimental results and discussion, *Polymer Engineering & Science*. 27 (1987) 493-499.

- [66] H Guanghong, W Yue, Microcellular Foam Injection Molding Process, INTECH Open Access Publisher 2012.
- [67] J Horst, J Spoormaker. Mechanisms of fatigue in short glass fiber reinforced polyamide 6, Polymer Engineering & Science. 36 (1996) 2718-2726.
- [68] Y Chung, MR Kamal. Morphology of PA-6 vibration welded joints and its effect on weld strength, Polymer Engineering & Science. 48 (2008) 240-248.
- [69] S Leduc, D Rodrigue. Effect of weld lines on the injection moulding of structural foams. I. Foam morphology, Cell.Polym. 24 (2005) 313-327.
- [70] S Leduc, D Rodrigue. Effect of weld lines on the injection moulding of structural foams. II mechanical properties, Cell.Polym. 25 (2006) 63-83.
- [71] Y Chung, MR Kamal. Morphology of PA-6 vibration welded joints and its effect on weld strength, Polymer Engineering & Science. 48 (2008) 240-248.
- [72] M Rodriguez-Perez, J Lobos, C Pérez-Muñoz, J De Saja. Mechanical response of polyethylene foams with high densities and cell sizes in the microcellular range, Journal of Cellular Plastics. (2009).
- [73] J Xu, L Kishbaugh. Simple modeling of the mechanical properties with part weight reduction for microcellular foam plastic, Journal of cellular plastics. 39 (2003) 29-47.
- [74] EH Tejada, CZ Sahagún, R González-Núñez, D Rodrigue. Morphology and mechanical properties of foamed polyethylene-polypropylene blends, Journal of cellular plastics. 41 (2005) 417-435.
- [75] J Chen, X Sun, L Turng, T Liu, W Yuan. Investigation of crystallization behavior of solid and microcellular injection molded polypropylene/nano-calcium carbonate composites using carbon dioxide as a blowing agent, Journal of Cellular Plastics. (2013) 0021955X13488400.
- [76] W Weng, G Chen, D Wu. Crystallization kinetics and melting behaviors of nylon 6/foiated graphite nanocomposites, Polymer. 44 (2003) 8119-8132.
- [77] G Zheng, W Yang, M Yang, J Chen, Q Li, C Shen. Gas-assisted injection molded polypropylene: The skin-core structure, Polymer Engineering & Science. 48 (2008) 976-986.
- [78] Z Xi, X Sha, T Liu, L Zhao. Microcellular injection molding of polypropylene and glass fiber composites with supercritical nitrogen, Journal of Cellular Plastics. (2014) 0021955X14528931.

- [79] G Wang, G Zhao, J Wang, L Zhang. Research on formation mechanisms and control of external and inner bubble morphology in microcellular injection molding, *Polymer Engineering & Science*. (2014) 807-835.
- [80] Meli, Gilles. Nucleation efficiency of talc in the foaming behaviour and cellular structure of polymer-based foams. U.S. Patent Application (2013) 14/409,658.
- [81] CB Park, NP Suh, DF Baldwin. Mixing supercritical foaming agent; homogenizing, nucleation, depressurization, shaping, releasing. (2000).
- [82] Z Xi, X Sha, T Liu, L Zhao. Microcellular injection molding of polypropylene and glass fiber composites with supercritical nitrogen, *Journal of Cellular Plastics*. (2014) 0021955X14528931.
- [83] Z Ma, G Zhang, Q Yang, X Shi, J Li, X Fan. Microcellular foams of glass–fiber reinforced poly (phenylene sulfide) composites generated using supercritical carbon dioxide, *Polymer Composites*. (2015).
- [84] T Kuboki. Foaming behavior of cellulose fiber-reinforced polypropylene composites in extrusion, *Journal of Cellular Plastics*. (2013) 0021955X13504775.
- [85] H Zhai, X Zhou, L Fang, A Lu. Study on mechanical properties of powder impregnated glass fiber reinforced poly (phenylene sulphide) by injection molding at various temperatures, *J Appl Polym Sci*. 115 (2010) 2019-2027.

VITA AUCTORIS

NAME: Tianhao Guo

PLACE OF BIRTH: Urumqi, Xinjiang, China

DATE OF BIRTH: 1990

EDUCATION: Bachelor of Engineering,
Polymer Science and Engineering
Nanjing Tech University, Jiangsu China
2008-2012

Master of Applied Science
Engineering Materials
University of Windsor
Windsor, ON, Canada
2013-2015